

Jordan Journal of Mechanical and Industrial Engineering (JJMIE)

JJMIE is a high-quality scientific journal devoted to fields of Mechanical and Industrial Engineering. It is published by The Jordanian Ministry of Higher Education and Scientific Research in corporation with the Hashemite University.

EDITORIAL BOARD

Editor-in-Chief

Prof. Mousa S. Mohsen

Editorial board

Prof. Bilal A. Akash
Hashemite University

Prof. Adnan Z. Al-Kilany
University of Jordan

Prof. Ayman A. Al-Maaitah
Mutah University

Prof. Moh'd A. Al-Nimr
Jordan University of Science and Technology

Prof. Ali A. Badran
University of Jordan

Prof. Naseem M. Sawaqed
Mutah University

Assistant Editor

Dr. Ahmad Al-Ghandoor
Hashemite University

THE INTERNATIONAL ADVISORY BOARD

Abu-Qudais, Mohammad
Jordan University of Science & Technology, Jordan

Abu-Mulaweh, Hosni
Purdue University at Fort Wayne, USA

Afanah Abdul-Hafiz
Robert Bosch Corporation, USA

Afonso, Maria Dina
Institute Superior Tecnico, Portugal

Badiru, Adedji B.
The University of Tennessee, USA

Bejan, Adrian
Duke University, USA

Chalhoub, Nabil G.
Wayne State University, USA

Cho, Kyu-Kab
Pusan National University, South Korea

Dincer, Ibrahim
University of Ontario Institute of Technology, Canada

Douglas, Roy
Queen's University, U. K

El Bassam, Nasir
International Research Center for Renewable Energy,
Germany

Haik, Yousef
United Arab Emirates University, UAE

Jaber, Jamal
Al- Balqa Applied University, Jordan

Jubran, Bassam
Ryerson University, Canada

Kakac, Sadik
University of Miami, USA

Khalil, Essam-Eddin
Cairo University, Egypt

Mutoh, Yoshiharu
Nagaoka University of Technology, Japan

Pant, Durbin
Iowa State University, USA

Riffat, Saffa
The University of Nottingham, U. K

Saghir, Ziad
Ryerson University, Canada

Sarkar, MD. Abdur Rashid Bangladesh University of
Engineering & Technology, Bangladesh

Siginer, Dennis
Wichita State University, USA

Sopian, Kamaruzzaman
University Kebangsaan Malaysia, Malaysia

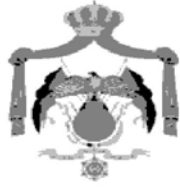
Tzou, Gow-Yi Yung-Ta Institute of Technology and
Commerce, Taiwan

EDITORIAL BOARD SUPPORT TEAM

Language Editor **Publishing Layout**
Dr. Wael Zuraiq MCPD. Osama AlShareet

SUBMISSION ADDRESS:

Prof. Mousa S. Mohsen, Editor-in-Chief
Jordan Journal of Mechanical & Industrial Engineering,
Hashemite University, PO Box 330127, Zarqa, 13133, Jordan
E-mail: jjmie@hu.edu.jo



Hashemite Kingdom of Jordan



Hashemite University

Jordan Journal of
Mechanical and Industrial Engineering

JJMIIE

An International Peer-Reviewed Scientific Journal

<http://jjmie.hu.edu.jo/>

ISSN 1995-6665

Jordan Journal of Mechanical and Industrial Engineering (JJMIE)

JJMIE is a high-quality scientific journal devoted to fields of Mechanical and Industrial Engineering. It is published by The Jordanian Ministry of Higher Education and Scientific Research in corporation with the Hashemite University.

Introduction: The Editorial Board is very committed to build the Journal as one of the leading international journals in mechanical and industrial engineering sciences in the next few years. With the support of the Ministry of Higher Education and Scientific Research and Jordanian Universities, it is expected that a heavy resource to be channeled into the Journal to establish its international reputation. The Journal's reputation will be enhanced from arrangements with several organizers of international conferences in publishing selected best papers of the conference proceedings.

Aims and Scope: Jordan Journal of Mechanical and Industrial Engineering (JJMIE) is a refereed international journal to be of interest and use to all those concerned with research in various fields of, or closely related to, mechanical and industrial engineering disciplines. Jordan Journal of Mechanical and Industrial Engineering aims to provide a highly readable and valuable addition to the literature which will serve as an indispensable reference tool for years to come. The coverage of the journal includes all new theoretical and experimental findings in the fields of mechanical and industrial engineering or any closely related fields. The journal also encourages the submission of critical review articles covering advances in recent research of such fields as well as technical notes.

Guide for Authors

Manuscript Submission

High-quality submissions to this new journal are welcome now and manuscripts may be either submitted online or mail.

Online: For online submission upload one copy of the full paper including graphics and all figures at the online submission site, accessed via E-mail: jjmie@hu.edu.jo. The manuscript must be written in MS Word Format. All correspondence, including notification of the Editor's decision and requests for revision, takes place by e-mail and via the Author's homepage, removing the need for a hard-copy paper trail.

By Mail: Manuscripts (1 original and 3 copies) accompanied by a covering letter may be sent to the Editor-in-Chief. However, a copy of the original manuscript, including original figures, and the electronic files should be sent to the Editor-in-Chief. Authors should also submit electronic files on disk (one disk for text material and a separate disk for graphics), retaining a backup copy for reference and safety.

Note that contributions may be either submitted online or sent by mail. Please do NOT submit via both routes. This will cause confusion and may lead to delay in article publication. Online submission is preferred.

Submission address and contact:

Prof. **Mousa S. Mohsen**, Editor-in-Chief
Jordan Journal of Mechanical & Industrial Engineering,
Hashemite University,
PO Box 330127, Zarqa, 13133, Jordan
E-mail: jjmie@hu.edu.jo

Types of contributions: Original research papers

Corresponding author: Clearly indicate who is responsible for correspondence at all stages of refereeing and publication, including post-publication. Ensure that telephone and fax numbers (with country and area code) are provided in addition to the e-mail address and the complete postal address. Full postal addresses must be given for all co-authors.

Original material: Submission of an article implies that the work described has not been published previously (except in the form of an abstract or as part of a published lecture or academic thesis), that it is not under consideration for publication elsewhere, that its publication is approved by all authors and that, if accepted, it will not be published elsewhere in the same form, in English or in any other language, without the written consent of the Publisher. Authors found to be deliberately contravening the submission guidelines on originality and exclusivity shall not be considered for future publication in this journal.

Supplying Final Accepted Text on Disk: If online submission is not possible: Once the paper has been accepted by the editor, an electronic version of the text should be submitted together with the final hardcopy of the manuscript. The electronic version must match the hardcopy exactly. We accept MS Word format only. Always keep a backup copy of the electronic file for reference and safety. Label the disk with your name. Electronic files can be stored on CD.

Notification: Authors will be notified of the acceptance of their paper by the editor. The Publisher will also send a notification of receipt of the paper in production.

Copyright: All authors must sign the Transfer of Copyright agreement before the article can be published. This transfer agreement enables Jordan Journal of Mechanical and Industrial Engineering to protect the copyrighted material for the authors, but does not relinquish the authors' proprietary rights. The copyright transfer covers the exclusive rights to reproduce and distribute the article, including reprints, photographic reproductions, microfilm or any other reproductions of similar nature and translations.

PDF Proofs: One set of page proofs in PDF format will be sent by e-mail to the corresponding author, to be checked for typesetting/editing. The corrections should be returned within 48 hours. No changes in, or additions to, the accepted (and subsequently edited) manuscript will be allowed at this stage. Proofreading is solely the author's responsibility. Any queries should be answered in full. Please correct factual errors only, or errors introduced by typesetting. Please note that once your paper has been proofed we publish the identical paper online as in print.

Author Benefits

Page charge: Publication in this journal is free of charge.

Free off-prints: Three journal issues of which the article appears in along with twenty-five off-prints will be supplied free of charge to the corresponding author. Corresponding authors will be given the choice to buy extra off-prints before printing of the article.

Manuscript Preparation:

General: Editors reserve the right to adjust style to certain standards of uniformity. Original manuscripts are discarded after publication unless the Publisher is asked to return original material after use. If online submission is not possible, an electronic copy of the manuscript on disk should accompany the final accepted hardcopy version. Please use MS Word for the text of your manuscript.

Structure: Follow this order when typing manuscripts: Title, Authors, Affiliations, Abstract, Keywords, Introduction, Main text, Conclusions, Acknowledgements, Appendix, References, Figure Captions, Figures and then Tables. For submission in hardcopy, do not import figures into the text - see Illustrations. For online submission, please supply figures imported into the text AND also separately as original graphics files. Collate acknowledgements in a separate section at the end of the article and do not include them on the title page, as a footnote to the title or otherwise.

Text Layout: Use double spacing and wide (3 cm) margins. Ensure that each new paragraph is clearly indicated. Present tables and figure legends on separate pages at the end of the manuscript. If possible, consult a recent issue of the journal to become familiar with layout and conventions. All footnotes (except for table and corresponding author footnotes) should be identified with superscript Arabic numbers. To conserve space, authors are requested to mark the less important parts of the paper (such as records of experimental results) for printing in smaller type. For long papers (more than 4000 words) sections which could be deleted without destroying either the sense or the continuity of the paper should be indicated as a guide for the editor. Nomenclature should conform to that most frequently used in the scientific field concerned. Number all pages consecutively; use 12 or 10 pt font size and standard fonts. If submitting in hardcopy, print the entire manuscript on one side of the paper only.

Corresponding author: Clearly indicate who is responsible for correspondence at all stages of refereeing and publication, including post-publication. The corresponding author should be identified with an asterisk and footnote. Ensure that telephone and fax numbers (with country and area code) are provided in addition to the e-mail address and the complete postal address. Full postal addresses must be given for all co-authors. Please consult a recent journal paper for style if possible.

Abstract: A self-contained abstract outlining in a single paragraph the aims, scope and conclusions of the paper must be supplied.

Keywords: Immediately after the abstract, provide a maximum of six keywords (avoid, for example, 'and', 'of'). Be sparing with abbreviations: only abbreviations firmly established in the field may be eligible.

Symbols: All Greek letters and unusual symbols should be identified by name in the margin, the first time they are used.

Units: Follow internationally accepted rules and conventions: use the international system of units (SI). If other quantities are mentioned, give their equivalent in SI.

Maths: Number consecutively any equations that have to be displayed separately from the text (if referred to explicitly in the text).

References: All publications cited in the text should be presented in a list of references following the text of the manuscript.

Text: Indicate references by number(s) in square brackets in line with the text. The actual authors can be referred to, but the reference number(s) must always be given.

List: Number the references (numbers in square brackets) in the list in the order in which they appear in the text.

Examples:

Reference to a journal publication:

- [1] M.S. Mohsen, B.A. Akash, "Evaluation of domestic solar water heating system in Jordan using analytic hierarchy process". Energy Conversion & Management, Vol. 38, No. 9, 1997, 1815-1822.

Reference to a book:

- [2] Strunk Jr W, White EB. The elements of style. 3rd ed. New York: Macmillan; 1979.

Reference to a conference proceeding:

- [3] B. Akash, S. Odeh, S. Nijmeh, "Modeling of solar-assisted double-tube evaporator heat pump system under local climate conditions". 5th Jordanian International Mechanical Engineering Conference, Amman, Jordan, 2004.

Reference to a chapter in an edited book:

- [4] Mettam GR, Adams LB. How to prepare an electronic version of your article. In: Jones BS, Smith RZ, editors. Introduction to the electronic age, New York: E-Publishing Inc; 1999, p. 281-304

Free Online Color: If, together with your accepted article, you submit usable color and black/white figures then the journal will ensure that these figures will appear in color on the journal website electronic version.

Tables: Tables should be numbered consecutively and given suitable captions and each table should begin on a new page. No vertical rules should be used. Tables should not unnecessarily duplicate results presented elsewhere in the manuscript (for example, in graphs). Footnotes to tables should be typed below the table and should be referred to by superscript lowercase letters.

PAGES	PAPERS
162 – 167	Fuzzy Logic Approach for Metal Casting Selection Process <i>Kasim M. Daws , Zouhair I. AL-Dawood , Sadiq H. AL-Kabi</i>
168 – 173	Dead Sea Mud Slurry Flow in a Horizontal Pipe <i>Abdelaziz Khlaifat, Taha Al-Khamis</i>
174 – 181	Japanese Manufacturing Techniques and Practices: An Indian Perspective <i>Jamal A. Farooque, Asit B. Mohapatra</i>
182 – 189	Automatic Control of Electrodes in Lithotripsy Machine <i>J. Al-Nabulsi, H. Amasha, B. Altrabsheh, B. Al-Nami</i>
190 -197	Comparision of Diesel Engine Performance and Emissions from Neat and Transesterified Cotton Seed Oil <i>A.Siva Kumar, D. Maheswar, K. Vijaya Kumar Reddy</i>
198 – 205	Thermal Simulation of a Pyrotechnic Solid-Propellant Gas Generator <i>Mohammad K. Alkam, P. Barry Butler</i>
206 – 215	The Effect of Fatigue on Crack Propagation in Flat Plates under Buckling Bending and Shear <i>Fathi A. Al-Shamma</i>
216 - 221	Water Pumping System with PLC and Frequency Control <i>Akayleh Ali, Mohammed Al_Soud, Essam Abdallah, Salah Addallah</i>
222 - 227	plane Deformation of a Textile Material with Boundary Forces Using Finite Element Method <i>M. A. Nawafleh, N. Al-Kloub</i>
228 – 235	Modeling and Verification of Double Slope Single Basin Solar Still Using Laboratory and Actual Solar Conditions <i>K. Kalidasa Murugavel, Kn. K. S. K. Chockalingam, K. Srithar</i>

Fuzzy Logic Approach for Metal Casting Selection Process

Kasim M. Daws , Zouhair I. AL-Dawood* , Sadiq H. AL-Kabi

Mechanical Engineering Department, University of Baghdad, Baghdad, Iraq

Abstract

Selecting the proper material is a vital step in the design process because the appropriateness of the choice has a significant impact on part performance and cost. A poorly selected material adds unnecessary cost and may affect the ease of processing. In this paper an automated advisory material selection system is designed. The designed system is named (CAMS). The objectives of this system are to solve the problems of Materials selection and evaluation (M/P&E) activities. The designed system depends on methodology for selection and evaluation of materials that are based on a number of user-specified attributes or requirements. The decision model enables the representation of the designer's preferences over the decision factors, and it is based on weighted property index (W.P.I) algorithms to determine the relative importance of each requirements. A compatibility rating between product profile requirements and the alternatives stored in the database for each decision criteria are generated using fuzzy logic (F.L) methodology. These requirements were matched with the capabilities of each (alloy) or material. The compatibility ratings are aggregated into single rating of that alternative's compatibility. A ranked set of compatible alternative alloys is produced t by the system. This approach has advantages over the existing systems that don't have a decision module or are not integrated with a database.

© 2009 Jordan Journal of Mechanical and Industrial Engineering. All rights reserved

Keywords: Materials Selection; Fuzzy Logic; Weighted Algorithm.

1. Introduction

The selection of the correct materials for a design is a key step in the process because it is a crucial decision that links computer calculations and lines on an engineering drawing with a working design. Materials and the manufacturing processes, which convert the material into useful part, strengthen all of engineering design. [1]. The material and manufacturing process selection problem is a multi-attribute decision-making problem. These decisions are made during preliminary design stages in an environment characterized by uncertain requirements, parameters, and relationships. Material and process selection (MPS) decisions occur before design for manufacturing (DFM) can begin [2, 3]. Studies have indicated that although the cost of product design is only around 5% of the total product cost, decisions made during the design stage affect (70 – 80 %) of the final product cost [4].

In this paper, a development of an advisory system is called Computer Aided Material Selection (CAMS) that aids the designer in decision-making (D.M). The objectives of the designed system are to evaluate and select the optimal and alternative materials (alloy) that satisfy the design specifications. The system (CAMS) indicates to the designer the compatibility degree between the selected materials (alloy) to all the specified properties

and characteristics, and then these selected materials are ranked according to their compatibilities.

2. Importance of Materials Selection

The increasingly tough competition on international markets forced many firms to search for new methods of producing high quality products at low cost. Designing for better products must take into consideration the balance between cost, quality, and performance triplex. To achieve such objectives, designers must use quantitative and qualitative techniques. The possible advantages result from manufacturing by using more flexible methods of production and more efficient equipment [5]. The recognition of importance of materials selection in design has increased in recent years. The adoption of concurrent engineering methods has brought materials engineers into the design process at an earlier stage, and the importance given to manufacturing in present day product design has reinforced the fact that materials and manufacturing are closely linked in determining final product performance [1]. Figure (1) shows the structure for material classification, ending with a schematic of a record some of attribute [6].

3. General Criteria in Material Selection Process

Selection of materials on the basis of performance characteristics is the process of matching values of the properties of the materials with the requirements and constraints imposed by the design. Selection on the basis

* Corresponding author. Ziaa04@yahoo.com.

of processing characteristics deals with finding the process that will form the material into the required shape with a minimum of defects at the least cost. Selection on the basis of an environmental profile is concerned with the impact of the material throughout its life cycle upon the environment. The chief business consideration that affects materials selection is the cost of the part that is made from the material [1]. Materials are selected on the basis of the following four general criteria [1]:

1. Performance characteristics (properties).
2. Processing characteristics.
3. Environmental profile .
4. Business considerations .

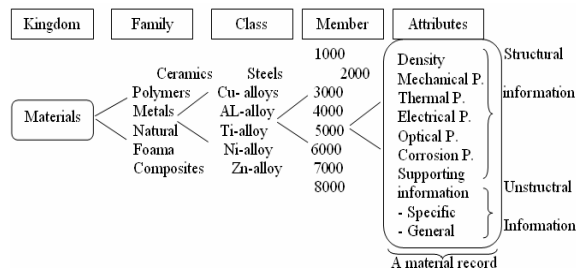


Figure 1. A hierarchical structure for material classification [6].

There are literally hundreds of different properties of materials. The most important to consider when selecting a material for a given product are those that are essential to the function of the product. Generally, most designers put equal importance on the factors of properties, availability, and economics, which list these factors along with some pertinent sub factors [7]. One of the critical factors affecting material selection practice is the function and performance requirement. Functional and performance requirements for materials include [7]:

a- Structural Requirements:

Such as strength, stiffness, and their degree of retention in adverse service environments.

b- Non structural Requirements:

Such as corrosion resistance, electrical or thermal performance, plus color and texture.

c- C-Design & Production Criteria:

Such as part size, shape, and production rate desired. All determine which process and technologies are best suited to the application.

Some attributes which knowledge based materials selector needs to process are suggested. A selector, which can reason with a large number of diverse materials, needs [8]:

1. The ability to deal with simple and complex data structures .
2. Powerful structures for data acquisition and updating. by modifications.
3. To manage spares data.
4. To compare incomplete descriptions.
5. To reason with appropriate classifications.
6. To model confidence .
7. To maintain consistency.
8. To be easily extensible.

4. Methodology of the Weighted Approach

In material / process selection, there are many factors that are affected in selection material or alloy to be manufactured. These factors are different in degree of

importance for each application or a specific situation. The differences between factors (properties) depend on the design requirement for each part. Then each property has a degree of importance differ from another property. Each input property is assigned a weight between (0 and 1), with (0) being unimportant and (1) being very important. Since different properties are expressed in different units, the best procedure is to normalize these differences by using a scaling factor. Scaling is a simple technique to bring all the different properties within on numerical range. Since different properties have widely different numerical values, each property must be so scaled that the largest value does not exceed 100 [1].

$$\beta = (NVP / LV) 100 \quad (1)$$

β = Scaled property

NVP = Numerical value of property

LV = Largest value under consideration

For properties such that it is more desirable to have low value e.g. density, corrosion loss, cost, and electrical resistance, the scale factor is formulated as follows [1]:

$$N = n(n-1) / 2 \quad (2)$$

5. Fuzzy Logic Approach

Fuzzy logic (F.L.) is one of the elements of artificial intelligence that is gaining popularity and applications in control systems and pattern recognition. It is based on the observation that people make decisions based on imprecise and numerical information. Fuzzy models or sets are mathematical means of representing vagueness and imprecise information, Accordingly the term used is fuzzy [9]. These models have the capability of recognizing, representing, manipulating, interpreting, and utilizing data and information that are vague and lack certainty. The concept of fuzzy can be illustrated in figure (2).

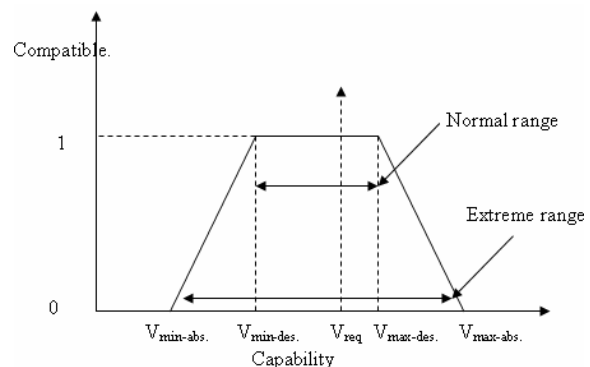


Figure 2. Fuzzy mapping of process capability [9].

Where:

$V_{\min-abs}$ = the absolute minimum value.

$V_{\min-des}$ = the desire minimum value .

V_{req} = the requirement value.

$V_{\max-des}$ = the absolute maximum value.

$V_{\max-abs}$ = the desire maximum value.

In fuzzy logic approach, the part process compatibility value will gradually grow from 0 to 1, instead of suddenly jumping from 0 (incompatible) to 1 (fully compatible). For analysis, the process of compatibility and the range of capability are needed in the previous values to be mapped

on a normalized scale as in the previous figure. If the value of part requirement falls within $V_{\min\text{-des}}$ and $V_{\min\text{-abs}}$ then the compatibility is considered to be fully compatible. If the part requirement value is between $V_{\min\text{-abs}}$ and $V_{\min\text{-des}}$, or between $V_{\max\text{-des}}$ and $V_{\max\text{-abs}}$, then the compatibility is considered to be less than 1 but more than 0. If the part requirement value is less than $V_{\min\text{-abs}}$ or more than $V_{\max\text{-abs}}$, then the compatibility is considered to be zero.

The compatibility $P(x_i)$ for a value x_i of an attribute i can be calculated by using the following equations [9]:

$$P(x_i) = 1 \text{ if } V_{\min\text{-des}} < x_i < V_{\max\text{-des}} \quad (5)$$

$$P(x_i) = (x_i - V_{\min\text{-abs}}) / (V_{\min\text{-des}} - V_{\min\text{-abs}}) \text{ if } V_{\min\text{-abs}} < x_i < V_{\min\text{-des}} \quad (6)$$

$$P(x_i) = (V_{\max\text{-abs}} - x_i) / (V_{\max\text{-abs}} - V_{\max\text{-des}}) \text{ if } V_{\max\text{-des}} < x_i < V_{\max\text{-abs}} \quad (7)$$

$$P(x_i) = 0 \text{ if } x_i < V_{\min\text{-abs}}, \text{ or } x_i > V_{\max\text{-abs}} \quad (8)$$

Fuzzy technologies and devices can be applied successfully in areas such as robotics, motion control, evaluation of design alternatives, decision making, design of intelligent systems, materials selection involving multi-criteria, image processing, and machine vision [10].

6. Methodology of Materials Selection

The methodology used in this paper for selection material is one of the artificial intelligence techniques, and it is suitable when there is fuzziness in the requirements. The material selection module assesses the degree of compatibility between a material alternative and the product profile requirements. Material compatibility is performed via selection queries on the database for each product specifications. The queries are based on the application of fuzzy logic approach to determine the degree of compatibility for each material. This approach differs from existing approaches in determining the values of compatibilities for both optimal and alternative selection alloys, and this doesn't exist in the other approaches. Then this method is more accurate than other methods.

In this paper, we selected aluminum and steel alloys as a database in material selection database dependent on references [11], [12], and [13]. There are about seventy alloys of aluminum and steel with different chemical composition. Then each alloy gave properties different to other alloy. To select the optimal alloy from alternative alloys, the user or designer can enter the range of values for mechanical properties with degree of accuracy required or named fuzzy limit. Then by using fuzzy logic approach (FLA) as mentioned in previous section, any alloy that has values out of the range of absolutely limits will be eliminated.

7. Computer Aided Material Selection (CAMS)

To select the optimum alloy or alternative alloys, the system will display the main window, which contains the sub-windows are:

1. General Applications Environment,

2. Properties Required,
3. Properties priorities,
4. Material Selection,
5. Evaluation , and
6. Final Results.

The first and second windows contained questions about the required properties and specifications. The third window asked the user about the preference degree of each selected property. The fourth window gave the selected alloys with degrees of compatibility's to ensure the specified properties. The fifth window gave the evaluations for each selected alloy with compatibility to each property. The final window gave the final results with draw diagrams to show the total compatibility with properties to select optimal and alternative alloys; we will clear the application of the system from case study.

8. Case Study

To evaluate the working of the (CAMS) system, we select bearing cover (B.C) part that is used in many applications like in ceiling fan. Then the problem is to select the type of alloy that are satisfied (B.C) part with specifications and quality. The required specifications can be illustrated in table (1) as follow:

Table 1. the required material properties for producing (B.C) part.

Mechanical properties		Physical Properties	
Tensile strength range	(220 to 280) Mpa	Specific Gravity	medium
Yield stress range	(140 to 180) Mpa	Density	minimum
Elongation range	(1 to 3) %	Other Properties:	
Brinell Hardness	(60 to 100) HB	Castability	Very Good
		Weldability	Very Good
		Corrosion resistance	Good

The system will display the special window for material selection as shown in figure (3), this window contains six sub-windows.

To determine the required properties for (B.C) part which are the range of values of mechanical properties with fuzzy limit for each property is entered. For physical properties, specific gravity, with medium and minimum density, is selected. For other properties, capability degree from the command bottom should be very good, and good for corrosion resistance is also selected as shown in figure (4).

The selected properties are not equal in degree of preference. Then to determine the degree of importance for each property, a click on command property priorities is made. In this case, the system will display sets of small windows containing only two properties that will ask the user about which property is preferred over other properties. The user must click on the property that is considered most importance than other properties. This is illustrated in figure (5).

After determining weights for each property, the system will display all the alloys that satisfied all the specified properties. The working of the system in this stage takes two steps: first step screening all the alloys that screened in application environment phase (i.e any alloy

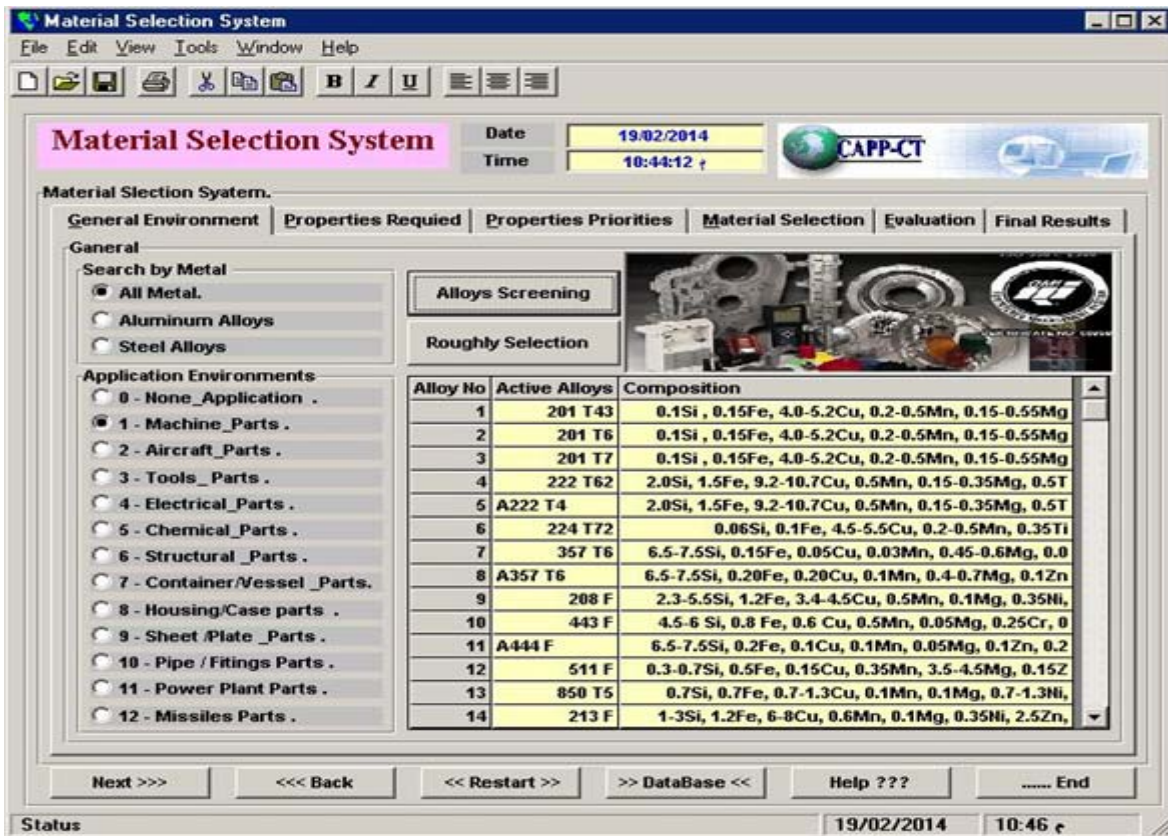


Figure 3 .Application environment window.

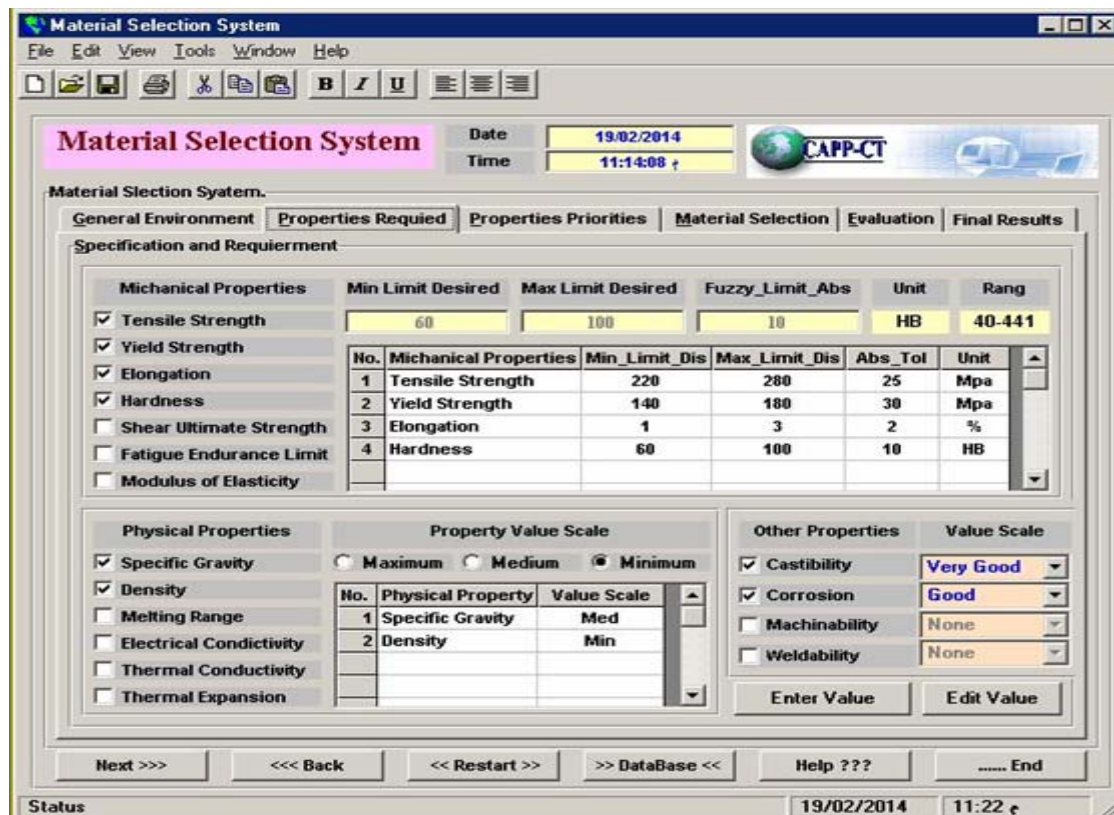


Figure 4. Materials properties window for (CAMS) system .

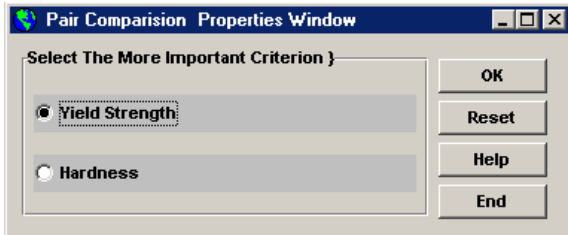


Figure 5. Pair comparison properties window.

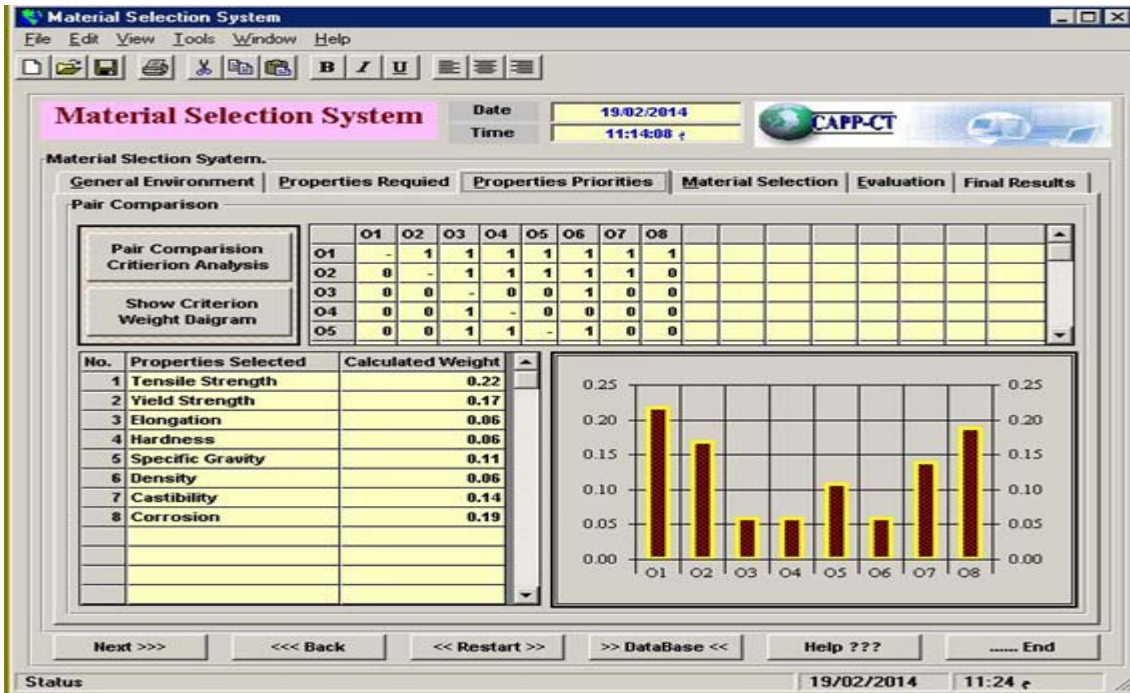


Figure 6. Weights drawing window .

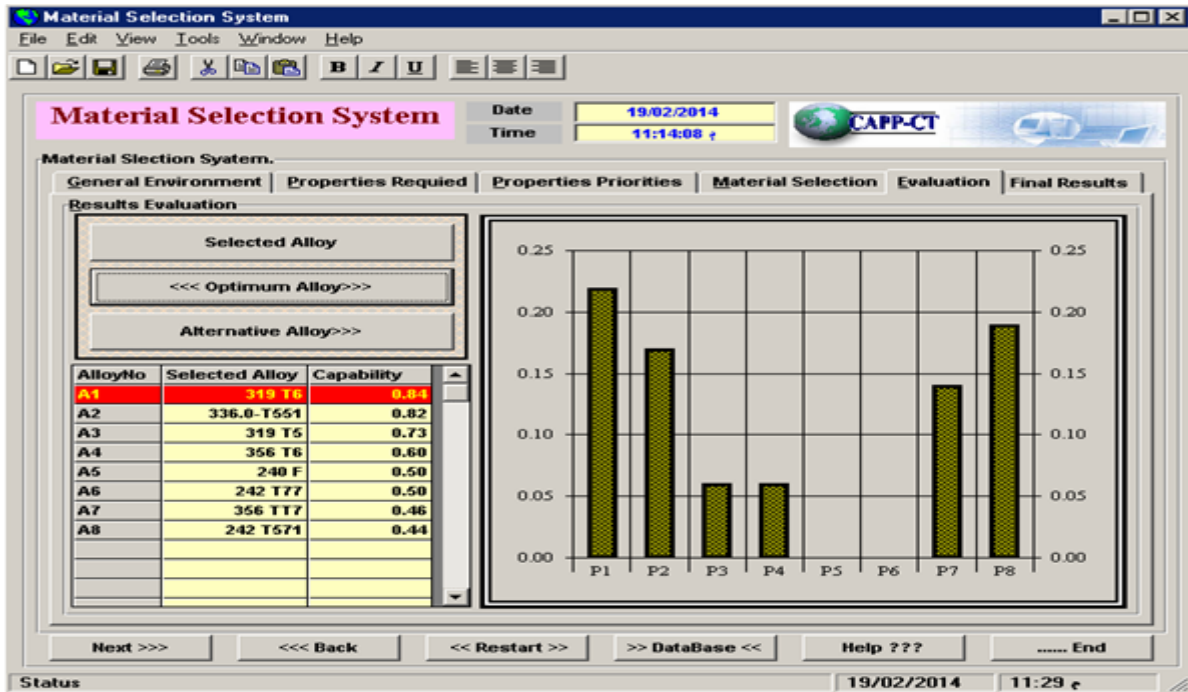


Figure 7. Evaluation alloys window.

does not satisfy the specified mechanical properties will be eliminated) and give each satisfied alloy value of compatibility with respect to mechanical properties. The second step is ranking the satisfied alloys according to the degree of compatibility with all other properties (i.e., physical, and other properties). The weights for each property with its diagrams can be illustrated in figure (6). Then the system will display the optimum alloy with all alternative alloys, and draw in a diagram of each alloy with degree of compatibility to each specified property as shown in figure (7).

From the above window, the designer or the decision maker (D.M) can select the optimal alloy which has the maximum compatibility degree with the specifications required. If the optimal alloy doesn't available or costly, the (D.M) can select the other alternatives available alloys take into the consideration the degree of compatibility with the property required. Also the (D.M) can benefit from the diagrams that are drawn for each property with respect to the alloy compatibility.

The final step is where the (CAMS) system will display the selected optimum or alternatives alloy with chemical composition, and will display all the properties for the selected alloy, and will draw the diagram for value of the total compatibility with respect to all specified properties.

9. Conclusions

The methodology that is used in this paper for selection material selection is one of the artificial intelligence techniques, and it is suitable when there is fuzziness in the requirements. The designed system serves not only to select the optimum or alternative material, but also to serve to evaluate the degree of compatibility with specifications requirements. The (CAMS) system gives the real representation in a diagram for each selected material for showing the degree of compatibility with respect to properties or characteristics are required.

After applying the (CAMS) system on the part (B.C), the optimum alloy that is selected is (Aluminum 319) with degree of compatibility for the specified properties is 84 %. Also there are other alternative alloys that are ranked according to the degree of compatibility. If the optimum

alloy does not exist in the company, the alternative alloy is (Aluminum 336) with degree of compatibility 82 %. The degrees of compatibility that are obtained from the system are varying from part to part and depending on the user preference to the required properties or requirements. The diagrams of compatibilities that are drawn between each alloy or to each property are clear real representation of capability for each alloy to the satisfied requirements. Hence, the designer can benefit from these diagrams in decision making for selecting the most preferred to him. The alternatives selected alloys / processes enable the designer to make some of modifications in the design stage until reaching satisfaction of the requirements of design.

References

- [1] Dieter G E. Engineering design a materials and processing approach. 3rd ed . Mc Graw-Hill Inc.; 2000.
- [2] S. Karthik, C. Chung, K. Ramani, "Rapid application development of process capability supplier". 23rd Computer and Information in Engineering (CIE) Conference, Chicago Illinois, Sept. 2-6, 2003.
- [3] Jeffrey W H. New directions in design for manufacturing. University of Maryland; 2004.
- [4] Y C Saty, K Gupta, "A web-based process/ material advisory system". Florida ASME International, Mechanical engineering congress and Exposition, November 5-10, 2000.
- [5] R. Neuffill, "Materials selection maximizing overall utility". Metals & Materials, Vol. 4, No. 6, 1988, 378-382.
- [6] Ashby M , Cebon F. New approaches to materials education. Cambridge University; 2002.
- [7] Myer K. Hand book of materials selection. New York: John Wiley & Sons; 2002.
- [8] A. Demaid, J. Zucker, "A conceptual model for materials selection". Metals & Materials, Vol.4, No. 5, 1988, 291- 296.
- [9] Ravi B. Metal casting computer aided design and analysis. New Delhi: Prentice hall of India; 2005.
- [10] Kalpakjian S. Manufacturing processes for engineering materials. 3rd ed. Addison wisely Longman. Inc; 2001.
- [11] Stefanescu D M. Metal handbook casting. 5th ed, Vol.15, ASM; 1988.
- [12] International ASM. Metals handbook desk edition. 2nd ed; 1998.
- [13] Robert B R. Metallic materials. 3rd ed. New York: E & F.N Spon; 1980.

Dead Sea Mud Slurry Flow in a Horizontal Pipe

Abdelaziz Khlaifat*, Taha Al-Khamis

Department of Chemical Engineering, Mutah University, Mutah 61710, Jordan

Abstract

This paper reports the results of experimental work on the flow of Dead Sea mud through a circular pipe. The dependence of the discharge of the Dead Sea mud in pipe on water content is examined for four different mud-water mixtures that were pumped through a horizontal pipe. A mathematical model describing all observed phenomena was developed. Experimental results were compared with prediction, using shear stress power law equation, and good agreement was obtained. The obtained results may find their application not only in the transportation of Dead Sea mud, but also in assessing the pumping requirements for the transportation of dredged cohesive mud at in-situ water content.

© 2009 Jordan Journal of Mechanical and Industrial Engineering. All rights reserved

Keywords: Flow; Mud; Dead Sea; Slurry; Non-Newtonian.

Nomenclature

k	flow consistency index
L	pipe length
n	flow behavior index
P	pressure
Q	volumetric flow rate
r	radial direction (m)
R	pipe radius (m)
\mathcal{U}	slurry velocity (m/s)
Z	axial direction (m)

Greek letters

μ	viscosity (N.s/m ²)
τ	shear stress
θ	angular direction

Subscripts

z	axial direction
app	apparent
inlet	
L	outlet
rz	in z-direction on a unit area perpendicular to the r-direction.

1. Introduction

One of the most raved-about muds in the world comes from the Dead Sea in Jordan. Detailed information about the Dead Sea and the effect of brine evaporation on its content were discussed in [1]. Dead Sea black mud (because of its color) is a mixture of Dead Sea minerals and organic materials naturally formed over thousands of

years on the bed of the Dead Sea. Physical properties, chemical, and mineralogical compositions of the Dead Sea mud were investigated for three different locations on the Eastern shore of the Dead Sea [2]. Due to its mineralogical contents, Dead Sea black mud replenishes the skin minerals essential for renewal and regeneration by removing toxins and dead cells with an exfoliating action. Its cleans, purifies, and rejuvenates skin tissue giving a brighter complexion [3-4]. Black Mud also stimulates blood and lymph circulation, increasing Oxygen intake and draining trapped fluids. It is therefore effective in treating cellulite and in alleviating arthritic and rheumatic conditions [5-6]

Different skin care products, bath salts, and cosmetics products are manufactured from the Dead Sea black mud. Large amount of this mud has to be collected, using special scoops, from different locations on the shore of the Dead Sea, then transported by trucks to the company site where the mud is pretreated and packed in small portions, then shipped to different manufacturers.

In this manuscript, we suggest hydraulic transportation of Dead Sea mud instead of dealing with the mentioned-above tedious process of mud collection and handling. Hydraulic transportation of Dead Sea mud in a circular pipe requires mixing the mud with water to decrease the mud viscosity, and accordingly friction. In order to minimize the mud pretreatment cost, industries which will pump Dead Sea mud will be under continuous pressure to decrease water content and increase mud concentration. At high concentration, the viscous forces, which are usually highly non-Newtonian and yield stress in nature, become dominant, and mud flows inevitably becomes laminar [7]. The objective of this paper is to demonstrate that the Dead Sea mud can be pumped from its source to the exploiting industry and to show and evaluate the impact of changing

* Corresponding author. khlaifat@mutah.edu.jo.

non-Newtonian viscous stresses have on pipelining problem.

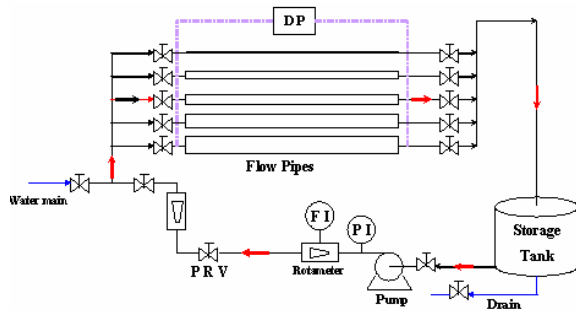


Figure 1. Experimental Setup.

2. Experimental Setup

One of the problems that are facing the industrial companies that deal with the Dead Sea Mud is the mud transport. Unlike pure water transport, mud transport is very complicated and expensive because of both its composition and high viscosity. High mud viscosity results in a very high shear stress while flowing. The high shear stress can be overcome only by having a very high pressure drop that needs to be generated by special pumps.

As it can be seen from Figure 1, the experimental setup consists of five-pipes network consisting of ¼ inch, nominal size pipe branch, a ½ inch branch, a ¾ inch branch, a 1 inch, and 2 inch branch all galvanized, schedule 40 were assembled. The setup can operate as closed or open loop system. The closed loop system consists of a storage tank, a pump, a pressure regulator, two rotameters (low and high range), and a differential pressure gauges (DP). Only the pipe with an inside diameter ½" and length 2m was used in this study and the system operated as closed loop, which consists of a storage tank, a pump, four valves and a manometer to measure the pressure drop. Distilled water was added to the Dead Sea Mud to prepare slurries with four different concentrations.

3. Mathematical Model

Flow of fluids in circular tubes is encountered to be the more economical and rapid transportation method than others, such as those involving conveyor systems. The mathematical model that describes the mud flow inside a pipe is developed based on the basic principles of continuity and momentum equations. The z-component of the Navier-Stokes momentum equation is simplified for steady state, laminar, incompressible and isothermal mud slurry flow in a horizontal pipe, as shown in Fig 1. It was postulated that the only non-vanishing velocity component is the axial velocity (v_z). The axial velocity, for fully developed flow, is a function of radial direction. Simplification of the z-component of momentum equation yields an expression for shear stress as follows:

$$\tau_{rz} = \frac{P_L - P_0}{2L} r \quad (1)$$

Where P_L is the outlet pressure (at $z = L$); P_0 is the inlet pressure (at $z = 0$); L is the pipe length; and r is

the radial direction. The non-Newtonian power law of viscosity, [9], is used for the Dead Sea mud slurry as:

$$\tau_{rz} = -k \left(-\frac{dv_z}{dr} \right)^n \quad (2)$$

Where: k is the flow consistency index and n is the flow behavior index. Inserting Eq. (2) into Eq. (1), rearrange and integrate, then apply the no-slip condition at the wall ($v_z(r = R) = 0$) to determine the integration constant. The final velocity profile expression will be:

$$v_z = \left(\frac{P_L - P_0}{2Lk} \right)^{\frac{1}{n}} \left(\frac{n}{n+1} \right) R^{\frac{n+1}{n}} \left[1 - \left(\frac{r}{R} \right)^{\frac{n+1}{n}} \right] \quad (3)$$

The velocity profile in Eq. (3) can be used to calculate:

1- The slurry maximum velocity ($v_{z,max}$):

The maximum velocity occurs at the centerline ($r = 0$) and has the value

$$v_{z,max} = \left(\frac{P_L - P_0}{2Lk} \right)^{\frac{1}{n}} \left(\frac{n}{n+1} \right) R^{\frac{n+1}{n}} \quad (4)$$

2- The slurry average velocity ($v_{z,average}$):

The average velocity is obtained by dividing the total volumetric flow rate by the cross-sectional area:

$$v_{z,average} = \frac{\int_0^{2\pi R} \int_0^{2\pi R} v_z r dr d\theta}{\int_0^{2\pi R} \int_0^{2\pi R} r dr d\theta} = \left(\frac{P_L - P_0}{2Lk} \right)^{\frac{1}{n}} \left(\frac{n}{n+1} \right) R^{\frac{n+1}{n}} \left[\frac{n+1}{3n+1} \right] \quad (5)$$

3- The slurry volumetric flow rate (Q):

The volume rate of flow is the product of area and average velocity, thus:

$$Q = \int_0^{2\pi R} \int_0^{2\pi R} v_z r dr d\theta = (v_{z,average})(Area) \quad (6)$$

$$= \left(\frac{P_L - P_0}{2Lk} \right)^{\frac{1}{n}} \left(\frac{n}{n+1} \right) R^{\frac{n+1}{n}} \left[\frac{n+1}{3n+1} \right] (\pi R^2)$$

Table 1. Dead Sea and distilled water content (Vol. %) in different runs.

Run Number	Distilled Water	Dead Sea Mud
1	10	90
2	15	85
3	20	80
4	25	75

4. Results and Discussion

Four experimental runs were carried out based on different Dead Sea mud volume fractions, as shown in Table 1. The slurries were prepared by adding distilled

water with volume fractions of 10%, 15%, 20% and 25%, to the Dead Sea mud volume fractions, shown in Table 1. The obtained suspensions, and before being used, were stirred continuously for 30 minutes.

Several tests of slurry runs were carried out at different pressure drops. Prior to each run, the slurry was mixed as stated above for a time sufficient to achieve homogeneous mixture. For each run, a representative sample of the slurry was collected to measure its density and percentage of solid by weight and volume. The results of these measurements are shown in Tables 2, 3 and 4, respectively.

Table 2. Density of Dead Sea Mud Slurry for Different Mud Concentration.

Experimental Run Number	1	2	3	4
Slurry Averaged Density, kg/m^3	1103	1067	1062	1038

Table 3. Percent of solid by weight for different concentrations of the Dead Sea Mud in the slurry

Experimental Run Number	1	2	3	4
Percent of solid by weight	14.53	9.88	8.40	6.99

Table 4. Percent of solid by volume for the slurry with different mud concentrations.

Experimental Run Number	1	2	3	4
Total volume (ml)	390	250	415	236
Volume of solid (ml)	114	61	90	38
Percent of solid by volume %	29.23	24.40	21.69	16.10

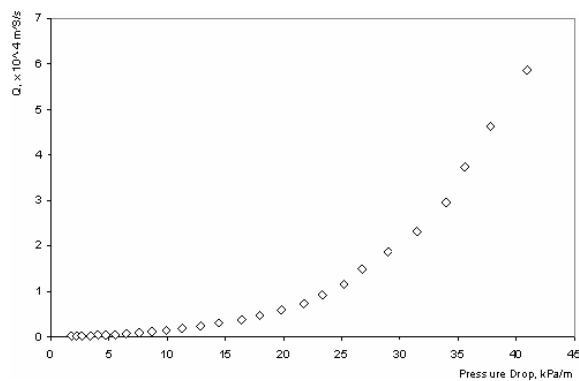


Figure 2. Slurry Volumetric Flow Rate Versus Pressure Drop for the Case of 90% Dead Sea Mud.

Figure 2 shows the operating conditions and measured exit slurry flow rate for the case of 90% Dead Sea mud volume fraction. As Fig. 2 shows, the slurry flow rate has nonlinear relationship with the pressure drop. For small pressure drop, slurry flow rate is almost negligible and changes in linear fashion, and when the pressure drops becomes greater than 10 kPa/m, the deviation from linear behavior starts. The volumetric flow rate versus pressure drop for other slurries with different Dead Sea mud volume fractions are shown in Fig. 3. From this figure, it is obvious that at low pressure drop, 10 kPa/m, there is no

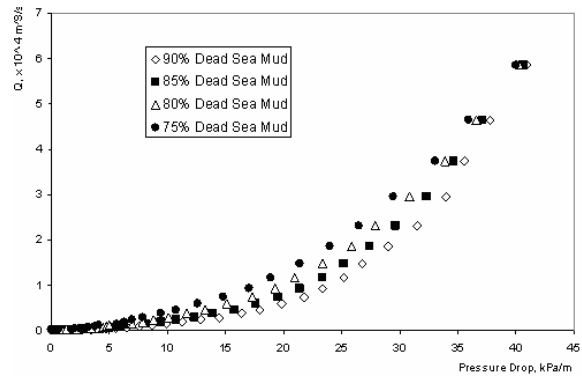


Figure 3. Volumetric Flow Rate Versus Pressure Drop for Slurries with Different Dead Sea Mud Volume Fractions .

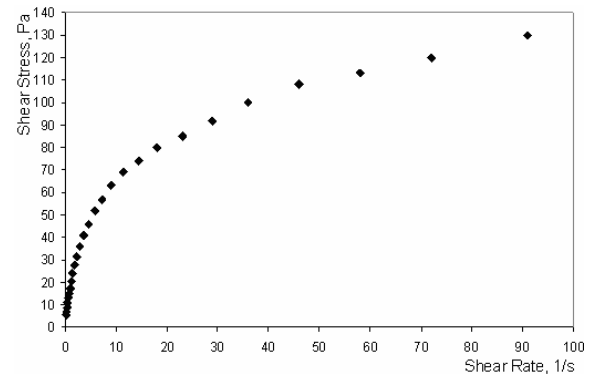


Figure 4. Shear Stress Versus Shear Rate for the Case of 90% Dead Sea Mud.

difference in slurry flow rate at different compositions. Also, at higher pressure drop, 25 kPa/m, the flow rate for the slurry with 75% Dead Sea mud is the highest. This can be explained by the fact that when the volume fraction of distilled water is increased, the slurry density decreases as shown in Table 2, and the slurry tends to behave as a Newtonian fluid where smaller driving force is needed to overcome the resistance to the flow. Also, from Fig 3 one can see that as the Dead Sea mud fraction in the slurry decreases, the volumetric flow rate – pressure drop curves become less concaved. This is seen very clear for the highest water volume fraction in the slurry (25%).

For unidirectional, laminar and steady flow in a circular pipe, the shear stress τ_w , in Pa, at the inside wall of the pipe can be calculated by $\tau_w = (D/4)(\Delta P/L)$ [8,9, and 10], where D is the pipe inside diameter, and $\Delta P/L$ is the pressure drop in Pa/m. The shear stress rate for the flow in the pipe can be calculated as $32Q/\pi D^3$ [10-11], and has a unit (1/s). Fig. 4 presents the experimental data for shear stress at the pipe inside wall versus the mean shear rate for slurry with 90% Dead Sea mud volume fraction. The nonlinear relationship between shear stress and shear rate attests the fact that the used slurry is not Newtonian fluid. Figure 5 shows a comparison between steady state slurry shear stress results for four different slurry compositions (90%, 85%, 80%, and 75% Dead Sea mud volume fractions). From this figure, one can see that the shear stress and shear rate curve for the case of slurry with 90% Dead Sea mud is the highest, while the curve for the slurry with lowest Dead Sea mud content is the lowest. This could be explained by the fact that as more water is added to the slurry, it gets thinner and behaves closer to Newtonian fluid. If large amount of water is added to the

slurry, it is expected that the relationship between shear stress and shear rate, Fig 5, will become linear.

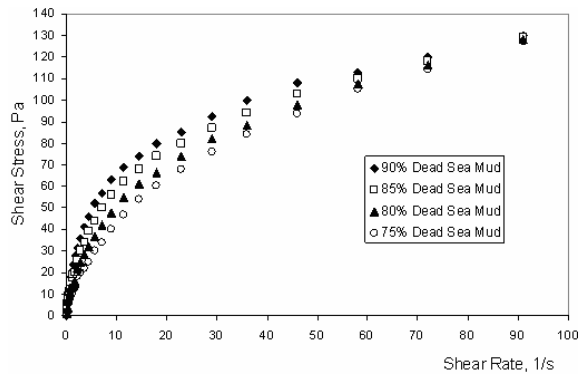


Figure 5. Shear Stress Versus Shear Rate for Slurries with Different Dead Sea Mud Volume Fractions.

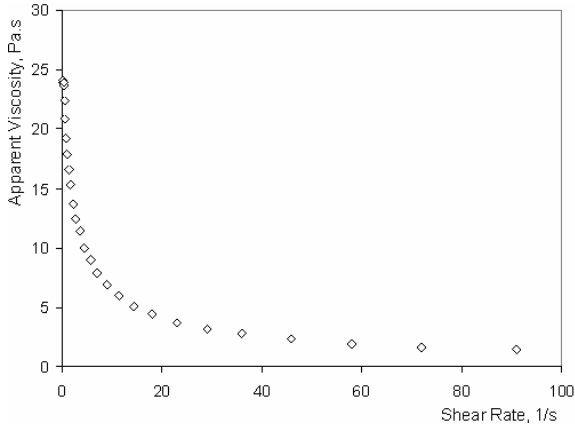


Figure 6. Apparent Viscosity Versus Shear Rate for the Slurry with 90% Dead Sea Mud.

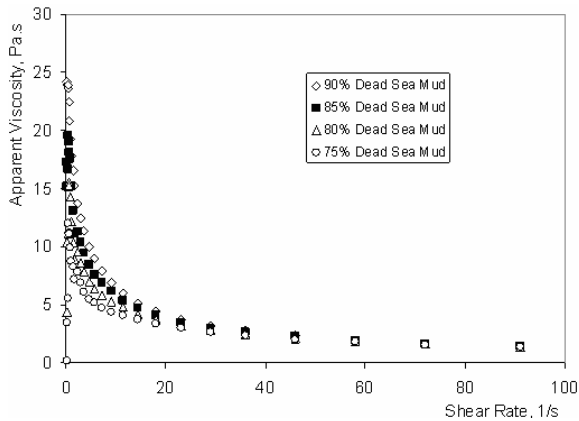


Figure 7. Apparent Viscosity Versus Shear Rate for Slurries with Different Dead Sea Mud Volume Fractions.

From Figures 4 and 5 at low values of flow rates (mean velocities), the profiles are almost linear. Because of the large densities of the slurries (Table 2) in comparison with Newtonian fluid, the straight lines pass through the origin and closer to the shear stress axis. All the trends between shear stress and shear rate attest to the validity of the power law assumption, Eq. (2), made for shear stress.

In order to check whether the obtained results are in good agreement with predictions (power law), the viscosity was expressed as an apparent viscosity. The apparent viscosity, μ_{app} , was calculated at each data point as the shear stress divided by the shear rate. The slurry

composites are restated here, using apparent viscosity versus shear rate as shown in Figure 6. It can be seen from this figure that the viscosity profile shows an exponential decrease as a function of shear rate. Similar trends were observed for slurry with other composition (Figure 7). From Fig., 7 it is obvious that the thinned with increasing shear rate. To understand the exponential decrease behavior between apparent viscosity shear rate, the shear stress power law equation, Eq. (2) is inserted into the apparent viscosity expression to have:

$$\mu_{app} = \frac{\text{shear stress}}{\text{shear rate}} = \frac{\tau_w}{dv_z/dr} = k \left(\frac{dv_z}{dr} \right)^{n-1} \quad (7)$$

Taking the logarithm of both sides of Eq. (7), we obtain:

$$\log(\mu_{app}) = \log(k) + (n - 1) \log \left(\left| \frac{dv_z}{dr} \right| \right) \quad (8)$$

Figure 8 shows the observed behavior between apparent viscosity and shear rate (plotted on a log-log scale for 90% Dead Sea mud slurry). From Equation (8) and when $n = 1$, zero slope in equation (8), the slurry behaves as a Newtonian fluid. This behavior is observed in Fig 8 for small shear rate (less than 0.55/s) where the viscosity of the slurry is about 23.89 Pa.s. Linear regression for high shear rate (from 9 to 100 S^{-1}) gives a negative slope with a value of (-0.6894) from which one can determine that $n = 0.3106$, and an intercept of 1.5087 ($\log k = 1.5087$) from which one can determine that $k = 32.2627 \text{ Pa.s}^{0.3106}$. Because of the fact that the Newtonian fluid behavior region contains few points, the entire region can be fitted using a power law model to have $n = 0.507$ and $k = 17.51 \text{ Pa.s}^{0.507}$. Similar trends were observed for slurries with other compositions (Figure 9). It is clear from this figure that the viscosity is decreasing smoothly for all slurries with increasing shear rate.

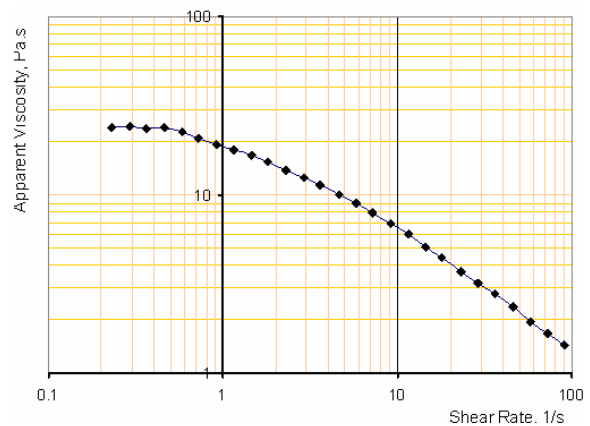


Figure 8. Apparent Viscosity Versus Shear Rate for the Slurry with Dead Sea Mud Volume Fraction of 90%.

Consistency index (k) and flow index (n) in equation (8) were calculated using power regression analysis of the data for apparent viscosity versus shear rate. The results of these calculations at different slurry compositions are tabulated in Table 5 for three cases: a) using all data; b) excluding the data points that result in some scatter of the

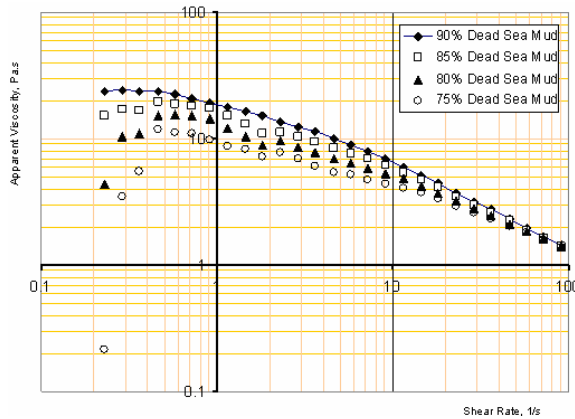


Figure 9. Apparent Viscosity Versus Shear Rate for Slurries with Different Dead Sea Mud Volume Fractions.

Table 5. Comparison Between Calculated Consistency and Flow Indices for Slurries with Different Dead Sea Mud Compositions.

Case	Run 1		Run 2		Run 3		Run 4	
	n	k, Pa.s ⁿ						
a	0.507	17.51	0.5571	13.92	0.6452	9.91	0.8301	5.36
b	0.4479	20.54	0.4855	16.88	0.5289	13.52	0.5955	9.96
c	0.3106	32.26	0.3553	26.12	0.4162	19.83	0.4901	14.29

viscosity at lower shear rate; and c) using the data points at high shear rate that result in linear relationship between apparent viscosity and shear rate. From this table, the calculated flow index is always less than one which means that the slurry is shear thinning. The more shear-thinning the slurry, the greater the friction reduction is. Also, Table 5 shows that when the water content is increased in the slurry, the flow index (n) increases for the above-mentioned three cases. Because flow index, in essence, is a measure of non-Newtonian-ness and for a Newtonian fluid $n = 1$; the increase in the flow index makes the slurry to behave as close as possible to the Newtonian fluid. Table 5 shows that for the three considered cases, we have a viscosity decrease with increasing flow behavior index; this behavior is very consistent with the slurry tendency to behave as Newtonian fluid.

5. Conclusions

Although the behavior of mud flow is complex and the theory of its behavior is not well developed, simplifying assumptions were made to permit an analytical solution

and provide insight into the influence of various parameters on the results of the laboratory tests.

This paper highlights the importance of a thorough rheological analysis of non-Newtonian fluids such as Dead Sea mud slurry. Power law was used to accurately represent the interaction between shear stress and viscosity and velocity gradient. Apparent viscosity – shear rate relation exhibits very valuable profiles to determine both flow consistency index and flow behavior index. The developed mathematical model could predict the flow rate of Dead Sea mud slurry through a pipe under the conditions of applied pressure drop. Experimental work showed that the slurry with low Dead Sea mud content behaves closer to Newtonian fluid.

References

- [1] A. Al-Khlaifat, "Dead sea rate of evaporation". American Journal of Applied Sciences, Vol. 5, No. 8, 2008, 934-942.
- [2] A. Khlaifat, O. Khashman, "Physical and chemical characterization of Dead Sea mud". submitted for possible publication to Journal of Materials Characterization.
- [3] R. Schiffner, J. Schiffner-Rohe, M. Gerstenhauer, M. Landthaler, F. Hofst dter, W. Stolz, "Dead Sea treatment - principle for outpatient use in atopic dermatitis: safety and efficacy of synchronous balneophototherapy using narrowband UVB and bathing in Dead Sea salt solution". Euro J Dermatol, Vol. 12, No. 6, 2002, 543-548.
- [4] S. Halevy, S Sukenik, "Different modalities of spa therapy for skin diseases at the Dead Sea area". Arch Dermatol, Vol. 134, No. 11, 1998, 1416-1420.
- [5] S. Bellometti, M. Poletto, C. Gregotti, P. Richelmi, F. Berte, "Mud bath therapy influences nitric oxide, myeloperoxidase and glutathione peroxidase serum levels in arthritic patients". Int J Clin Pharmacol Res, Vol. 20, No. 3, 2000, 69-80.
- [6] S. Sukenik, D. Buskila, L. Neumann, A. Kleiner-Baumgarten, "Mud pack therapy in rheumatoid arthritis". Clin Rheumatol, Vol 11, No. 2, 1992, 243-247.
- [7] R. Haldenwang, P. T. Slatter, S. Vanyaza, R. P. Chhabra, "The effect of shape on laminar flow in open channels for non-Newtonian fluids". J Hydrotransport, Vol 16, 2004, 311-324.
- [8] Bird R B, Stewart W E, Lightfoot E N. Transport phenomena. 2nd ed. New York; John Wiley & Sons; 2002.
- [9] Noel de Nevers. Fluid mechanics for chemical engineers. 2nd ed. McGraw-Hill; 1991.
- [10] Wilkes J O. Fluid mechanics for chemical engineers. Prentice Hall; 1999.
- [11] J. Billingham, J. Ferguson, "Laminar unidirectional flow of a thixotropic fluid in a circular pipe". J. Non Newtonian Fluid Mech, Vol. 47, 1993, 21-55.

Japanese Manufacturing Techniques and Practices: An Indian Perspective

Jamal A. Farooquie^{a,*}, Asit B. Mohapatra^b

^aDepartment of Business Administration, Aligarh Muslim University (AMU), Aligarh-202002, India.

^bReliance Retail, Mumbai, India.

Abstract

With rapid advancement in technology and availability of workforce at reasonable wages, India is becoming a preferred location for manufacturing companies from all over the world. The manufacturing sector in India has witnessed a growth of about 15 percent during the year 2007. Japanese techniques like kaizen, quality circles, total productive maintenance, and just-in-time, etc. have been implemented worldwide by various manufacturing organizations to improve their performance and competitiveness. The extent of success achieved has, however, been influenced significantly by the structure and culture of the organization concerned and the country as well. The present article attempts to study the experiences of a few selected Indian manufacturing organizations, operating in and around New Delhi region, regarding the implementation and adaptability of popular Japanese manufacturing techniques and practices. A structured questionnaire containing both open and close-ended questions is used for data collection. The results are obtained using descriptive analysis, hypothesis testing, and correlation analysis. Though implementation of Japanese manufacturing techniques and practices (JMTPs) has resulted in improvement of various production-related dimensions and other benefits, there is still a need to understand how to harbor such techniques and practices for the long-term growth and benefit of the organizations on the whole.

© 2009 Jordan Journal of Mechanical and Industrial Engineering. All rights reserved

Keywords: Indian Manufacturing; Japanese Manufacturing Techniques and Practices; Productivity; Competitiveness.

1. Introduction

Manufacturing plays an important role in the economy of every nation. In India, manufacturing accounts for about 17% of the GDP and 12% of employment. Indian manufacturing sector shares three-fourths of all exports from India [1]. There has been a growth of around 15 percent in this sector in the year 2007. Product and process innovations, technological developments, improved managerial skills, and the availability of low cost workforce are the potential competitive capabilities of India's manufacturing. There are, however, several other aspects, which the country needs to address in order to improve its competitiveness in the global manufacturing scenario. Industries all over the world have been focusing on the technological and managerial dimensions of their operations to improve their performance and competitiveness.

Apart from such tools and techniques, Japan has conceived and evolved many other techniques and practices for improving the organizations' performance and competitiveness. Kaizen (continuous improvement), just-in-time (kanban), quality circles, total productive maintenance, poka-yoke, zero defects, and cellular

manufacturing, etc. are among those techniques and practices that have been adapted by industries, particularly manufacturing ones, in various developed and developing countries. The culture of the organization concerned and that of the country, however, have a strong bearing on the extent to which these Japanese manufacturing techniques and practices (JMTPs) make their impact as desired. Ford and Honeycutt [2], in a comprehensive article, have discussed the relevance of the culture of a country in understanding the country's business practices. They have also established that corporate culture is company-specific, and therefore generalization of any company-specific observations can be misleading. It is, perhaps, for this reason why researchers have been addressing issues like adoption, implementation, and effectiveness of various Japanese techniques and management practices in the manufacturing sector of different countries. Examples of such studies include that in the USA, Singapore, Korea, and Scotland [3-6].

The Indian manufacturing ranks 2nd, just after Japanese manufacturing, in terms of Deming awards per country. There are about 13 companies that have won this award and many others are ISO-9000 certified [7]. Till the last couple of years of the 20th century, however, practices like statistical process control (SPC), total quality management (TQM), just-in-time (JIT), total productive maintenance (TPM), cellular manufacturing, and continuous improvement either failed to serve their purposes in the

* Corresponding author. jamalfarooquie@yahoo.co.in

Indian manufacturing organizations or to even receive any attention from this sector [8].

In this context, and as inspired by the findings like that of Ford and Honeycutt [2], the authors have made an attempt to study the present scenario of Indian manufacturing with reference to the implementation and effectiveness of some popular Japanese manufacturing techniques and practices. This has further helped the authors assess the adaptability of these techniques and practices in the Indian context.

2. Some Previous Studies

This section explains briefly the Japanese manufacturing techniques and practices under study and presents a brief overview relevant literature. *Kaizen (KZN)* is based on making small changes on a regular basis - reducing waste and continuously improving productivity, safety, and effectiveness. While *Kaizen* has historically been applied in manufacturing settings, it is now becoming common to find it applied to service business processes as well [9, 10].

The basic principle of *Just-in-Time (JIT)* is to eliminate all forms of waste, and is defined as anything that does not add value to the product [11]. *JIT* applies primarily to repetitive manufacturing. Research has shown that successful implementation of the *JIT* philosophy can produce significant benefits for manufacturing firms such as improving quality, minimizing levels of inventory, improving relationships with suppliers [12], reducing the labour turnover rate, reducing manufacturing lead times, reducing set-up time [13], reducing operations and materials handling costs, and maximizing the use of space [14].

Quality Circle (QC) is a management tool that has many benefits for various work environments such as control and improvement of quality, more effective company communication, utilization of employees' problem solving capabilities, and more job involvement. Literature presents numerous studies such as those by Park [15] and Mandal *et al.* [16], on quality circles and other quality related practices. Better quality and enhanced productivity have been among the major benefits of practicing *QCs*. *Total Productive Maintenance (TPM)* is a manufacturing program designed primarily to maximize the effectiveness of equipment throughout its entire life by the participation and motivation of the entire workforce. The benefits from implementing *TPM* have been well documented at numerous plants. *TPM* management brings everyone, from equipment designer to operators, together to work under an autonomous and small group environment [17].

The 5-S Philosophy focuses on effective work place organization and standardized work procedures. 5-S simplifies work environment and reduces waste and non-value activity while improving quality, efficiency and safety. The five Ss in the Japanese language are Seiri (sort), Seiton (set-in-order), Seiso (shine), Seiketsu (standardize), and Shitsuke (sustain). *Single Minute Exchange of Dies (SMED)* is an approach to reduce the loss of output quantity and quality that occurs due to changeovers and set-up activities. The method has been developed in Japan by Shigeo Shingo and has proven its

effectiveness in many companies by reducing changeover times from hours to minutes.

The Japanese concept *Poka-yoke (PKYK)*, mistake-proofing, is oriented towards both finding and correcting problems as close to the source as possible. There are six mistake-proofing principles or methods, namely, elimination, replacement, prevention, facilitation, detection, and mitigation. Process improvement is among the major outcomes of poka-yoke implementation [18]. *Zero Defect (ZD)* method endorses continuous improvement. The *ZDs'* objectives are limited to quality improvement, whereas, *QCs* aim at improvement in quality, methods, morale, and motivation. The focus of *ZD* programs is to produce as little defectives as possible, theoretically no defectives.

A *Work Improvement Team (WIT)* is formed to improve the work processes in an organization. There are multiple reasons, anything from improving quality of products to that of processes or systems, etc., for which an organization chooses to implement *WITs*. *Cellular Manufacturing (CM)* is a philosophy that attempts to recognize and exploit similarities among components to be manufactured and to group them into families based on these similarities in shapes, production processes, or on both [19]. Comprehensive reviews of different cell design approaches and their features are presented by several researchers including that by Mansouri *et al.* [20].

3. Objectives and Methodology

Manufacturing covers a large variety of operations and products and hence a huge number of organizations. Many organizations, out of this population, use one or more *JMTs*. Since these organizations are scattered all over the country, and also a true sampling frame of such organizations was not available, judgmental sampling method has been used to draw the sample with the help of personal references of the authors and the professional bodies in the country like CII and ASSOCHAM. Presuming that larger organizations can provide us with more useful data, annual turnover was chosen as the criterion to select the sample companies. Manufacturing organizations with an annual turnover of Rs. 1 billion (US\$ 20 million) and above are included in the study. Moreover, administrative and other limitations, like that of time and cost, restrict the scope of this study to the regions in and around New Delhi. A preliminary survey was also conducted to finalize the list of the *JMTs* to be included in the study. Data availability has been the major criterion for this selection. Non-inclusion of the *JMTs* that are left out of the study does not seem to affect the validity and reliability of the findings, as previous researchers too have not necessarily considered all of them together.

This study aims to determine (i) the implementation status of *JMTs* and their effectiveness, (ii) the relative importance of various triggers, facilitators, barriers, outputs, and benefits and also their effect on *JMTs* effectiveness, (iii) the effect of those triggers, facilitators, and barriers along with the stage of *JMTs* development on the benefits and outputs, (iv) the correlation among the various variables of the study, and (v) adaptability of *JMTs* in the Indian context. A structured questionnaire, consisting of 15 items, was designed to collect data. The

questionnaire, along with a brief write up was sent to the executives of 170 companies, selected through the above-mentioned procedure and criteria. With a low response rate of about 32 percent, 54 completed questionnaires were received back and of them, 35 were found valid. The results are obtained by using descriptive analysis, multiple regression method to test hypotheses, and coefficient of correlation. Percentage in fraction has been rounded off to the nearest number while analyzing the data.

4. Analysis and Findings

The first three questions in the questionnaire deal with the profile of the organizations. Next six questions are designed to collect data on the JMTPs and their implementation and effectiveness. Another set of questions (10-14) has been used for gathering information on variables like triggers, facilitators, barriers, benefits, and outputs. The last question invites opinions of the respondents on adaptation of JMTPs in the Indian context.

4.1. Organizations Profile

According to the number of employees, the sample organizations can be classified into three classes - those employing less than 2500 employees (54%), 2500-4999 (32%), and those with 5000 or more employees (14%). The annual turnover-wise distribution of the organizations exhibit that the majority (37%) have annual turnovers of Rs. 10 billion or above, 11% each with Rs. 7.5-10 billion and Rs. 5-7.5 billion, 18% with Rs. 2.5-5 billion, and the annual turnover of the remaining 23% has been Rs. 10-25 million. This pattern could have emerged possibly due to the fact that organizations that have more resources at their disposal are more flexible in experimenting with techniques and practices other than traditional ones. Nearly two-thirds of the organizations (66%) have reported that they have a joint venture with at least one foreign company. This figure may be interpreted as an indication that foreign tie-ups could be one of the reasons for which organizations adopt a JMTP to align themselves with the best global practices, as also to compete with their global players. The foreign partners belong to the countries like France, Japan, Germany, USA, and UK. The organizations having just 1-2 years old joint venture with any foreign country, and those with no such tie-ups account for 43% (15 out of 35). Around 35% have been operating jointly with a foreign company for over 10 years. The age of the joint venture for 14% of the companies has been between 3-5 years, and that of the remaining 8% is 6-10 years.

4.2. Implementation and Effectiveness of JMTPs

Table 1 presents the distribution of the organizations implementing various JMTPs, the length of implementation, the stage of development, and the effectiveness (in terms of mean score) of each JMTP. The findings reveal that 5-S and KZN have been implemented in most of the organizations, followed by WITS, QCs, TPM, and JIT. PKYK and SMED are, however, rarely adopted by Indian manufacturers. A survey of 34 industries conducted in 2002 by Kumar and Garg [21] has reported a positive attitude of around 60 percent of the respondents towards JIT implementation. A recent study [22] on JIT practices in Indian manufacturing concludes

that the art of designing the right strategy for implementing JIT is still debatable. 5-S, being oriented towards a healthy work atmosphere and based on behavioral changes, rather than physical ones, has been relatively inexpensive to implement than other JMTPs. Rane *et al.* [23] has found companies, particularly in automobile sector, using 5S effectively as a stepping-stone for JIT implementation. The low usage of SMED may be attributed to the nature of business under which most of the Indian companies operate where, unless the production limits of the company are stretched beyond compliance, the targets necessitate faster changeovers of machinery and production setup. Thus, SMED was not found suitable.

This can be observed from Table 1 that almost in each case the majority of organizations had been practicing the JMTP for over two years (at the time of data collection). Moreover, most of the JMTPs in use, except ZD, PKYK, and SMED, are found in their well-developed stage of implementation. While investigating the respondent's understanding of the various stages of implementing JMTPs, their explanation was that a well-developed stage is achieved when the practice has been totally internalized or institutionalized, which means even the shop floor workers know and practice the JMTP in question.

As far as the effectiveness of these techniques is concerned, Kaizen was rated as the most effective technique with mean as 4.27 followed by 5-S (3.65). Besides these, JMTPs that were found to obtain scores above the median were TPM (2.78), WITs (2.56) and QCs (2.51). The respondents were asked to explain the factors they took into account when assessing the effectiveness of JMTPs. A clear-cut response format was not found due to the complexities involved in measuring the intangible benefits of JMTPs. Number of people participating in the JMTP, monetary benefits like cost cutting, material consumption, productivity, lead-time and output, and change in work culture like employees becoming more customer-oriented and taking on more responsibilities were, however, found as the key considerations. The most ineffective techniques among all the JMTPs under study are CM and JIT. A possible reason for low implementation & effectiveness of JIT could be that many of the suppliers of the organizations in question are small-scale firms, and they do not have the capability and resources to match the strict requirements laid down by JIT.

The findings also indicate that a given JMTP does not necessarily score high on the effectiveness scale despite it being well-developed. For example, the practice of QCs has been developed well in 73 percent of the organizations implementing it as against 66 percent in the case of Kaizen and 5-S. QCs however, have not been as effective as Kaizen and 5-S.

Effectiveness being an important resulting parameter of JMTP implementation, a null hypothesis (H01) was formed to investigate the statistical relationship, if any, between the effectiveness of a JMTP and the combined effect of four relevant independent variables. These variables are stages of development of the JMTPs, annual turnover, facilitators to JMTPs implementation, and the size of the organization (number of employees). The null hypothesis was stated as "the coefficient of multiple determination in the population is zero". This is equivalent

Table 1. Implementation and Effectiveness of JMTPs.

JMTP	No. of Orgns.	Length of Implementation			Stage of Development			Effectiveness Score
		Up to 1 year	1 – 2 years	Over 2 years	Well developed	Growth	Introductory	
KZN	29 (83%)	5 (18%)	3 (10%)	21 (72%)	19 (66%)	8 (28%)	2 (6%)	4.27
JIT	16 (46%)	3 (19%)	2 (12%)	11 (69%)	9 (56%)	6 (38%)	1 (6%)	1.91
QCS	22 (63%)	3 (14%)	2 (9%)	17 (77%)	16 (73%)	5 (23%)	1 (4%)	2.51
TPM	19 (54%)	4 (21%)	2 (11%)	13 (68%)	8 (39%)	9 (50%)	2 (11%)	2.78
5-S	32 (91%)	3 (9%)	6 (19%)	23 (72%)	21 (66%)	7 (22%)	4 (12%)	3.65
SMED	7 (20%)	NIL	2 (29%)	5 (71%)	1 (20%)	6 (80%)	NIL	1.10
PKYK	11 (31%)	1 (9%)	2 (18%)	8 (73%)	7 (64%)	3 (27%)	1 (9%)	1.65
ZDS	13 (37%)	3 (23%)	3 (23%)	7 (54%)	5 (38%)	7 (54%)	1 (8%)	1.32
WITS	24 (69%)	3 (13%)	3 (13%)	18 (74%)	17 (68%)	7 (32%)	NIL	2.56
CM	13 (37%)	4 (30%)	1 (8%)	8 (62%)	7 (54%)	5 (38%)	1 (8%)	1.20

For abbreviations pl refer to section 2.

Table 2. Statistical Tables.

Statistic	H ₀₁		H ₀₂		H ₀₃	
<i>Multiple regression</i>						
Multiple R	0.297		0.328		0.363	
R ²	0.088		0.108		0.131	
Adjusted R ²	-0.033		0.021		0.016	
Std. Error	1.0908		0.661		0.299	
<i>F test</i>	Reg	Res	Reg	Res	Reg	Res
D.o.f.	4	30	4	30	4	30
Sum of sqs	3.457	35.696	1.633	13.529	0.405	2.678
Mean sq	0.864	1.190	0.544	0.436	0.101	0.089

to saying that the coefficient of each independent variable in the multiple regression equation is equal to zero.

The hypothesis is tested using multiple regression and F statistics. At 5% level of significance, the hypothesis is found statistically accepted (Table 2). This means the overall effect of the four independent variables on the effectiveness of JMTPs is insignificant. This might have happened due to either insufficient data or the fact that the overall culture of an organization matters a lot in how JMTPs perform.

4.3. Triggers, Facilitators, Barriers, Outputs, and Benefits

Triggers of any process are the factors responsible for its initiation. The major factors that have been considered important, based on this study and as extracted from the literature, for the initiation of various JMTPs include the need (a) to reduce manufacturing cycle time, production cost, waste, and inventory, and (b) to improve on production flexibility, size of the organization, and market share. Initiatives were also taken to implement JMTPs, as this was insisted by the customers or by the presence of a joint venture with a foreign company, particularly from Japan. The need to reduce waste, production cost, and

inventory has scored high (mean scores as 4.48, 4.22 and 4, respectively) on a 5-point scale of importance. Whereas, presence of a joint venture, concern over declining market share, and customers' insistence were rated on the lower side of the scale with mean scores as 2.58, 2.48, and 2.29, respectively. The aim of reducing manufacturing cycle time, enhancing production flexibility, or right sizing an organization, has played an important role in JMTPs implementation, but scoring only between 4 and 3 on the scale.

Eight factors were considered as facilitators in the implementation of various JMTPs. In order of their increasing importance (on a 5-point scale), the factors are incentives given to employees, organizational structure, linking business goals to JMTPs, organizational and individual discipline, internal & external benchmarking, top management initiatives, effective communication, and training programs.

The respondents were found reluctant in mentioning barriers to JMTPs implementation. This hesitation can be understood because identification of any such factor may reflect some negative aspects of their organization's policies. Five factors are, however, considered by them as barriers to JMTPs implementation. Resistance from

employees and lack of expertise have emerged out as the two most obstructing factors with their respective mean scores as 2.32 and 2.12 on a 5-point rating scale. The other barriers that have been found relatively less influential are changes required in the organizational structure (2.03), perceived cost of implementation (1.97), and lack of commitment at the top management level (1.90). Literature reports several barriers in JMTP adoption in India. For example, regarding implementation of TPM in the Indian context, a study [24] finds TPM by no means an easy task as a variety of internal and external barriers exist.

Outcomes of JMTPs implementation have been measured in the form of production-related outputs (more of quantitative nature) and benefits (more of qualitative nature). Figure 1 presents the mean score of each output, as obtained through the responses measured on a 5-point scale. Inventory levels, overtime requirements, raw materials consumption, maintenance costs, workforce requirements, and manufacturing cycle time have decreased marginally or significantly as a result of using one or more JMTPs. On the other hand, JMTPs have resulted in the improvement of product quality, on-time deliveries, and output per shift. A worldwide scenario of Japanese production and manufacturing techniques has been presented by Blakemore [25], and is supporting the findings of this study. Higher quality levels, lower costs and shorter production times are highlighted as the major outcomes of implementing such techniques all over, including the countries like USA, France, Australia, China and Germany.

The respondents were also asked to show their degree of agreement on a similar 5-point Likert scale with the statements regarding the benefits of the JMTPs being practiced in their organizations. The results indicate that organizations have experienced improvement in team coordination, employees efficiency, employees ability to take initiatives, work culture, sense of responsibility among the employees, employees motivation and morale, quality consciousness, customer-orientation, profit margin, and market share. Employee turnover, absenteeism, and number of complaints from the customers were found decreasing in the organizations practicing one or more JMTPs (Figure 2).

Factors responsible for taking an initiative to implement a JMTP and for facilitating or obstructing this implementation may be diverse for different organizations, but each organization looks forward to many returns as possible. It is quite rational to assume that such factors have some effect on how productive and beneficial a JMTP is. Statistical investigation to this effect, therefore, seems to be justified at this juncture. Two null hypotheses regarding outputs and benefits, H_02 and H_03 respectively, were formulated and tested on the same lines, as was done for H_01 . The combined effect of the facilitators, triggers, barriers, and stage of development is examined on the outputs and benefits separately, using multiple regression and F statistic. It is found that the combined effect of the four variables on the outputs and the benefits are statistically insignificant (Table 2). The results, however, do not appear to be in line with a non-statistically assumed relationship among such variables. Apart from the inadequacy of data, leaving many other variables out of the study may have a significant bearing on these results.

Organization culture, the manner in which a JMTP is implemented, and whether an organization is public, private, national, or multinational, are examples of those variables.

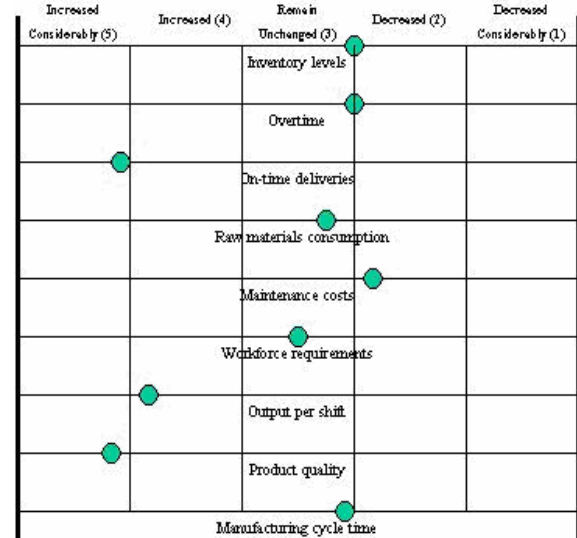


Figure 1. Responses on output.

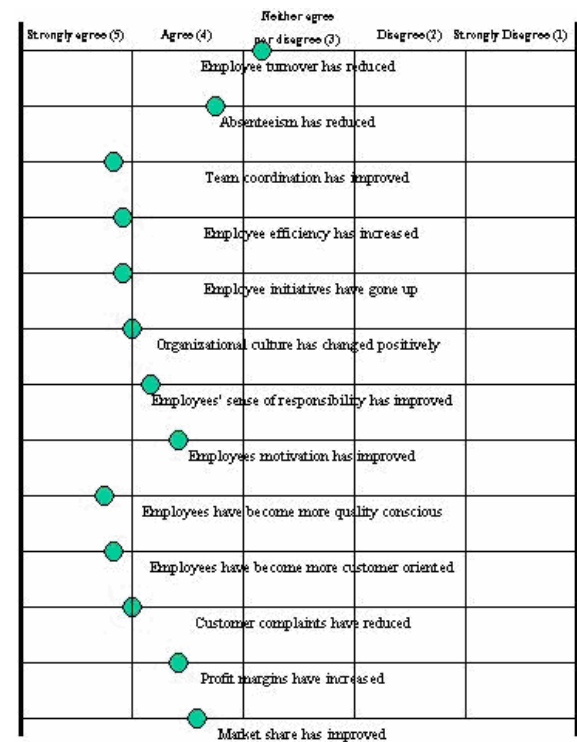


Figure 2. Responses on benefits.

4.4. Correlations

Finally, a correlation analysis is conducted to determine the mutual relationships and their directions among the variables involved in the study. Triggers, facilitators, barriers, effectiveness, outputs, benefits, stage of development, age of the joint venture, annual turnover, and size of the organization have been considered for this part of the analysis. At 5% or better level of significance, only three relationships were found significant. These relationships are between benefits and outputs (0.417, $p < 0.05$); age of joint venture and stage of development

(0.499, $p < 0.01$); and annual turnover and barriers (0.467, $p < 0.01$). A significant positive correlation between the outputs and benefits of JMTPs seems to be justified, as these variables are, in fact, two different forms of the results that an organization achieves through implementation of JMTPs.

Age of the joint venture in an organization and the stage of development of the JMTPs implemented there are also found to co-vary in the same direction. Reasoning behind this relationship may be that a foreign partner, which has already reaped the benefits of JMTPs in its home country, attempts to inculcate the same culture in the Indian company, too. However, in the section that deals with triggers, it was revealed that a joint venture with a foreign company has not been a major factor responsible for JMTPs implementation in the Indian companies. These two findings related to a possible relationship between the presence of a joint venture and JMTPs effectiveness reflect some contradiction. The importance of a joint venture was measured along with eight other factors. So it is possible that this factor scores relatively lower than some others on the importance scale. This argument is supposed to remove the element of contradiction referred above.

Annual turnover of an organization and barriers to JMTPs implementation are surprisingly found correlated and that too with a +ve sign. Apparently, going for a JMTP, even on an experimental basis, is easier for a company with a high turnover as it can safely absorb adverse (financial) results, if any. On the other hand, three out of the five barriers identified in this study, namely, resistance from employees, lack of commitment at the top level, and fear of organizational changes, might be more dominating as barriers in companies with high turnover. If this is true, it may be accepted that the higher the annual turnover the stronger are the obstructions in JMTPs adaptation.

5. Conclusions

The manufacturing sector is so vast and diversified that the findings of any study, based on a small sample and with the inclusion of only a limited number of variables, cannot be safely generalized for the whole sector. This study also has a limited scope of application for the same reasons. It is, however, believed that the findings of this study shall be useful as suggestive guidelines for those manufacturing organizations in the country that are planning to implement Japanese manufacturing techniques and practices in order to enhance their productivity and improve competitiveness. The major findings are listed below.

- 5-S is the most widely used techniques followed by Kaizen. Effectiveness-wise, it is the other way round. JIT and CM are on the lower end of the effectiveness scale.
- The need to reduce waste, production cost, and inventory has triggered the implementation of JMTPs in most of the cases.
- Resistance from employees and lack of expertise have emerged out as the major barriers to JMTPs implementation, whereas training programs and effective communication channels have facilitated the implementation process most.
- Improved product quality, increased on-time deliveries, and reduced inventory levels have been the major outputs of JMTPs implementation. Team spirit, quality consciousness, and attitude towards work have also improved.
- The combined effect of the stage of development, annual turnover, facilitators, and size of the organization on effectiveness of a JMTP are insignificant.
- The facilitators, triggers, barriers, and stage of development combined together do not make any significant effect on the outputs and benefits of JMTPs.
- The correlations between benefits and outputs; age of joint venture and stage of development; annual turnover and barriers are found positive and significant.

Based on the analysis and interpretation of the data, this may be concluded that achieving successful implementation of Japanese techniques and practices is not an issue for Indian manufacturing. The issue is, however, how to harbor such practices for the long-term growth and benefit of the organizations on the whole. The study, therefore, recommends that organizations intending to go for any JMTP should first understand the need to use that JMTP and its application, prepare for its adaptation, and then identify the ways and measures required for its successful implementation.

References

- [1] National Manufacturing Competitiveness Council. The national strategy for manufacturing report. New Delhi; Mar 2006.
- [2] J.B. Ford, E.D. Honeycutt, "Japanese national culture as a basis for understanding Japanese business practices. *Business Horizons*, Nov-Dec 1992, 27-34.
- [3] H.I. Jin, M.L. Sang, "Implementation of just-in-time systems in US manufacturing firms". *International Journal of Operations & Production Management*, Vol 9, No. 1, 1989, 5-14.
- [4] H. Sin-Hoon, N. Yong-Tjoon, "A study on just-in-time practices in Singapore". *International Journal of Operations & Production Management*, Vol 15, No. 6, 1995, 5-24.
- [5] Y.L. Choong, "The adoption of Japanese manufacturing management techniques in Korean manufacturing industry". *International Journal of Operations & Production Management*, Vol 12, No. 1, 1992, 66-81.
- [6] G. Mould, M. King, "Just-in-time implementation in the Scottish electronics industry". *Industrial Management & Data Systems*, Vol 95, No. 9, 1995, 17-22.
- [7] Summit on Indian Manufacturing Competitiveness. *Indian manufacturing in a global perspective: Setting the agenda for growth*. Report, Deloitte Research; 2005.
- [8] P. Chandra, T. Sastry, "Competitiveness of Indian manufacturing- Findings of the 1997 manufacturing futures Survey". *Vikalpa*, Vol 23, No. 3, 1998, 25-36.
- [9] R. N. Cheser, "The effect of Japanese kaizen on employee motivation in US manufacturing". *International Journal of Organizational Analysis*, Vol. 6, No.3, 1998, 197-212.
- [10] M. L. Emiliani, "Improving business school courses by applying lean principles and practices". *Quality Assurance in Education*, Vol. 12, No. 4, 2004, 175-187.
- [11] J. M. Burnham, "Some conclusions about JIT manufacturing". *Production and Inventory Management Journal*, Vol. 28, No. 3, 1987, 7-10.

- [12] S. M. Aghazadeh, "JIT inventory and competition in the global environment: A comparative study of American and Japanese values in auto industry". *Cross Cultural Management*, Vol 10, No. 4, 2003, 29-42.
- [13] M. A. Wafa, M. M. Yasin, "A conceptual framework for effective implementation of JIT: An empirical investigation". *International Journal of Operations and Production Management*, Vol 18, No. 11, 1998, 1111-1124.
- [14] P. Petersen, "The misplaced origin of just-in-time production methods". *Management Decision*, Vol. 40, No.1, 2002, 82-90.
- [15] S. J. Park, "Estimating success rates of quality circle programs: public and private experiences". *Public Administration Quarterly*, Vol 15, No.1, 1991, 133-146.
- [16] P. Mandal, P. E. D. Love, A. S. Sohal, B. Bhadury, "The propagation of quality management concepts in the Indian manufacturing industry: some empirical observations". *The TQM Magazine*, Vol 12, No. 3, 2000, 205-213.
- [17] C. J. Bamber, J. M. Sharp, M. T. Hides, "Factor affecting successful implementation of total productive maintenance: A UK manufacturing case study perspective". *Journal of Quality in Maintenance Engineering*, Vol 5, No. 3, 1999, 16-18.
- [18] M. Fisher, "Process improvement by poka-yoke". *Work Study*, Vol 48, No. 7, 1999, 264-266.
- [19] F. A. Mubarak, B. M. Khumawala, C. Canel, "Focused cellular manufacturing: An alternative to cellular manufacturing". *International Journal of Operations and Production Management*, Vol 23, No. 3, 2003, 277-299.
- [20] S. A. Mansouri, S. M. Hussein, S. T. Newman, "A review of the modern approaches of multi criteria cell design". *International Journal of Production Research*, Vol 38, No. 5, 2000, 1201-1218.
- [21] V. Kumar, D. Garg, "JIT elements in Indian context: an analysis". *Productivity*, Vol. 41, No. 2, 2002, 217-222.
- [22] V. D. Wakchaure, M. A. Venkatesh, S. P. Kullurkar, "Review of JIT practices in Indian manufacturing industries". *Proc. IEEE Int Conference on Management for Innovation and Technology*, 2006, 1099-1103.
- [23] S. B. Rane, A. V. Bhosale, S. S. Mantha, S. G. Aravandekar, "Effective JIT implementation using 5's philosophy". *Proc. of GCMM-2004 Int Conference*, Vellore, 2004, 260-265.
- [24] I. P. S. Ahuja, J. S. Khamba, "Strategies and success factors for overcoming challenges in TPM implementation in Indian manufacturing industry". *Journal of Quality in Maintenance Engineering*, Vol. 14, No. 2, 2008, 123-147.
- [25] J. Blakemore, "Japan Manufacturing Tour". *Manufacturing Society of Australia*, Nov 2006, www.mansa.org.au, Accessed on Feb 2009.

Automatic Control of Electrodes in Lithotripsy Machine

J. Al-Nabulsi, H. Amasha, B. Altrabsheh, B. Al-Naami

Biomedical Engineering Department, Faculty of Engineering, Hashemite University, Zarqa, Jordan

Abstract

Extracorporeal shock wave lithotripsy (ESWL) employs high-energy shock waves that propagate through the body and focus on the stone to break it into small grains, which travel out of the body along with the urine. The distance between lithotripsy long-life electrodes tends to vary after every session. This variation causes an associated pain for the patient, and hence the need for re-calibration and adjustment of the distance. Both manual calibration and adjusting procedure are time wasting, inaccurate, and must be performed by an expert operator.

In this paper, a mathematical model has been developed to predict the number of shocks needed for every patient, depending on input information regarding his age, stone size, and location. An automatic adjustment procedure for the distance between electrodes, utilizing a proportional integral derivative controller, is also proposed in order to increase treatment effectiveness and to reduce patient pain. This also enables better planning of treatment and allows the possibility for any operator to use, and thus resulting in a better utilization of apparatus. Results from trials in a hospital were adequate, and the experimental data matched those predicted by the model.

© 2009 Jordan Journal of Mechanical and Industrial Engineering. All rights reserved

Keywords: Solar Still; Lithotripsy; Kidney Stones; Shock-Waves.

1. Introduction

Extracorporeal Shock Wave Lithotripsy is a technique for destructing stones in the kidney and ureter into smaller particles that can be disposed of by the urine system, and this spares the patient the agony of surgery. This technique still imposes some pain and problem in the planning procedure [1]. Several researchers have proposed models to reduce the amount of pain and wasted time accompanied this process [2, 3]. There are two main types of lithotripsy electrodes which are used in hospitals and clinics: the first type is the disposable electrode shown in Figure 1a, which has the function of discharging the electrical shock wave, and this type is used for only one session. The other type is the adjustable electrode, shown in Figure 1b and known as the long life electrode where it can be used up to 50 sessions. Both electrodes could be either flat or conical depending on the electrode shape. In this paper, the second type has been investigated where a new method for automatically adjusting and controlling the distance or the gap between the electrodes is presented (Refer to Figure 1).

At present, the non-disposable long life lithotripsy electrode gap is adjusted manually by the doctor or the physician where it can be performed by placing a calibrated and a well-known thickness of metal sheet directly in the gap between the electrodes heads and manually adjusting the venire to the desired thickness [4]. This process is time consuming and exposes the patient to more pain than necessary. The main objective of this

research is to introduce a scientific and a reliable way to automatically control and adjust the long life electrodes. This should increase the treatment effectiveness and further reduce patient's pain.

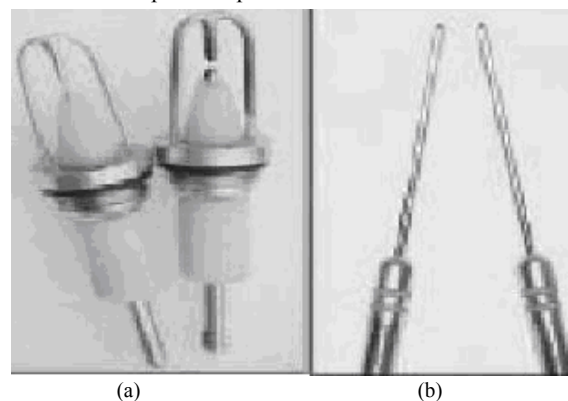


Figure 1. (a) Disposable Electrodes, and, (b) None disposable Electrodes [5].

2. Treatment Process

The process of removing a stone from the kidney or from the ureter without the need for an open surgical technique is known as lithotripsy, which is a non-invasive surgical technique. The technique involves disintegration of the stone in vivo, so that it can pass through the urinary tract in the form of small particles, the passage of which doesn't result in sever discomfort or disability. The treatment process can be planned ahead depending on patient weight, sex, and type of stone [2, 3]. This planning

* Corresponding author. jian@hu.edu.jo

will indicate more accurately the times when the automatic adjustment should take place [4].

In percutaneous lithotripsy, a probe is guided under X-ray fluoroscopy through a small incision into the location of the kidney stone. Mechanical shock waves are produced at the tips of the probe by a controlled electric-discharge (spark), or the probe contains an ultrasonic transducer that produces ultrasonic waves. Each of these forms of energy is used to break up the kidney stone, so that it can be withdrawn in pieces through the probe guide element or can be allowed to pass through the urinary tract.

Extracorporeal shock wave lithotripsy generates high-pressure waves outside the body which can be focused at a specific site within the body called the Focal Point (F_2). This focal point is important and is needed throughout the treatment process in order to concentrate and direct the shock wave energy on the stone, so that a maximum fragmentation can occur to the stone with minimum pain and discomfort to the patient [6]. The variation of the size of the focal point results in variation to the energy density [7], and hence the total energy being delivered to the desired treatment area, as shown in Figure 2a and 2b.

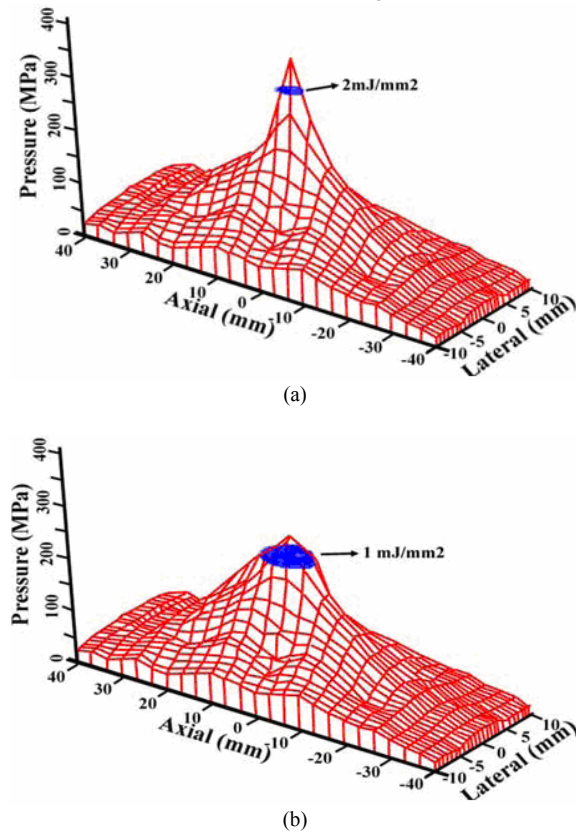


Figure 2. (a) High energy density for a fine focal. [7], (b) Same total energy distributed over a larger focal point. [7]

Many mechanical shock waves are produced at one focus of an ellipsoidal reflector such that these waves converge to another focal point several centimetres away from the reflector. The reflector and the patient are submerged in demineralised, degassed water in such a way enabling the patient to move until the stone is located at the focal point of the shock wave. This positioning of the patient is critical, and a biplane X-ray system is used to establish the position of the stone at the focal point as well as to monitor its disintegration.

A high-voltage pulse (approximately 20 kV) is applied to the spark gap, and the discharge produces a shock wave that propagates through the water to the focal point. The patient is placed on a gantry support that can be precisely positioned as the operator observes the stone on the biplane X-ray monitors. Once the patient is approximately positioned, multiple-shock waves are generated by multiple discharges across the spark gap. Up to 2000 shock waves may be necessary to reduce kidney stone down to one to two millimetre fragments that can pass through the urinary tract. With this treatment, most patients are able to resume full activity after two days. This considerably reduce the needed time than surgical treatment by lithotomy would entail. Although the apparatus is complex and expensive to purchase and operate, the overall savings for the patient and the health-delivery system are clear [1, 8].

2.1. Energy and Number of Shocks

Depending on many factors, doctors can determine the appropriate energy of each shock (kV) and the corresponding number of shocks, which can be used as the input to the lithotripsy instrument. From 2^k factorial design, the most significant factors on ESWL outcome are related to the stone and to the patient. Doctors depend on these factors to determine the appropriate energy of each shock (kV) and the corresponding number of shocks. These factors are:

- Factors related to the patient such as age and condition of patient.
- Factors related to the stone such as, diameter, composition, location, and number of stones.

The stones may have different shapes and different diameters. Figure 3 illustrates some of the stones found in human bodies. Generally, stones with diameter below 2cm can be successfully treated with ESWL. On the other hand, specialists recommend that stones with greater diameter should not be treated with the ESWL. A stone located in the kidney is known as renal calculi while the stone located in the ureter is known as ureteric calculi.

2.2. Collecting Data and Analysis

Several data were collected from various clinical centres taking in mind the factors mentioned earlier [9, 10, and 11]. Tables 1, 2, and 3 illustrate these data. It is obvious that the location of the stone, its size, and age effect the treatment process in terms of number of shocks and the energy given in (kilo Volt; kV). Design Ease software package [12] and statistical analysis [13, 14, 15, and 16] have been used where factors such as patient age, stone location, and stone diameter are considered as input variables while the number of shocks is considered as the output.

The results with all factors and coefficients are illustrated in Table 4-a and Table 4-b:

From these tables, a relationship can be derived between the patient age (A), stone position (B), stone diameter (C), and the number of shocks (N) given to the patient as illustrated in Equation 1 below:

$$N = 2350 + 225 * A + 725 * B + 1075 * C + 100 * A * B + 100 * A * C + 350 * B * C + 75 * A * B * C \quad (1)$$

It can be noted that:

1. Sum source squares values are as follows $C > B$ and $B > B * C$ and $B * C > A$
2. Coefficients values are as follows $C > B$ and $B > B * C$ and $B * C > A$
3. The most significant factors affecting ESWL outcomes are: stone diameter, stone position (or location), and position-diameter (location-diameter), and patient age. So we choose these factors for the next step of analysis. This is shown in Figure 3 and Figure 4.

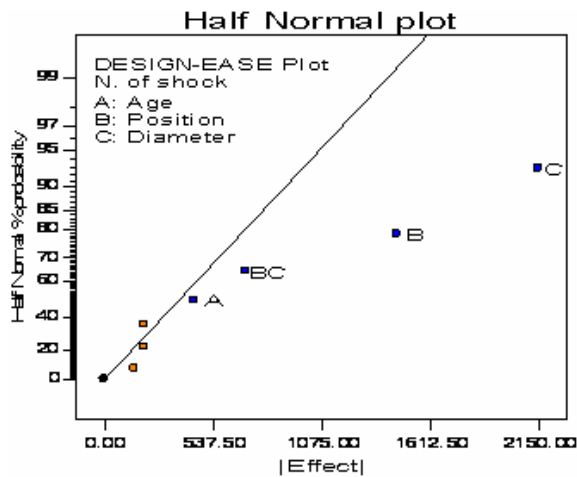


Figure 3. Half normal plot.

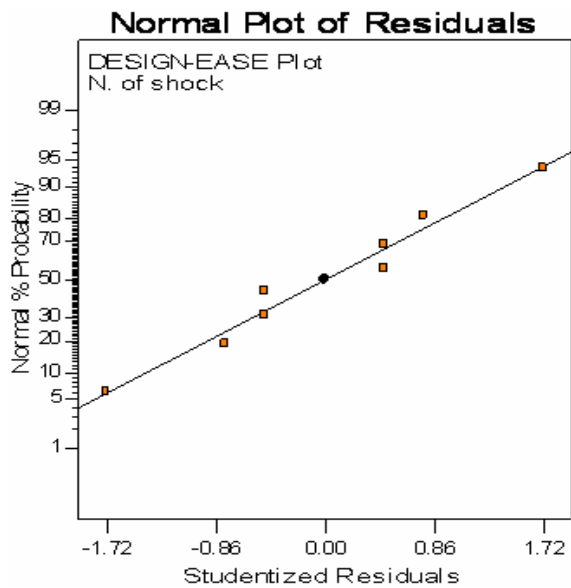


Figure 4. Normal plot of residuals.

Now we will conduct analysis of variance the selected factorial design.

Through close inspection of Table 5-a, Table 5-b and Table 5c, it could be noticed that:

- I. The Model F-value of 54.27 implies that the model is significant, and there is only a 0.39% chance that a "Model F-Value" this large could occur due to noise.
- II. Values of "Prob > F" less than 0.0500 indicate model terms are significant, in this case B, C, BC, and A are significant model terms, values greater than 0.1000 indicate the model terms are not significant.
- III. The 'pred R-squared' of 0.9031 is in reasonable agreement with the 'Adj R squared' of 0.9682.

IV. Adeq precision' measures the signal to noise ratio. A ratio greater than 4 is desirable, and the ratio of our design is 19.597 indicating an adequate signal.

This leads to the Equation 2 of the number of shocks (N) in terms of Coded Factors:

$$\text{Number of Shocks} = 2350 + 225 * A + 725 * B + 1075 * C + 350 * B * C \quad (2)$$

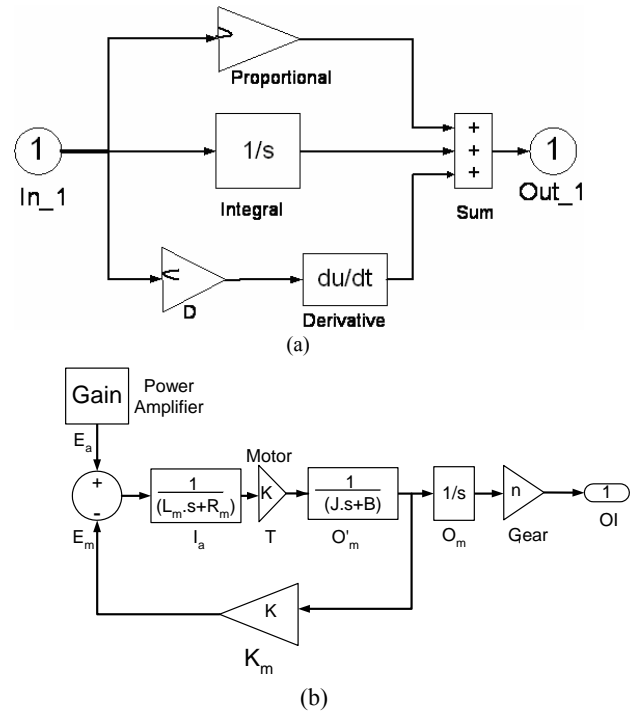


Figure 5. (a) Block diagram of PID controller, (b) Block diagram of plant (power amplifier, stepper motor, and gear).

Table 1. Data regarding patient age, location and number of shocks [9]

Patient Age (Years)	Stone Location	Stone Diameter (mm)	Response I Run No. of Shocks per Session	No. of Sessions
18	Kidney	2	800	1
90	Kidney	2	1000	1
18	Ureter	2	1500	1
90	Ureter	2	1800	1
18	Kidney	20	2200	2
90	Kidney	20	2500	2
18	Ureter	20	4000	2
90	Ureter	20	5000	2

The following conclusions can be derived from the previous equations and analysis:

1. The numerical estimates of the effect indicate that the effect of stone diameter (C) is large and has a positive direction (increasing C increases number of shock), since

changing stone diameter from low (2 mm) to high (20 mm) changes the number of shocks by 1075 shocks.

Table 2. Data regarding patient age, location and number of shocks [10]

Patient Age (Years)	Stone Location	Stone Diameter (mm)	Response1 Run No. of Shocks per Session	No. of Sessions
30	Kidney	5	1200-1500	1
30	Ureter	5	2000-2200	1
30	Kidney	10	1800-2000	1
30	Ureter	10	2000-2500	1
30	Kidney	15	≈ 2200	2
30	Ureter	15	≈ 4000	2
30	Kidney	20	≈ 2200	2
30	Ureter	20	≈ 5000	2

- The numerical estimates of the effect indicate that the effect of stone position (B) is large and has a positive direction (increasing B increases number of shock), since changing stone position from low (kidney) to high (ureter) changes the number of shocks by 725 shocks.
- The numerical estimates of the effect indicate that the effect of position-diameter (B*C) is large and has a positive direction (increasing B*C increases number of shock), since changing stone position-diameter from low (kidney-2mm) to high (ureter-20mm) changes the number of shocks by 350 shocks.
- The numerical estimates of the effect indicate that the effect of patient age (A) is large and has a positive direction (increasing A increases number of shock), since changing patient age from low (18 years) to high (90 years) changes the number of shocks by 225 shocks.
- The most significant factors are stone diameter and its location while the patient age has less effect on the number of shocks given to the patient.
- This result agrees with the practical specimens collected from various medical centres as shown earlier.

The best method used to study the factors that vary together is the factorial design method, where the most important benefits from the process are that any operator can treat the patient without the need for high experience to determine number of shocks and energy of each case.

3. Model Construction

From 2^k factorial design the most significant factors affecting ESWL outcome are patient age, stone position, age-and-position interaction, and stone size. In LABVIEW software, the patient age and the stone size are selected

Table 3. Data information regarding patient age, location and number of shocks [11]

Patient Age (Years)	Stone Location	Stone Diameter (mm)	Response1 Run No. of Shocks per Session	No. of Sessions	kV
10	Kidney	5	2000	1	12
10	Ureter	5	2000	1	12
10	Kidney	10	2000	1	12
10	Ureter	10	2000	1	12
10	Kidney	15	2000	2	12
10	Ureter	15	2000	2	12
10	Kidney	20	2000	2-3	12
10	Ureter	20	2000	2-3	12
10	Kidney	25	2000	3-4	12
10	Ureter	25	2000	3-4	12
10	Kidney	30	2000	> 5	12
10	Ureter	30	2000	> 5	12
20	Kidney	5	4000	1	18
20	Ureter	5	6000	1	18-20
20	Kidney	10	4000	1	18
20	Ureter	10	6000	1	18-20
20	Kidney	15	4000	2	18
20	Ureter	15	6000	2	18-20
20	Kidney	20	4000	2	18
20	Ureter	20	6000	2	18-20
20	Kidney	25	4000	3	18
20	Ureter	25	6000	3	18-20
20	Kidney	30	4000	> 5	18
20	Ureter	30	4000	> 5	18-20

Table 4a. Analysis of variance for all factors.

Model	Sum of Source Squares	DF	Mean Square
	1.504E+7	7	2.149E+6
A	4.050E+5	1	4.050E+5
B	4.050E+6	1	4.205E+6
C	9.245E+6	1	9.245E+6
A*B	80000.00	1	80000.0
A*C	80000.00	1	80000.0
B*C	9.800E+5	1	9.800E+5
A*B*	45000.00	1	45000.0
C			

Table 4b. Factor estimates and their coefficient.

Factor Estimate	Coefficient
Intercept	2350.00
A - Age	225.00
B - Position	725.00
C - Diameter	1075.00
A*B	100.00
A*C	100.00
B*C	350.00
A*B*C	75.00

Table 5a. Analysis of variance for selected factorial design

Model	Sum of Squares	DF	Mean Square	F Value	Prob > F
Intercept	1.484E+007	4	3.709E+006	54.27	0.0039
A	4.050E+005	1	4.050E+005	5.93	0.0930
B	4.205E+006	1	4.205E+006	61.54	0.0043
C	9.245E+006	1	9.245E+006	135.29	0.0014
BC	9.800E+005	1	9.800E+005	14.34	0.0323

Table 5b. data analysis.

Std. Dev	261.41
Mean	2350.00
R-Squared	0.9864
Adj R-Squared	0.9682
Pred R-Squared	0.9031
Adeq Precision	19.597

Table 5c. Standard error of data

Coefficient Factor	Estimate	DF	Standard Error	95% CI Low	95% CI High	VIF
Intercept	02350.0	1	92.42	2055.87	2644.13	1.00
A-Age	225.00	1	92.42	-69.13	519.13	1.00
B-Position	725.00	1	92.42	430.87	1019.13	1.00
C-Diameter	1075.00	1	92.42	780.87	1369.13	1.00
BC	350.00	1	92.42	55.87	644.13	1.00

To be the inputs while the number of shocks is the output. The Model was obtained using Mathcad as follows:

MAD=	18	2	VN=	600
	26	4		1000
	34	6		1400
	42	8		2000
	50	10		2200
	58	12		2200
	64	14		2500
	72	16		3500
	80	18		4000
	90	20		4000
K=1		Span =0.75		
The answer of the regress are the coefficients:				
3				
3				
Regress(MAD,Vn, K)=	1	K		
	-13.41	a ₁		
	-315.513	a ₂		
	-546.667	a ₀		
The equation:				
Number of Shocks = N = 546.667-31041*A+315.513*D				
Where, A is the patient age, D is the stone diameter				

4. Proportional Integral Derivative (PID) Controller

The distance between the two electrodes has to be automatically adjusted using a closed loop control system. This process will keep the focal point F_2 in the optimal position to minimize the pain and discomfort to the patient. An automatic control model of distance between the electrodes is simulated, using MATLAB, and SIMULINK was used to visualize the performance of the controller; the design is simulated as a closed loop control system containing controller, plant, and sensor unit.

The PID controller combines the proportional (P), the integral (I), and the differential component (D) as Figure 5a and Figure 5b show. The manipulated value y is given by Equation 2 and further simplified into Equation 3 [17, 18, and 19]:

$$y = K_p \cdot x_d + \frac{1}{T_i} \int x_d \cdot dt + K_d \cdot \frac{d x_d}{dt} \quad (3)$$

$$y = K_p \left(x_d + \frac{1}{T_r} \int x_d \cdot dt + T_d \cdot \frac{d x_d}{dt} \right) \quad (4)$$

Where

y = Controller output

K_p = Proportional gain.

T_i = Integral time.

K_d = Derivative action coefficient.

$T_r = K_p T_i$ Reset time which is the period by which the PI controller is faster than the I Controller.

$T_d = K_d/K_p$ the time needed to get the wanted manipulated variables using D component earlier than when using the PI controller.

Stepper motors are low-cost solution for position control and inherently high torque/position gain resulting in excellent holding torque. The electrical torque acts to increase rotational speed (ω), while the mechanical torque acts to slow it. The net accelerating torque in the machine:

Torque=moment of inertia \times acceleration

$$T_{net} = J \times \alpha \quad (5)$$

$$T_{net} = J \times \left(\frac{d\omega}{dt} \right) \quad (6)$$

$$T_{net} = J \times \left(\frac{d^2(\theta)}{dt^2} \right) \quad (7)$$

Where:

T_{net} : net accelerating torque in machine(N.m.s)

J : moment of inertia for the machine(N.m.s²).

α : rotational acceleration (rad/sec²).

θ : phase angle of a rotating machine(rad) .

Assuming a constant field current and a constant flux Φ ,

$$e_m(t) = K \cdot \Phi \cdot \frac{d(\theta)}{dt} = K_m \cdot \frac{d(\theta)}{dt} \quad (8)$$

where:

$e_m(t)$ is the back electromotive force (V).

K is the motor parameter

K_m is a function of the permeability of magnetic material.

Then, by Laplace transform;

$$\frac{E_m(s)}{\theta(s)} = K_m(s) \quad (9)$$

The armature current is related to the input voltage applied to the armature as

$$E_a(s) = (R_m + L_m \cdot s) \cdot I_a(s) + E_m(s) \quad (10)$$

$$G_1(s) = \frac{I_a(s)}{\{ E_a(s) - E_m(s) \}} = \frac{1}{(R_m + L_m \cdot s)} \quad (11)$$

Where:

I_a is the motor armature current

E_a is the motor input voltage

The armature current would be:

$$I_a(s) = \frac{E_a(s) - E_m(s)}{R_m + L_m \cdot s} \quad (12)$$

The torque developed by the motor is assumed to be related linearly to θ and to the armature current as follows

$$T(t) = K_t \cdot \theta \cdot \dot{I}_a(t) = K_\tau \cdot \dot{I}_a(t) \quad (13)$$

By Laplace transform:

$$T(s) = K_\tau I_a(s). \quad (14)$$

The load torque for motor

$$J \frac{d^2\theta}{dt^2} = T(t) - B \frac{d\theta}{dt} \quad (15)$$

Where,

B is the air friction and bearings friction (Damping coefficient) .

$$T(t) = J \frac{d^2\theta}{dt^2} + B \frac{d\theta}{dt} \quad (16)$$

Laplace transformation yields:

$$T(s) = \{ J \cdot s^2 + B(s) \} \cdot \theta(s) \quad (17)$$

$$G_2(s) = \frac{\theta(s)}{T(s)} = \frac{1}{J \cdot s^2 + B(s)} \quad (18)$$

$$\theta(s) = \frac{T(s)}{J \cdot s^2 + B(s)} \quad (19)$$

Where θ is the angle of Rotation:

We can get the motor transfer function:

$$G(s) = \frac{\theta(s)}{E_a(s)} \quad (20)$$

$$G(s) = \frac{K_\tau \cdot G_1(s) \cdot G_2(s)}{1 + K_\tau \cdot G_1(s) \cdot G_2(s) \cdot H(s)} \quad (21)$$

$$G(s) = \frac{K_\tau}{J \cdot L_m \cdot s^3 + (B \cdot L_m + J \cdot R_m) \cdot s^2 + (R_m + K_\tau K_m) \cdot s} \quad (22)$$

But L_m is small enough so it can be ignored;

$$G(s) = \frac{K_\tau}{J \cdot R_m \cdot s^2 + (R_m + K_\tau \cdot K_m) \cdot s} \quad (23)$$

In order to move the two electrodes simultaneously, each with half the required distance, using only one stepper, we need to redesign the whole electrode set which will complicate the design and will deprive the current instruments from utilising the benefit of automatic control. We decided to use two separate stepper motors; one for each electrode, and thus the movement expected of each stepper will be half the required distance. The plastic covering of the mechanism is removed, and each stepper is

coupled to the corresponding electrode mechanism through a screw and gear whose transfer ratio (coupling ratio) enables very fine adjustment. This modification can be suggested to the industry to modify the design of the electrodes set to allow for both manual and automatic adjustments.

5. Results and Discussion

The resulting model for computing the number of shocks as a function of patient age (A) and stone diameter (D) is given as:

$$\text{Number of Shocks} = N = 546.667 - 31041 \cdot A + 315.513 \cdot D \tag{24}$$

Now, to obtain the equation that relates the distance to the number of shocks, we gathered data experimentally from Arabic Centre of Lithotripsy (Al-Khalidi Hospital) by measuring the distance between the two electrodes after number of shocks at certain kV. Sources of error include personal, measuring, and random. The following tables and figures show the *Number of Shocks* vs. *Distance* for different values of kV.

Table 6a. Data of electrodes distance and Number of shocks at 16 kV.

Distance (mm)	No. of shocks
0.0	0
0.41	200
0.5	450
0.58	700
0.65	1000
0.69	1500
0.89	2000
0.95	2500
0.97	3000

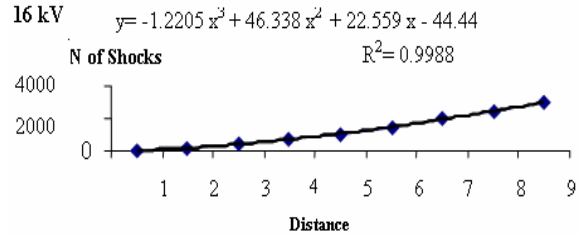
Table 6b. Data of electrodes distance and Number of shocks at 18 kV.

Distance (mm)	No. of shocks
0.0	0
0.05	250
0.17	500
0.49	1000
0.77	1500
0.97	2000
1.17	2500
1.27	3000

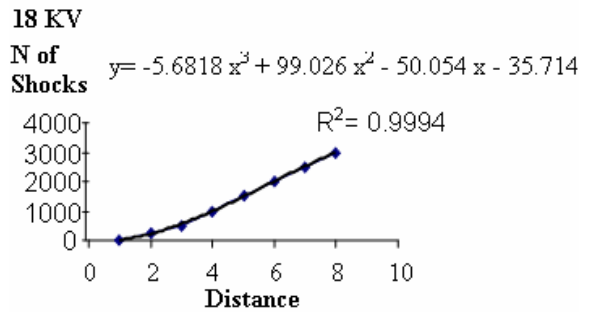
The same behaviour is observed from Figure 6 at different voltage values (kV). Depending on this trend, a fitting curve is obtained for different high voltage values and shown in Figure 7.

Table 6c. Data of electrodes distance and Number of shocks at 20 kV.

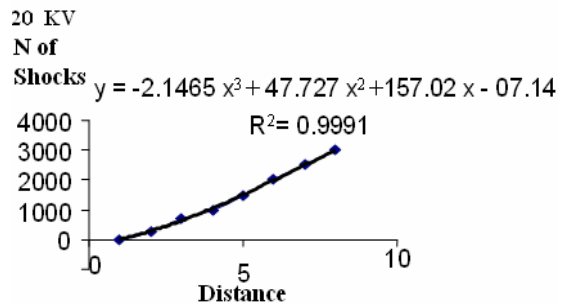
Distance (mm)	No. of shocks (shocks)
0.0	0
0.32	250
0.47	700
0.57	1000
0.79	1500
1.17	2000
1.52	2500
1.88	3000



(a)



(b)



(c)

Figure 6. (a) Shows the relationship between the distance and number of shocks for 16 kV, (b) Shows the relationship between the distance and number of shocks for 18 k, (c) Shows the relationship between the distance and number of shocks for 20 kV

The second half of the model, used in automatic control, presents the relation between number of shocks and distance between electrodes:

$$\text{Distance} = 3 \cdot 10^{-11} \cdot X^3 - 2 \cdot 10^{-7} \cdot X^2 + 0.0007 \cdot X + 0.0529 \tag{25}$$

Where *X* is the number of shocks.

Any operator can safely use the software interface of the mathematical model as Equation 24 shows, where patient age and stone size are provided to calculate the suitable number of shocks which is, then, used to find the corresponding distance (ΔD) from Equation 25. The PID controller compares this distance with the safe distance

($\Delta D \geq \Delta D_{\text{safe}}$) so that when exceeded, it forces the electrodes to return to the reference distance.

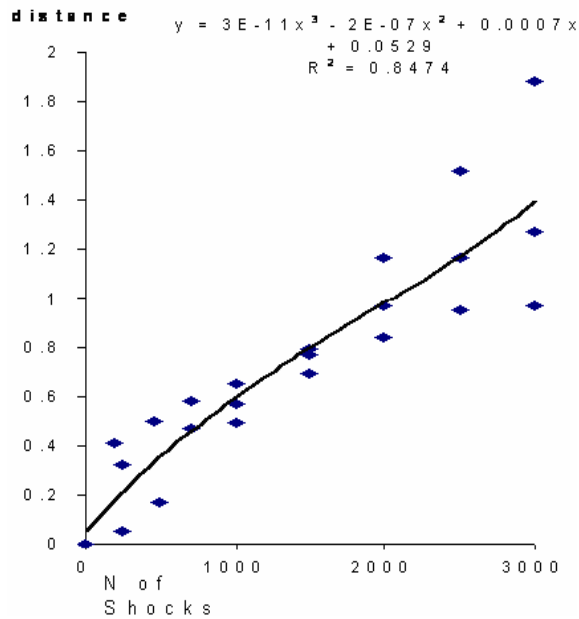


Figure 7. Shows fitting curve relationship between the distance and number of shocks for various kilo Volts.

6. Conclusion

This paper shows that this process has derived a mathematical model that is integrated into a software interface, which allows any operator to treat the patient without the need of highly experienced professionals to determine number of shocks for each case on one hand. On the other hand, and as a consequence, this process will automatically and accurately keep the focal point F_2 in the optimal position which minimizes patient pain and discomfort and saves precious time wasted on calibration conducted by professionals.

The system has been on trials in a number of hospitals and has shown good results. Predictions have, always, been confirmed by professionals and no confliction was reported. The model and control system could be integrated into an expert system, which will enhance performance with time.

References

- [1] Clark J W. Medical Instrumentation: Application and Design, 3rd ed. Wiley; 1998
- [2] H. M. Amasha, B. M. Al-Eideh, "Statistical case study of extracorporeal shock wave lithotripsy". Engineering in Medicine and Biology Society. Proceedings of the 23rd Annual International Conference of the IEEE, Vol. 4, Istanbul, Turkey, Oct. 2001, 3935-3937.
- [3] J. S. Shieh, T. C. Yang, C. C. Liu, "An Enhanced Patient Controlled Analgesia (EPCA) for the ESWL". Biomedical Engineering: Application, Basis and Communication, Vol. 19, No. 1, 2007, 7-17.
- [4] J. M. Gilmore, P. A. Lewin, M. E. Schafer, "Sensors for characterization of extracorporeal shock wave devices". Engineering in Medicine and Biology Society, Proceedings of the Annual International Conference of the IEEE, Vol. 2, Philadelphia, USA, 1988, 751 - 752.
- [5] Retrieved from: <http://www.pckmed.com/>.
- [6] M. Robert, B. Segui, C. Vergnes, P. Taourel, J. Guiter, "Piezoelectric extracorporeal shockwave lithotripsy of distal ureteric calculi: assessment of shockwave focusing with un-enhanced spiral computed tomography". BJU International, Vol. 87, 2001, 316-321.
- [7] Retrieved from <http://www.hofterleeuwe.com/>.
- [8] H. Reichenberger, "Lithotripter systems". Proceedings of the IEEE, Vol.76, Issue 9, Sep. 1988, 1236 1246.
- [9] Retrieved from <http://www.kidney.org/general/oatoz/content/lithotripsy.html>.
- [10] Retrieved from <http://www.endeicione.com/med/topic3024.html>.
- [11] Retrieved from <http://www.glacit.caltech.edu/>.
- [12] Retrieved from <http://www.nwasoft.com/>.
- [13] Montgomery D C, Goldsman D M. Applied statistics and probability for engineers. Wiley; 2006.
- [14] Montgomery D C, Runger G C. Engineering statistics. Wiley; 2007.
- [15] Soong T. Fundamentals of probability and statistics for engineers. Wiley; 2004.
- [16] Devore J L. Probability and statistics for engineering and the sciences. Enhanced Review. 7th ed. Duxbury Press; 2008.
- [17] Dorf R, Bishop R. Modern control system. 11th ed. Prentice Hall; 2007.
- [18] Golnaraghi K B. Automatic control systems. 8th ed. Wiley; 2002.
- [19] Nise N S. Control systems engineering. 5th ed. Wiley; 2007.

Comparison of Diesel Engine Performance and Emissions from Neat and Transesterified Cotton Seed Oil

A. Siva Kuma^{a,*}, D. Maheswar^b, K. Vijaya Kumar Reddy^c

^aDepartment of Mechanical Engineering, Malla Reddy Engineering College, Secundrabad - 14, Andhra Pradesh, India.

^bTurbo Machinery Institute of Technology, Pantancheru, Medak (Dist.), Andhra Pradesh, India.

^cDept. of Mechanical Engineering, JNTU College of Engineering, JNTU Hyderabad, Andhra Pradesh - 85, India.

Abstract

There is an increasing interest in India to search for suitable alternative fuels that are environmental friendly. Environmental concerns and limited amount of petroleum resources have caused interests in the development of alternative fuels for internal combustion (IC) Engines. As an alternative, biodegradable, renewable and sulphur free biodiesel is receiving increasing attention. The use of biodiesel is rapidly expanding around the world, making it imperative to fully understand the impacts of biodiesel on the diesel engine combustion process and pollutant formation. Biodiesel is known as the mono-alkyl-esters of long chain fatty acids derived from renewable feedstock, such as, vegetable oils or animal's fats, for use in compression ignition engines. Therefore, in this study, different parameters for the optimization of biodiesel production were investigated in the first phase, while in the next phase of the study performance test of a diesel engine with neat diesel fuel and biodiesel mixtures was carried out. Biodiesel was made by the well known transesterification process. Cottonseed oil (CSO) was selected for biodiesel production. The transesterification results showed that with the variation of catalyst, methanol, variation of biodiesel production was realized. However, the optimum conditions for biodiesel production are suggested in this paper. A maximum of 76% biodiesel was produced with 20% methanol in presence of 0.5% sodium methoxide. The engine experimental results showed that exhaust emissions including carbon monoxide (CO), particulate matter (PM) and smoke emissions were reduced for all biodiesel mixtures. However, a slight increase in oxides of nitrogen (NO_x) emission was experienced for biodiesel mixtures.

© 2009 Jordan Journal of Mechanical and Industrial Engineering. All rights reserved

Keywords: Bio-Diesel; Transesterification; Cottonseed Oil Methyl Ester; Performance and Exhaust Emissions.

1. Introduction

New and renewable alternative fuels as a substitute for petroleum-based fuels have become increasingly important due to environmental concerns, unstable costs and transportation problems. One of the renewable alternative fuels is bio-diesel, which is domestically produced from new or used vegetable oil and animal fat. Oil or fat reacts with alcohol (methanol or ethanol). This reaction is called transesterification. The reaction requires heat and a strong catalyst (alkalis, acids, or enzymes) to achieve complete conversion of the vegetable oil into the separated esters and glycerin [9]. During the transesterification reaction, glycerin is obtained as a by-product. It is used in pharmaceutical, cosmetic and other industries [1, 2]. Not only can bio-diesel be used alone in neat form but it can

also be mixed with petroleum diesel fuel in any unmodified diesel engine [3].

Diesel fuel is very important for countries economy because it has a wide area of usage such as long haul truck transportation, railroad, agricultural and construction equipment. Diesel fuel contains different hydrocarbons, sulphur and contamination of crude oil residues [4, 5]. But chemical composition of biodiesel is different from the petroleum-based diesel fuel. Biodiesel hydrocarbon chains are generally 16-20 carbons in length and contain oxygen at one end. Bio-diesel contains about 10% oxygen by weight. Bio-diesel does not contain any sulfur, aromatic hydrocarbons, metals and crude oil residues [10, 6]. These properties improve combustion efficiency and emission profile. Biodiesel fuel blends reduce particulate matter (PM), hydrocarbon, carbon monoxide and sulfur oxides [11]. However, NO_x emissions are slightly increased depending on biodiesel concentration in the fuel [12, 13]. Due to the lack of sulfur biodiesel decrease, levels of corrosive sulfuric acid accumulate in engine crank case oil

* Corresponding author. siva_appisetty1@yahoo.co.in

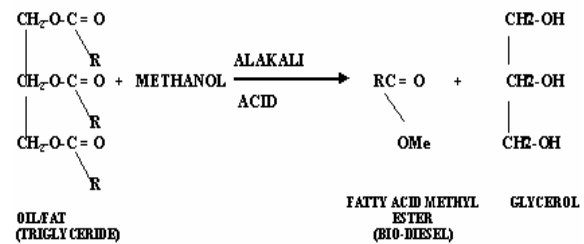
[7]. Using biodiesel is a big advantage for countries where petroleum is imported [14]. Many countries that import crude petrol encourage the production of bio-diesel by reducing taxes and by giving low interest credits.

Vegetable oils, the main source of biodiesel, have considerably higher viscosity and density compared to diesel fuel. Despite transesterification process, which has a decreasing effect on the viscosity of vegetable oil, it is known that bio-diesel still has some higher viscosity and density when compared with diesel fuel [15, 16]. The viscosities of fuels have important effects on fuel droplet formation, atomization, vaporization and fuel-air mixing process, thus influencing the exhaust emissions and performance parameters of the engine. There have been some investigations on using preheated raw vegetable oils such as palm and jatropha oil in diesel engines [8,17]. However, it is known that vegetable oils have considerably higher viscosity compared with diesel fuel. It was declared that CO, HC and particulate matter emission were improved because preheating reduced the viscosity of raw vegetable oil to almost the level of diesel fuel and caused a better combustion [18].

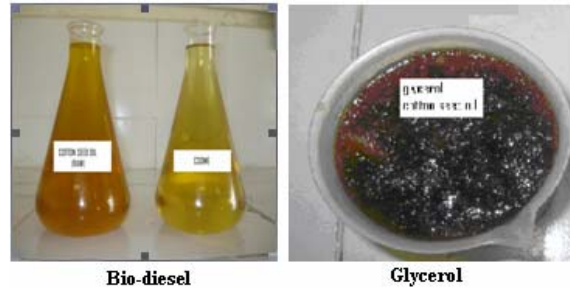
In the present investigation different parameters for biodiesel production have been investigated and the effects of viscosity of cottonseed oil methyl ester (CSOME), which is decreased by means of preheating process, on the performance parameters and exhaust emissions of a diesel engine. For this aim, CSOME was produced by transesterification method, using cottonseed oil and methyl alcohol, and its effect of reaction temperature, catalyst percentages, alcohol percentages and reaction time for optimum biodiesel production have been studied, and its properties were determined. Finally, the results for CSOME were compared with those for diesel fuel.

2. Production of Cottonseed oil Methyl Ester

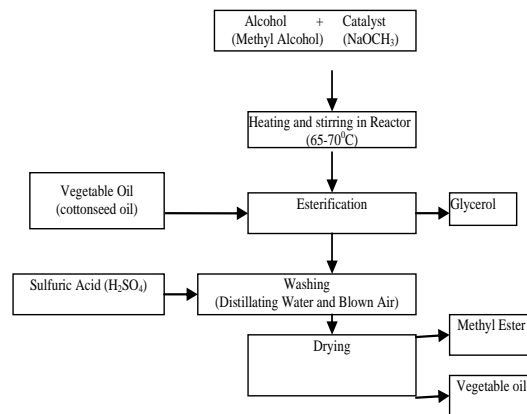
The Transesterification process of cottonseed oil was performed using 5g Sodium methoxide as catalyst and 100ml methyl alcohol per 1 litre pure cotton seed oil. First, the cottonseed oil was heated to about 65-70°C in a reactor with a capacity of about 40 litres. Then, the catalyst was mixed with methyl alcohol to dissolve and added to the heated cotton seed oil in the reactor. After the mixture was stirred for 1 h at a fixed temperature of about 70°C, it was transferred to another container and the separation of the glycerol layer was allowed. Once the glycerol layer was settled down, the methyl ester layer, formed at the upper part of the container, was transferred to another vessel. After that, a washing process to remove some unreacted remainder of methanol and catalyst was carried out, using distilled water and blown air. Then, a distillation process at about 110°C was applied for removing the water contained in the esterified cottonseed oil. Finally, the produced cottonseed oil methyl ester (CSOME) was left to cool down. The Chemical Equation of Transesterification Process, Crude, Transesterified (Biodiesel) of Cottonseed Oil and its by-product, and the Production Process of CSOME are presented in Figure 1a, Figure 1b and Figure 1c respectively.



(a)



(b)



(c)

Figure 1. (a) Chemical Equation of Transesterification Process, (b) Crude, Transesterified (Biodiesel) Cotton Seed Oil and its by-product, (c) The flowchart of the cotton seed oil methyl ester (CSOME) production processes

3. Experimental Setup

A single cylinder 4-stroke water cooled diesel engine developing 5.2 KW at 1500 rpm was used. Engine details are given in Table 1. The schematic of the experimental setup is shown in Figure 2. An eddy current dynamometer was used for loading the engine. The fuel flow rate was measured on the volumetric basis. Experiments were initially carried out on the engine at all loads using diesel to provide base line data. The engine was stabilized before taking all measurements. Various blends of different proportions of CSOME and diesel were used to run a single cylinder CI engine.

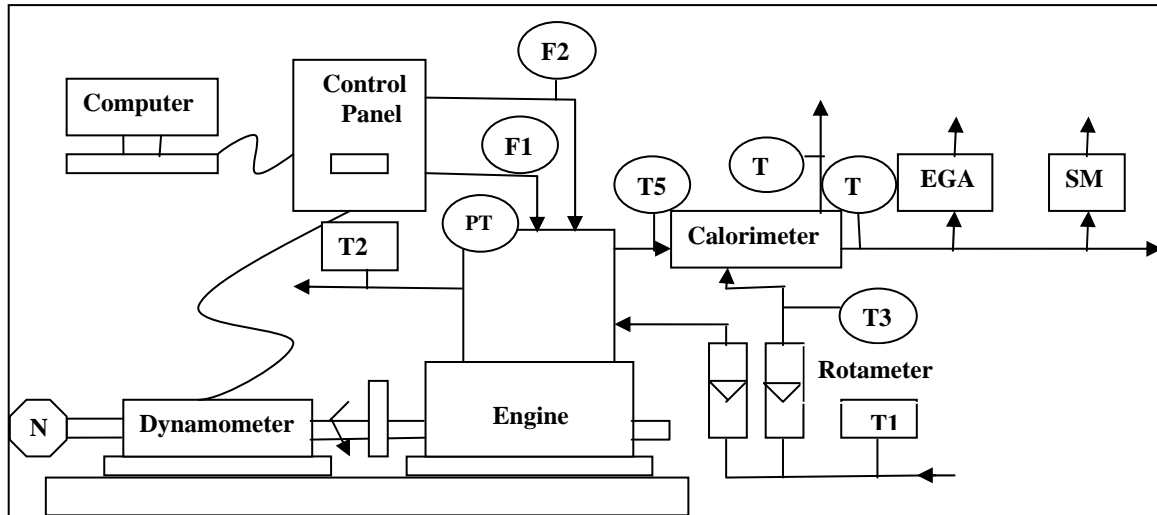


Figure 2. Experimental Setup with main parts

Where,

- | | | | |
|--------|---|-----|------------------------------|
| T1, T3 | Inlet Water Temperature °C | F2 | Air Intake DP unit |
| T2 | Outlet Engine Jacket Water Temperature °C | PT | Pressure Transducer |
| T4 | Outlet Calorimeter Water Temperature °C | Wt | Load kg |
| T5 | Exhaust Gas Temperature before Calorimeter °C | N | RPM Decoder |
| T6 | Exhaust Gas Temperature after Calorimeter °C | EGA | Exhaust Gas Analyzer (5 gas) |
| F1 | Fuel Flow DP (Differential Pressure) unit | SM | Smoke meter |

4. Results and Discussions

4.1. Optimization of Different Parameters for Biodiesel Production

The rate of conversion from CSO to CSOME depends upon the different parameters like oil temperature, reaction temperature, catalyst percentage, methanol percentage, purity of reactants, etc. In this work, reaction temperature, catalyst percentage and methanol percentage have been investigated.

4.1.1. Reaction Temperature and Biodiesel Production

Figure 3. shows the effect of methanol percentages on biodiesel production. The volumetric percentages of methanol were varied from 15% to 25%. The weight percentage of catalyst (NaOCH₃) was fixed at 0.5%. The reaction temperature was varied from 45 to 60°C. The maximum bio-diesel yield was noticed at 20% methanol. This was due to the fact that the 20% methanol has a favorable influence on maximum bio-diesel production. A maximum of 76% biodiesel production was observed at 20% methanol and at a temperature of 55°C.

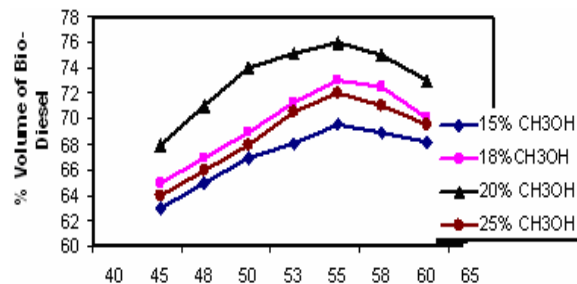


Figure 3. Effect of Temperature on Bio-Diesel Production (NaOCH₃=0.5%)

Table 1. Experimental Setup Specifications.

Engine	Four-stroke, single cylinder, constant speed, water cooled Diesel engine
Maximum Power/ HP	5.2 KW @ 1500 RPM/ 7.2 HP
Bore x Stroke	87.5 x 110 mm
Compression Ratio	17.5:1
Dynamometer	Eddy current dynamometer with loading unit

4.1.2. Influence of Catalyst Percentage and Biodiesel Production

Figure 4. Depicts the influence of catalyst percentages on bio-diesel production. The weight percentages of catalyst were varied from 0.5 to 0.75%. The optimum methanol percentage was kept

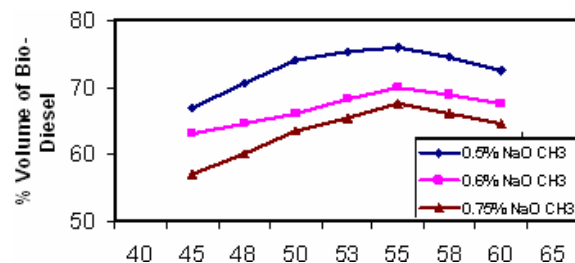


Figure 4. Effect of Catalyst (NaOCH₃) Percentages on Bio-Diesel (CH₃OH=20%).

constant to 20%. It can be seen from the figure that with the increase in lye catalyst, bio-diesel yield decreases. This may be associated with the increase in the formation of wax. The vegetable oil used in transesterification process contains many free fatty acids. The catalyst reacts with these free fatty acids and

produces wax. A maximum of 76% bio-diesel yield was found at 0.5wt%. Catalyst and at a reaction temperature of 55°C. If the weight percentage of catalyst is used below 0.5% the bio-diesel production was found minimum. Thus 20% methanol and 0.5% NaOCH₃ were chosen as the optimum percentages for biodiesel production.

4.1.3. Influence of Reaction Time on Biodiesel Production

Figure 5 shows the effect of reaction time on bio-diesel production. The catalyst percentage was set to 0.5. The reaction temperature was kept at 55°C. It was found that when reaction time increases, the bio-diesel production increases and reaches maximum at about 8hrs. Then bio-diesel production decreases with the increase in reaction time. When the mixture of CSO, methanol and catalyst was kept for 24hrs, the bio-diesel production was reduced to 70%. This was due to the fact that the tendency of soap formation increases with the increase in reaction time. It was found that for 8hrs the maximum bio-diesel production was 76.5%.

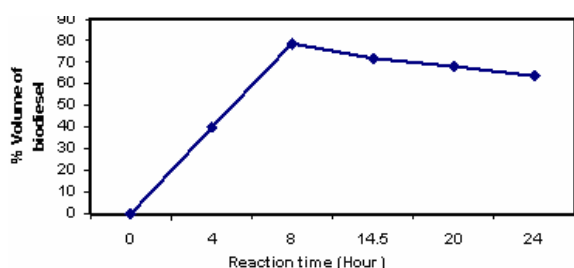


Figure 5. Effect of Reaction Time on Bio-Diesel Production (CH₃OH=20%NaOCH₃=0.5%, Reaction Temperature 60°C).

4.2. Properties of Neat Diesel Fuel and Biodiesel Mixtures.

Performance of CI engine greatly depends upon the properties of fuel, among which viscosity, density, cetane number, volatility, lubricity, calorific value, etc are very important. In this work the effect of temperature on viscosity with neat diesel fuel and different biodiesel mixtures have been investigated.

Viscosity and other properties of neat diesel fuel and CSOME were determined by the authors and shown in Table 2. Regarding volatility, there are no direct volatility data for bio-diesel, but it can be explained with the help of distillation temperature. Since diesel fuel (90% = 326°C, table 2) has lower distillation temperature than that of biodiesel (90% = 361°C, table 2), neat biodiesel has low volatility.

4.2.1. Viscosity as a Function of Temperature

One of the major interests of this work is bio-diesel viscosity. Viscosity plays an important role of diesel combustion and exhaust emissions. Figure 6 Shows the variation of absolute viscosity of diesel and different bio-diesel mixtures with respect to temperatures. It is clear from the figure that absolute viscosities of neat diesel fuel and different bio-diesel mixtures decrease with increased temperature and vice versa. By increasing the temperature of the fluid, the inter molecular attraction between different layers of the fluid decreases, thus viscosity decreases.

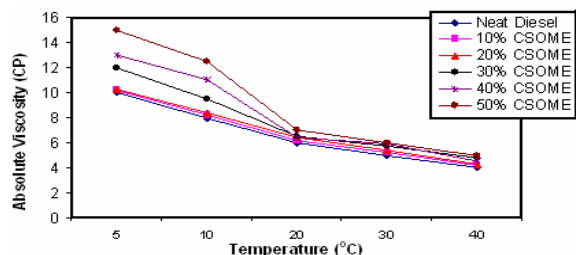


Figure 6. Variation of Absolute Viscosity of different Diesel-Biodiesel blends with respect to Temperature.

The figure also indicates that viscosity increases with the increase of bio-diesel percentages. For proper functioning of the engine, it

is necessary to reduce the viscosity of a fuel. Fuel with relatively higher viscosity will not break into fine particles when sprayed. Large particles will burn slowly resulting in poor engine performance. On the other hand, if the viscosity is too low, the fuel will not lubricate the moving parts of the injection pump and injection nozzle. This causes rapid wear of those parts. For operating, a temperature range of 20-40°C up to B50 (50% CSOME) can be effectively used. For temperature range below 20°C, it is necessary to keep the bio-diesel percentages as low as possible.

Table 2. Properties of neat diesel fuel and CSOME.

Properties	Neat diesel fuel	CSOME	ASTM Method
Chemical formula	C _{14.09} H _{24.78}	C ₅₄ H ₁₀₁ O ₆	-
Kinematic viscosity (mm ² /s) at 40°C	3.8	6.1	D445
Density (kg/m ³) at 15°C	836	848	D 1298
Higher calorific value (KJ/Kg)	43,850	40,610	D 5865
Flash point (°C)	55	200	-
Cetane number	49	53	D613
Cloud point (°C)	-20	-2	D2500
Pour point (°C)	-24	-5	D97
Carbon mass (wt %)	84.6	76.0	D3176
Hydrogen (wt %)	12.8	11.9	D3176
Oxygen (wt %)	0.00	10.36	D3176
C/H ratio	6.32	6.11	D3176
Sulfur (wt %)	0.038	<0.004	D3176
Distillation (°C)	-	-	D86
10%	225	238	-
50%	268	290	-
90%	326	361	-

4.3. Optimization of Engine Speed

Figure 7. shows the brake thermal efficiency (BTE) with neat diesel fuel at different engine speeds. To optimize the engine speed, BTE versus engine speed curve has been drawn. The BTE is defined as the actual brake work per cycle divided by the amount of fuel chemical energy as indicated by the lower heating

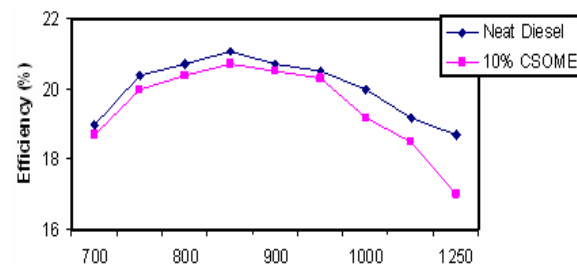
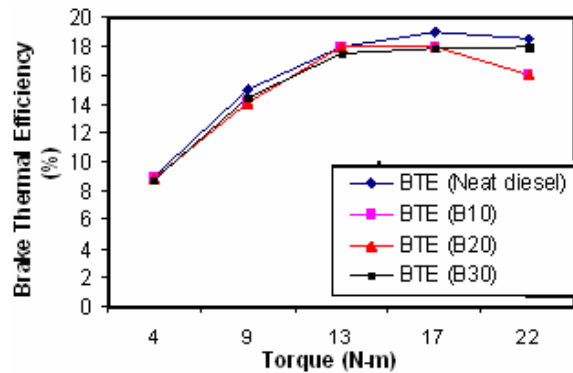


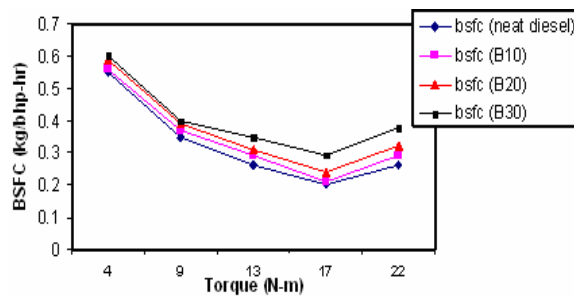
Figure 7. Effect of Engine Speed on Brake Thermal Efficiency (Load = 49N).

value of fuel. As can be seen in the figure, with the increase in engine speed up to 850 rpm, the BTE increases. This was due to the fact that with the increase in engine speed, the output power of the engine increases. As power increases, the engine BTE increases as well. The BTE of the engine decreases when the engine was run at a speed above 850 rpm.

4.3.1. Brake Thermal Efficiency and Brake Specific Fuel Consumption.



(a)



(b)

Figure 8. (a) Effect of Engine Torque on Brake Thermal Efficiency (Engine speed 850rpm), (b) Effect of Engine Torque on Brake Specific Fuel Consumption (Engine speed 850rpm).

Figure 8 (a) and (b). Illustrate the variation of BTE and brake specific fuel consumption (BSFC) with engine torque using neat diesel fuel and bio-diesel mixtures. Figure8-a. shows that the efficiency increases with the increase in engine torque and, after reaching maximum value, efficiency decreases with the increase of torque. On the other hand, according to Figure8-b., BSFC decreases with the increase in engine torque and becomes minimum and then increases again. It can be seen from the figure that in case of biodiesel mixtures, the BSFC values were determined to be higher than those of neat diesel fuel, and thus more biodiesel mixtures were required for the maintenance of a constant power output. It is well known that BSFC is inversely proportional with the BTE. From the figure, it was learned that BTE with biodiesel mixtures was little lower than that of neat diesel fuel. The slight reduction of BTE with biodiesel mixtures was attributed to poor spray characteristics, poor air fuel mixing, higher viscosity, higher volatility and lower calorific value.

4.4. Exhaust Emissions with Neat Diesel Fuel and Biodiesel Mixtures.

4.4.1. CO Emissions.

Figure 9. Shows the CO emissions of the neat diesel fuel and the biodiesel mixtures. CO is an intermediate combustion product and is formed mainly due to incomplete combustion of fuel. If combustion is complete, CO is converted to CO₂. If the combustion is incomplete due to shortage of air or due to low gas

temperature, CO will be formed. Usually high diesel CO emissions are formed with fuel-rich mixtures, but as diesel combustion is occurred with lean mixture and has an abundant amount of air, CO from diesel combustions is low. The comparative analysis of CO is shown in Figure9. For bio-diesel mixtures CO emission was lower than that of diesel fuel, because biodiesel mixture contains some extra oxygen in their molecule that resulted in complete combustion of the fuel and supplied the necessary oxygen to convert CO to CO₂. Compared to neat diesel fuel, 30% bio-diesel mixtures reduced CO emissions by 24%.

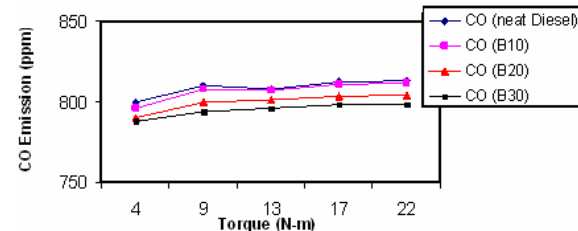


Figure 9. Variation of CO emission with Engine Torque for Neat Diesel and Bio-Diesel Mixture (engine speed 850rpm).

4.4.2. NO_x Emissions.

Figure 10. shows the effect of engine torque on NO_x emission. Naturally NO_x emission increases with the increase in engine torque. It is well known that nitrogen is an inert gas, but it remains inert up to a certain temperature (1100°C) and above this level it does not remain inert and it participates in chemical reaction. At the end of the combustion, gas temperature inside cylinder arises around 1500°C. At this temperature oxidation of nitrogen takes place in presence of oxygen inside the cylinder. On the other hand, since the formation of nitrogen oxides do not attain chemical equilibrium reaction, then after the end of expansion stroke when the burned gases cool and the formation of NO_x freeze, the concentration of the formed NO_x in the exhaust gas remain unchanged. Figure10. also shows that NO_x level was higher for biodiesel mixtures than conventional diesel fuel at the same engine torque. This occurs due to the presence of extra oxygen in the molecules of Bio-diesel mixtures. This additional oxygen was responsible for extra NO_x emission. Approximately 10% increase in NO_x emission was realized with 30% biodiesel mixtures. Reduction of NO_x with biodiesel may be possible with the proper adjustment of injection timing and the introduction to exhaust gas recirculation. (EGR).

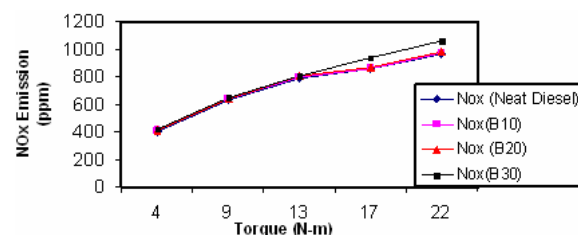


Figure 10. Variation of NOx emission with Engine Torque for Neat Diesel and Bio-Diesel Mixture (engine speed 850 rpm).

4.4.3. PM Emissions.

Figure 11. Shows the PM emission with neat diesel fuel and 20% biodiesel mixtures. The primary reason of the particulate emission from CI engine is improper combustion and combustion of heavy lubricating oil. Diesel PM (some times also called diesel exhaust particles (DEP)), is the particulate component of diesel exhaust, which includes diesel soot and aerosols such as ash particulates, metallic abrasion particles, sulfates, and silicates. When released into the atmosphere, PM can take the form of individual particles. In this experiment, PM was measured by

filter cloth method. It was found that particulate emission with 20% biodiesel mixture was lower than that of neat diesel fuel because neat biodiesel contains 10-12% extra oxygen, which resulted in better combustion, lowers PM emission. With 20% biodiesel mixtures, PM emission was reduced by 24% compared with neat diesel fuel.

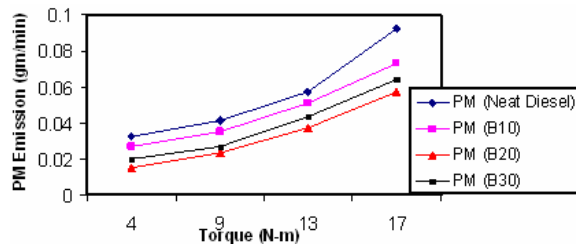


Figure 11. Variation of Particulate Matter Emission with Torque (engine speed 850 rpm).

4.4.4. Smoke Emission.

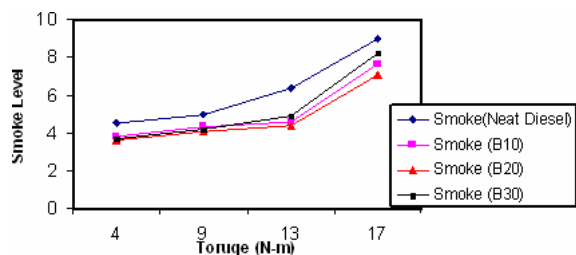


Figure 12. Variation of Smoke Emission with Torque (Engine Speed 850rpm).

The variation of smoke emission with engine torque for neat diesel fuel and 10% mixture was shown in Figure 12. For 10% biodiesel mixtures, smoke emission was less, compared to neat diesel fuel. The maximum reduction of smoke emission with 10% biodiesel mixtures was observed by 14%. Because of the heterogeneous nature of diesel combustion, fuel-air ratio, which affects smoke formation, tends to vary within the cylinder of a diesel engine. Smoke formation occurs primarily in the fuel-rich zone of the cylinder, at high temperatures and pressures. If the applied fuel is partially oxygenated, locally over-rich regions can be reduced and primary smoke formation can be limited.

5. Conclusions

Cottonseed oil methyl ester (CSOME) was produced by means of transesterification process using cottonseed oil, which can be described as a renewable energy sources. The viscosity of CSOME was reduced by preheating it before supplying it to the test engine. After the fuel properties of CSOME have been determined, various performance parameters and exhaust emission of the engine were investigated and compared with those of diesel fuel. The experimental conclusions of this investigation can be summarized as follows.

- Kinematics viscosity and flash point of CSOME are higher than those of diesel fuel.
- A maximum of 76% BD production was found at 20% methanol and 0.5% NaOCH_3 at 55°C reaction temperature.
- Thermal efficiency with biodiesel mixtures was slightly lower than that of neat diesel fuel due to lower heating value of the mixtures. However, volatility, higher

viscosity, higher density may be additional reasons for efficiency reduction with biodiesel mixtures.

- Biodiesel mixtures showed less CO, PM, smoke emission than those of neat diesel fuel.
- NOx emission with biodiesel mixtures showed higher values when compared with neat diesel fuel.
- Compared to the neat diesel fuel, 10% BD mixtures reduced PM, smoke emission by 24% and 14% respectively.
- Biodiesel mixtures (30%) reduced CO emission by 24%, while 10% increase in the NOx emission was experienced with the same blend. The reason for reducing three emissions (PM, smoke and CO) and increasing NOx emission with biodiesel mixtures was mainly due to the presence of oxygen in their molecular structure. Also low aromatics in the biodiesel mixtures may be an additional reason for reducing these emissions.

References

- [1] M. S. Graboski, R. L. McCormick, "Combustion of fat and vegetable oil derived fuels in diesel engines". Pergramm, Vol. 2, 1998, 125-164.
- [2] M. A. Hanna, "Biodiesel production: a review". Bio resource Technol, 2004, 1-15.
- [3] M. Canakci, J. Van gerpen, "Biodiesel production from oils and fats with high free fatty acids". Trans ASME, Vol. 44, No. 6, 2001, 1429-36.
- [4] A. Keskin, A. Kadir, G. D. Metin, "Using of cotton oil soap stock bio-diesel - diesel fuel blends as an alternative diesel fuel". Renewable energy Journal, Vol. 33, 2008, 553-557.
- [5] M. S. Graboski, R. L. McCormick, "Combustion of fat and vegetable oil derived fuels in diesel engines". Prog Energy Combust Sci, Vol. 24, 1998, 125-64.
- [6] A.S Ramadhas, S. Jayaraj, C Muraleedharan, "Use of vegetable oils as IC engine fuels A review". Renewable energy, Vol.29, 2003,727-742.
- [7] E. G. Shay, "Diesel fuel from vegetable oil; status and opportunities". Biomass bio energy, Vol. 4, No. 4, 1993, 227-242.
- [8] B.K. Barnwal, "Prospects of Biodiesel production from vegetable oils in India". Renewable and Sustainable Energy Reviews, Vol. 9, 2005, 363-378.
- [9] K. Aydin, A. keskin, "Investigation of performance and emission of vegetable oil and alcohol mixture in a diesel engine". In: proceedings of the Vth national combustion and air pollution symposium, Turkey, 2000, 49-54.
- [10] A. V. Tomasevic, S. S. Marinkovic, "Methanolysis of used frying oil". Fuel process technol, 2003, 81:1-6.
- [11] A. S. Kumar, D. Maheshwar, K. Kumar, "Transesterification process of bio-diesel". Proceeding of REA, Delhi, 11-13 Dec 2008, 623-631.
- [12] V.Gerpen, "A pilot plant to produce biodiesel from high free fatty acid feedstock", American society of agricultural engineers, Vol. 46, No. 4, 2003, 945-954.
- [13] B. baiju, M. Das, M. K. babu, "Engine performance and emission studies using rubber seed biodiesel and karanja biodiesel as a fuel in a compression ignition engine". Proceeding of REA 2008, Delhi, 11-13 Dec 2008, 658-673.
- [14] T. Krawezy, "Biodiesel- alternative fuel makes in roads but hurdles remain". INFORM 1996, Vol. 7, No. 8, 800-815.
- [15] A. Bijalwan, "Bio-diesel revolution". Science Reporter, January 2006, 14-17.

- [16] I.V. Subba, General president Indian science congress association, "Presidential address." 93rd Indian science congress annual report, 2005-2006.
- [17] A. P. J. Abdul Kalam, Hon'ble president of India, "Dynamics of rural development". 93rd Indian science congress annual report, 2005-2006.
- [18] C. M. Narayan, "Vegetable oil as engine fuels- prospect and retrospect." Proceedings on recent trends in Automotive fuels, Nagapur, India, 2002.

Thermal Simulation of a Pyrotechnic Solid-Propellant Gas Generator

Mohammad K. Alkam^{a,*}, P. Barry Butler^b

^aDepartment of Mechanical Engineering Jordan University of Science and Technology Irbid, Jordan

^bDepartment of Mechanical and Industrial Engineering, The University of Iowa, Iowa City, IA 52242, U.S.A

Abstract

The current work presents a numerical simulation of the thermal operation of a pyrotechnic solid propellant gas generator undergoing a tank test. The effect of several parameters on the thermal characteristics of the system under consideration is investigated. These parameters include heat loss to the ambient, heat transfer to the hardware elements of the present system, and ambient temperature. The question of the applicability of tank test results to auto airbag systems has been addressed. In the present work, it has been concluded that the thermal performance of present system is significantly sensitive to heat transfer to the tank wall and to the value of the ambient temperature.

© 2009 Jordan Journal of Mechanical and Industrial Engineering. All rights reserved

Keywords: Pyrotechnic; Gas Generator; Airbag; Tank-Test.

Nomenclature			ΔT	change in temperature (T-298 K)	K
			U	internal energy	J/g
Variable	Definition	Dimension	V	volume	cm ³
A	area	cm ²	W _k	molecular weight of species k	g/mol
a	propellant burning rate prefactor	cm/(s-MPa ⁿ)	W	mixture molecular weight	g/mol
C _d	discharge coefficient		Y	mass fraction	
C _p	constant pressure specific heat	J/g-K	Greek		
C _v	constant volume specific heat	J/g-K	γ	specific heat ratio	
d	grain diameter	cm	ρ	density	g/cm ³
H	enthalpy	J/g	$\dot{\omega}$	gas-phase mass production	g/s
H _f	enthalpy of formation	J/g	φ	volume fraction of condensed-phase species	
j	computational cell index		σ	propellant temperature-sensitivity coefficient	K ⁻¹
k	species index		Subscripts		
kk	total number of species		c	combustion chamber	
L	length	cm	eff	effective	
m	mass	g	gen	generant (propellant)	
\dot{m}	mass production rate	g/s	gr	grain	
N	number of propellant grains		ign	ignitor	
P	pressure	N/m ²	j	gas cell index	
Q	energy transfer	J	k	species index	
\dot{Q}	energy transfer rate	J/s	M	hardware cell index	
r	burn depth	cm	P	product	
R	gas constant = R _u /W	J/g-K	p	plenum	
RI	inner radius	cm	ref	reference state (298 K, 1 atmosphere)	
RO	outer radius	cm	R	reactant	
R _u	universal gas constant	J/mol-K	t	discharge tank	
T	temperature	K	Superscripts		
To	ambient temperature	K	H	hardware	
			n	propellant burning-rate pressure index	
			gas	gas-phase	

* Corresponding author. alkam@just.edu.jo.

cond condensed-phase
o standard-state

1. Introduction

Solid propellant gas-generators have several engineering applications. Among these applications are pilot emergency escape systems, missile launching, powering actuators and valves, and short-term power supplying [1]. Of special interest to the present work is the performance of solid propellant gas generators used in automotive applications. Current automotive applications include inflation devices for driver, passenger and side impact airbags and knee bolsters, and piston actuators for automatic seat belt tensioners. Contemporary airbag systems can be classified into two major groups based on the configuration used to produce gas for inflating a vehicle airbag [2]. The first group is referred to as "pyrotechnic" in which the air bag is inflated solely by rapid gas production from a solid propellant. The second group is referred to as "augmented" in which hot gases produced from a solid propellant are diluted by an ambient-temperature, high-pressure stored gas before the gas mixture is discharged into the airbag. However, earlier airbag configurations (over the 1960's) relied solely on pressurized, ambient-temperature stored gas to inflate airbags [3].

There are several issues of considerable concern to the designer of an automotive airbag system. These issues include: 1) the size of the inflator, 2) the volume ought to be occupied by the inflated airbag, 3) the transients of the airbag operation, especially the time duration of the inflating process, 4) the force exerted by the airbag on the driver and/or the passenger upon the inflating process, 5) the sensitivity of the airbag-system performance to a wide range of ambient conditions, 6) the reliability of the airbag system over a relatively long period of time that spans over 20 years, and 7) the thermophysical properties of the utilized propellant. In an investigation conducted by Berger and Butler [4], the authors studied the decomposition behavior of three condensed-phase propellants commonly used in airbag industry. These propellants are 1) sodium-azide (NaN_3), 2) a non-azide propellant containing azodicarbinamide (ADCA), and 3) a double-based propellant (DB). In their work, Berger and Butler studied several thermophysical properties of the above mentioned propellants including a) the flame temperature and chemical composition of the product gases, b) the number of gaseous moles produced per mass of condensed phase propellant consumed, c) the condensed-phase (slag) production of each propellant, and d) and the toxicity of gas-phase combustion products. It has been concluded that there is a trade off between the advantage of producing large number of gaseous moles per unit mass of solid propellant and the advantage of having a lower flame temperature. The study showed that among the three propellants under consideration, NaN_3 has the lowest flame temperature, but also the lowest gas production per unit mass of propellant. The study concluded also that there is a negative correlation between the flame temperature and the amount of slag produced. In another study, Ulas et al. [5] conducted an experimental investigation on the determination of ballistic properties

and burning behavior of a composite solid propellant for airbag application. In their article, it was reported that the pressure exponent was found to be a strong function of the initial propellant temperature. They also introduced the values of the activation energy and the pre-exponential factor of the Arrhenius equation.

There appears to be a current demand for novel designs of airbag systems such that the output of the airbag operation could be controlled according to different crash conditions. These types of airbags are referred to as "smart" airbags. One method being studied for controllable output is to add a second solid-propellant combustion chamber to a standard augmented gas generator [6]. The traditional single-combustor gas generator is designed around a single operating state. For example, in the U.S. this is specified as being sufficient to protect an unbelted, 74.5-kg adult in a 48-km/hr frontal collision. All other operating conditions are considered off-design. The augmented, dual-combustion chamber design presented in ref. [6] can be optimized for three operating conditions to, consequently, have a more uniform off-design performance. The wider range of acceptable operation is a result of dynamic controllability of the discharge process to match the kinematics of the occupant as they are thrown towards the deploying airbag.

In airbag industry, the performance of an airbag inflator is often evaluated by conducting what is commonly called "tank test". In a tank test, the combustion products are allowed to flow into a rigid tank that is initially filled with ambient air; in the meanwhile pressure and temperature histories of the combustion products in the tank are observed. Besides, the final product composition is measured. In an auto airbag operation, the combustion products flow into an inflatable airbag rather than a rigid tank. From a thermal point of view, that is the major difference between the operation of an auto airbag and a tank test operation, given that all other design and operating conditions are similar. The question remains whether the tank test provides satisfactory description of the auto airbag inflating process. One important issue is the amount of energy lost within the hardware components of the system under consideration, especially the tank wall. This energy plays a major role in the thermal behavior of the products of combustion. Hence, investigating the amount of energy lost within each hardware component could help judge whether the tank test is an acceptable representation of the auto airbag operation. Besides, it would provide a better understanding of the thermal transients of the airbag operation. In a recent study, Sinz and Hermann [7] have developed an algorithm for simulation of an airbag deployment.

In the present work, it is intended to evaluate the performance of a pyrotechnic solid-propellant gas generator in a conventional tank-test environment. Special emphasis is put on the heat balance characteristics of the system at hand. The analysis is performed using AIM; a program designed to simulate the transient, thermochemical events associated with the firing of a solid propellant gas generator [8]. AIM models the processes of gas generation and discharge which are highly nonlinear events governed by first principles (i.e., solving complete conservation equations, variable specific heats, mixture mixing rules, etc.). AIM also includes the dynamics of

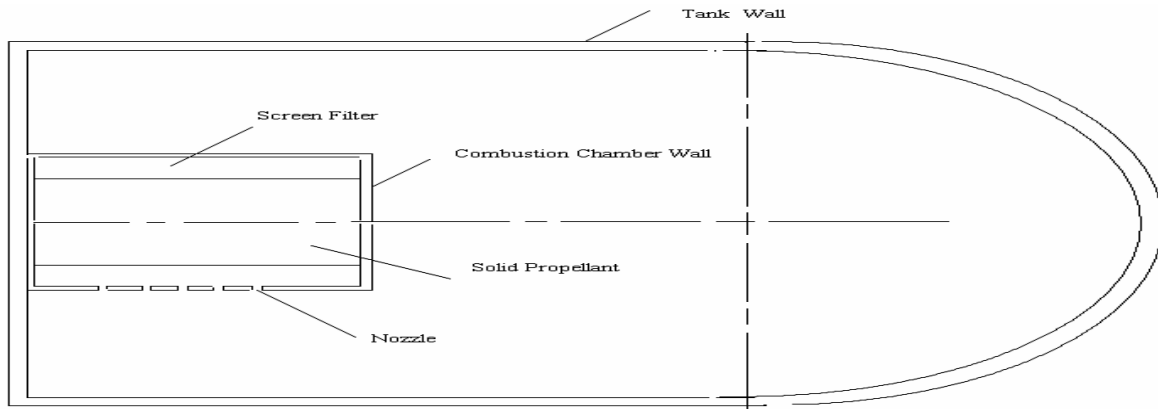


Figure 1: Schematic Diagram of the present problem/

coupled events such as ignition, heterogeneous combustion, particle filtering, heat transfer, phase change, and mass discharge. Further demands arise when the simulation also takes into consideration the temperature gradients within the walls of the hardware components.

2. Problem Description

The present work introduces thermal analysis of a conventional pyrotechnic solid propellant gas generator. This gas generator is based on the approximate design specifications of an inflator of a passenger-side airbag. The inflator at hand delivers the combustion products into a constant volume tank such that the pressure inside the tank is elevated into a certain value without exceeding a maximum tank pressurization rate. A schematic diagram of the setup under consideration is shown in Fig. 1. The combustion chamber contains the main propellant along with a small amount of ignitor propellant. The mass of propellant occupies a portion of the total volume within the combustion chamber. Also, within the combustion chamber is a metallic screen used to capture condensed-phase particulate and to cool the exiting gases. The screen, with a specified mass, has a hollow cylindrical shape and it is located at the inner wall of the combustion chamber. The combustion products exit the combustion chamber through an array of nozzles each of individual flow characteristics. The nozzles are initially covered with a burst foil that seals the interior of the combustion chamber from the surrounding tank. The burst foil is designed to rupture when the pressure within the combustion chamber reaches a predetermined burst pressure. The discharge tank is a constant-volume cylindrical vessel with a hemispherical top. It has a volume that is several orders of magnitude larger than the volume of the gas generator and it has no exit nozzles. The only inlet into the discharge tank comes from the exit nozzles of the combustion chamber. Initially, the discharge tank contains air at atmospheric conditions.

3. Mathematical Model

The propellant used throughout this study is sodium-azide (NaN_3). It is assumed that the combustion process proceeds at an equilibrium state during the complete burning process of the propellant. It is also assumed that the surrounding conditions do not deviate substantially during the combustion process. Therefore, the distribution

of product species calculated at one flame state are assumed to be the same throughout the combustion process [9]. With these assumptions an adiabatic flame temperature calculation can be performed at an estimated average pressure within the combustion chamber.

The standard JANNAF [10] species database was used for calculating the thermochemical properties of the products of combustion for the propellant. Product species were chosen from this database by minimizing the Gibb's free energy of the reacting system within a specified tolerance while satisfying the elemental population constraint. PEP [11], a thermochemical equilibrium calculation program, was used to solve the system of equations to determine the adiabatic flame temperature and the relative amounts of product species.

The following premises dictate the mathematical formulation of the present model:

1. Gas-phase and condensed-phase combustion products are composed of multiple species.
2. Specific heats of the species present are temperature-dependent.
3. The existence of extreme turbulent mixing upon gas deployment results in much shorter fluid mixing time scales than diffusion time scales. This motivates the assumption of well-mixed gases, and hence gaseous and condensed-phase products are assumed spatially uniform within the combustion chamber, on the one hand, and the tank, on the other.
4. The use of the filtering screen restricts the solid propellant combustion to the combustion chamber.
5. Ignition of the solid propellant is represented by an empirical expression that was determined from experimental data.
6. Heat transfer within the combustion chamber and the tank walls is axisymmetric, i.e. the temperature within the hardware walls is function of axial and radial coordinates in addition to time.

The present conservation equations are derived by applying conservation principles of mass and energy to the computational domain under consideration. The computational domain of interest is divided into 1) three gas computational cells corresponding to the combustion chamber, the tank, and the ambient, respectively, and 2) a prescribed number of hardware cells that represent the combustion chamber and the tank walls. These cells are obtained by dividing the hardware walls into a number of finite element cells. The distribution of the gas

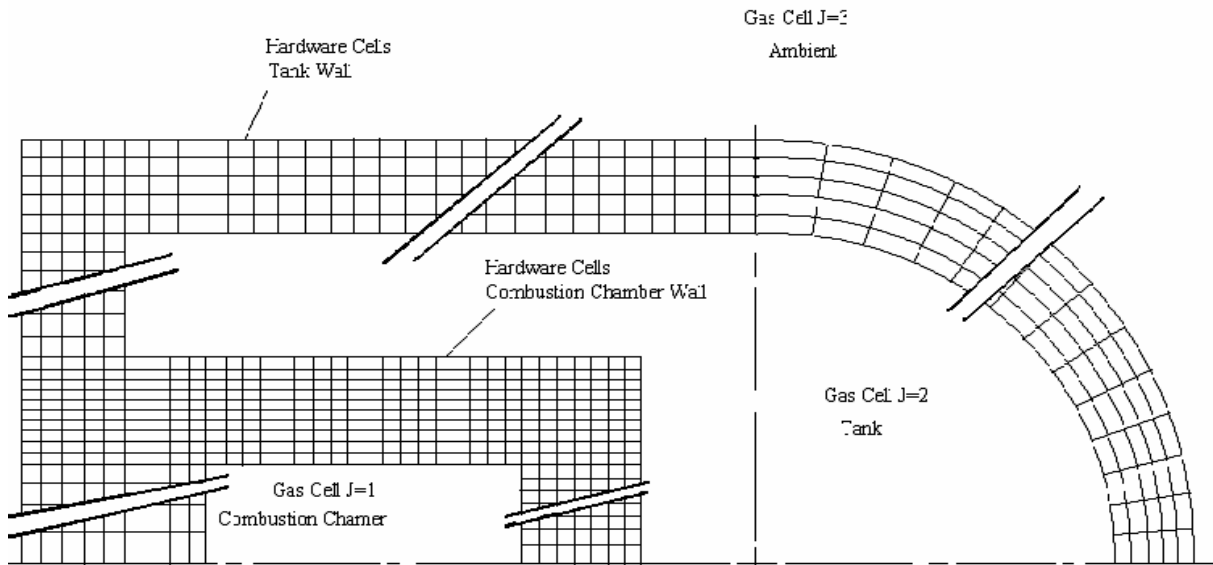


Figure 2. Distribution of the hardware Computational cells of the combustion chamber and the tank walls

computational cells as well as the hardware cells is depicted in Fig. 2.

Taking into consideration the set of assumptions listed above, the conservation equations of species mass and energy are applied to the individual volumetric cells within a gas generator system. The gas cells shown in Fig. 2 are designated with the index j , whereas the $j=1$ for the combustion chamber, $j=2$ for the tank, and $j=3$ for the ambient. The gas within the volumetric cell j of size V_j , is well mixed (spatially uniform) and has properties P_j, T_j, ρ_j . The mass inflow from cell $j-1$ is uniform across the inlet area and has properties P_{j-1}, T_{j-1} , and H_{j-1} where H_{j-1} is the enthalpy of the mixture in cell $j-1$. The hardware cells shown in Figs. 2 are designated with the index M , where M varies from 1 to M_t . Each hardware cell has a volume V_M , and has a temperature T_M .

For each gas-cell control volume j depicted in Figure 2, the conservation of species equation takes the following form:

$$\frac{dm_{k,j}}{dt} = Y_{k,j-1} \dot{m}_{j-1} - Y_{k,j} \dot{m}_j + \dot{\omega}_{k,j} + \dot{m}_{gen,k,j} \quad (1)$$

The sum of $\dot{\omega}_{k,j}$, the gas-phase mass production rate, and $\dot{m}_{gen,k,j}$, the mass addition due to propellant decomposition, represent the rate of mass production within the control volume, and Y_k is the mass fraction for species k . The energy equation for each gas cell is written as Formula 2 :

$$\frac{dI_j^{gas}}{dt} = \frac{1}{m_j^{gas} C_{vj}^{gas}} \left[\sum_{k=1}^{kk} (U_{k,j} \dot{\omega}_{k,j}) + H_{j-1}^{gas} \dot{m}_{j-1}^{gas} - H_j^{gas} \dot{m}_j^{gas} + \dot{Q}_j^{gas} + H_j^{gas} \dot{m}_{gen,j}^{gas} + P V_j^{gas} \frac{d\phi_j}{dt} \right]$$

The production of gas from a burning propellant is dependent on the propellant surface regression rate \dot{r}_{gr} , instantaneous propellant grain surface area A_{gr} , and propellant density ρ_{prop} . The propellant burning rate is modeled as a function of pressure and variation from

ambient temperature ΔT and is represented by the form [12].

$$\dot{r}_{gr} = a e^{\sigma \Delta T} P^n \quad (3)$$

Here, r_{gr} is the burn depth measured from the initial surface of the propellant. Equation 3 is a typical burn-rate function for propellants under quasi-steady-state pressure conditions. The variation of the propellant grain surface area, on which a flame is propagating, with burn depth, is primarily dependent on the geometry of the propellant grain as well as flame spreading characteristics and can also change due to grain fracture. The variation of the propellant grain surface area, on which a flame is propagating, with burn depth, is called the form function of the grain and is primarily dependent on the geometry of the propellant grain as well as flame spreading characteristics and can also change due to grain fracture. For this study, it is assumed that the form function is only a function of grain geometry. Thus, it is assumed that flame spread is instantaneous on the grain surface at the time of ignition and no grain fracture occurs. Analyzing the regression of the propellant grain shape can develop a form function based solely on geometry. For all results presented herein, the propellant grains are modeled as solid right circular cylinders, initially 1.1 cm in length and 4.1 cm in diameter which burn uniformly on all exposed surfaces. The right circular cylinder geometric shape provides a well-defined mathematical relationship between surface area of the propellant grain and the burn depth.

The total rate of mass addition to the system due to propellant decomposition is:

$$\dot{m}_{prop} = N_{gr} A_{gr} \rho_{prop} \dot{r}_{gr} \quad (4)$$

Combining the rates of mass production rate from the propellant and ignitor charge according to Eq. (5) provides closure for the addition of mass to the system and completes the necessary relations to conserve mass within the gas generator system.

$$\dot{m}_{gen} = \dot{m}_{ign} + \dot{m}_{prof} \quad (5)$$

The mass flow exiting each volumetric cell through the local nozzles is classified as either in the sonic or subsonic flow regime, depending on the pressure difference between the adjacent cells and the specific heat ratio of the gaseous mixture within the volumetric cell from which the gases are exiting. The choked flow critical condition is calculated to determine whether a sonic or subsonic flow condition exists for the mass flow between two cells using the above parameters. Applying the fundamental laws of gas dynamics, the gas-phase mass flow rate is determined from the following sonic and subsonic relations.

Subsonic formula 6:

$$\dot{m}^{gas} = A_{flow} C_d \sqrt{\frac{2\gamma}{\gamma-1} P_+ \rho_+ \left[\left(\frac{P_+}{P_-} \right)^{\frac{2}{\gamma}} - \left(\frac{P_+}{P_-} \right)^{\frac{\gamma+1}{\gamma}} \right]}$$

Sonic formula 7:

$$\dot{m}^{gas} = A_{flow} C_d \sqrt{\gamma P_+ \rho_+} \left(\frac{2}{\gamma+1} \right)^{\frac{\gamma+1}{2(\gamma-1)}}$$

In Eqs. (6) and (7), A_{flow} and C_d are the respective flow area and discharge coefficient for the given nozzle [13]. The subscripts '+' refers to the high-pressure chamber and '-' refers to the low-pressure chamber.

The term (\dot{Q}_j^{gas}) that appears in Eq. (2) represents the net heat transfer between the gas in cell J and all the hardware cells that are in direct thermal communication with the gas in this specific cell. The calculation of this term is based on an effective heat transfer coefficient, h_{eff} , obtained from Nusselt number correlations according to the geometrical and flow conditions of the local flow [8].

The energy equation for each hardware cell is written as:

$$\frac{dT_M^H}{dt} = \frac{\dot{Q}_M^H}{m_M^H C_{vM}^H} \quad (8)$$

where the term (\dot{Q}_M^H) represents the net heat transfer exchange between the hardware cell M and all the computational cells that are in direct thermal communication with the hardware cell M. This term includes: 1) heat exchange between a specific hardware cell and the adjacent gas cell (\dot{Q}_M^H) , and 2) heat exchange between a specific hardware cell and all other adjacent hardware cells. This part of heat exchange is calculated in a quasi equilibrium fashion assuming the hardware material has constant physical properties. In other words, the heat flux between two adjacent hardware cells in certain direction equals the thermal conductivity multiplied by the temperature gradient between the two cells in that direction divided by the appropriate length scale.

Individual gas- and condensed-phase chemical species are tracked throughout the numerical simulation, thus requiring thermodynamic properties for each chemical species over a wide range of conditions. A fourth-order polynomial expansion in temperature is used to represent the standard-state, constant-pressure specific heat data for the individual species $C_{p,k}^o(T)$. Standard-state enthalpy of the species can be determined by the fundamental thermodynamic relationship:

$$H_k^o(T) = \int_{T_{ref}}^T C_{p,k}^o(T) dT + H_{f,k}^o(T_{ref}) \quad (9)$$

All condensed-phase species are considered incompressible:

$$\rho_{cond,j} = \text{constant} \quad (10)$$

where R_j , the gas constant for cell j, is dependent on the local mixture molecular weight: $W_j = \sum X_k W_k$. From this derivation, a system of ordinary differential equations is developed to express the time derivatives of all dependent variables: gas- and condensed-phase temperatures, individual species mass, and gas pressure within each gas cell, in addition to hardware temperatures. These differential equations combine with the constitutive relations to form the governing equations for the gas generator systems.

4. Discussion of Results

The results of the present work are obtained using a stoichiometric mixture of NaN_3 and Cu_2O . This composition is often used in airbag industry. A thermochemical equilibrium code [11] has been used to characterize the equilibrium composition of the present propellant. Table 1 describes the composition of both the reactants and the products of combustion of the problem under consideration, given that the reactants exist at ambient conditions and the products exist at the adiabatic flame temperature of the present mixture. Table 1 shows that 60.412 % of the product mass is in condensed phase, while the gaseous products are mainly composed of N_2 . Hence, the gas-phase reactions within the combustion products are neglected and all chemical species present at the calculated adiabatic flame temperature are assumed to be chemically frozen.

The present results are obtained using the software AIM [8]. AIM incorporates the chemical kinetic package CHEMKIN [14] to evaluate thermodynamic properties for all species present. It also uses the ordinary differential equations solver LSODE [15] to solve the resulting set of ordinary differential equations along with the proper initial conditions numerically. Besides, all chemical species are characterized in terms of standard-state, temperature-dependent specific heat functions, heats of formation and entropies of formation. These chemical species data are taken from JANAF thermodynamic tables [10]. Table 2 shows the initial, operating, and design conditions that

have been used throughout the present computations. These conditions resemble a generic inflator system.

The operating and design conditions that appear in Tables 1 and 2 have been used to produce the results of present case study. Throughout this text, these conditions will be referred to as "basic conditions". All the figures in the present work have been produced using the basic conditions unless otherwise stated. AIM computations have been verified in ref. [6]. The authors presented a comparison between AIM computations and analytical solutions for two standard problems, namely, isentropic and isothermal discharges of constant volume pressurized chamber.

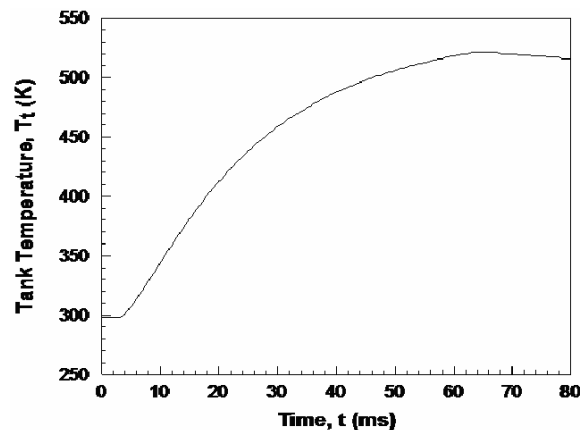


Figure 3. Temperature history inside the tank.

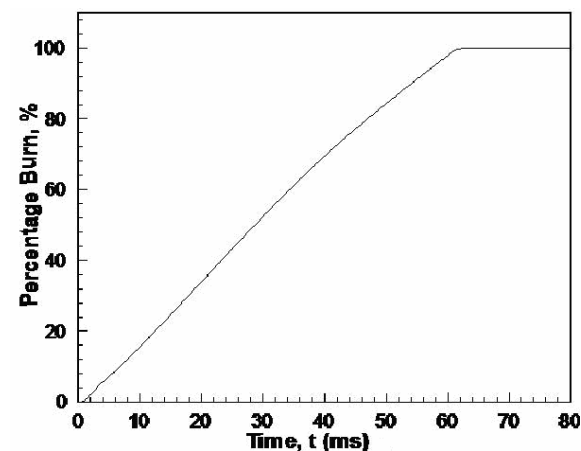


Figure 4. History of the fuel percentage burn.

The temperature history of the gases inside the tank is shown in Fig. 3. The maximum value of the gas-temperature inside the tank is reached after about 60 ms from the beginning of combustion. At this instant, almost all of the solid propellant have just been burned as shown in Fig. 4.

The performance of an airbag inflator is commonly evaluated by several parameters. Among these parameters are the maximum pressure rise-rate, the peak pressure and temperature within a standard discharge tank, and the time integral of the pressure inside the discharge tank (pressure impulse). The maximum pressure rise-rate affects the airbag transients upon the inflating process. The peak pressure and temperature, and the pressure impulse inside the tank are key issues in the safety considerations of a vehicle occupant. The pressure impulse provides a

Table 1. Chemical composition of solid propellant and combustion products.

Propellant Formulation				
Component	Phase	Mass %	Mole %	Molecular Weight
NaN ₃	S	60.998	77.488	65.01
Cu ₂ O	S	39.002	22.512	143.08
Combustion Products				
N ₂	G	39.451	53.807	28.01
Cu	S	34.661	20.842	63.54
Na	L	8.846	14.702	22.99
Na	G	0.136	0.227	22.99
Na ₂ O	S	16.905	10.421	61.98

Table 2. Present system parameters.

Variable (units)	Value
Combustion chamber material	Aluminum
Nozzles (Diameter(m) , Number)	(0.006,18) (0.005,12)
ρ_c (kg/m ³)	2770
ρ_t (kg/m ³)	7854
Filter material	Carbon Steel
m_c (kg)	0.68
m_{Filter} (kg)	0.5467
L_c (m)	0.2712
L_{Filter} (m)	0.247
m_p (kg)	0.445
N	14
RI_c (m)	0.02615
RI_{Filter} (m)	0.0205
RO_c (m)	0.03055
RO_{Filter} (m)	0.0255
Tank material	Carbon Steel
V_c (m ³)	0.0005826
V_t (m ³)	0.06

computations with and without heat transfer to the tank walls.

measure of the momentum transferred to a vehicle occupant. The peak pressure within the discharge tank provides a measure of the discharged energy of an inflator system. In airbag industry, the conventional tank test has been used to evaluate the performance of airbag inflators. The question that rises is whether or not the tank test conditions resemble the actual operation of the airbag. There is a considerable difference between heat transfer to the wall of the discharge tank and heat transfer to the airbag. This may lead to a significant difference between the thermal behavior of an airbag operation and that of a tank test. It is intended to investigate the sensitivity of the tank test output to the amount of heat transfer to the tank wall. This could help evaluate the need for more research on the airbag itself rather than the tank test. For that purpose, the pressure history inside the tank is plotted in Fig.5. The figure compares the present calculations of the pressure transients with a similar case but without heat transfer to the tank wall. It is clear that both the peak pressure and the pressure rise-rate are considerably sensitive to heat transfer to the tank wall. This result

suggests that one should be careful upon applying the tank test results on airbag systems directly.

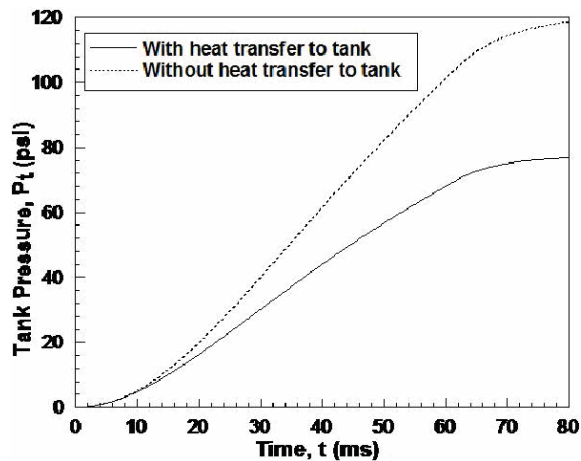


Figure 5. Computation of the tank pressure history. Comparison between

The high sensitivity of the thermal characteristics of the present system to heat transfer (observed in Fig. 5) creates an interest in the heat transfer issue of airbag systems. It is interesting to perform an energy balance to find out how much energy is lost through heat transfer to the hardware during the operation of the current system. Figure 6 presents the history of the integrated amount of heat transfer to the combustion chamber wall, the screen filter, the tank wall, and the ambient. It Fig. 6, it is shown that the heat loss to the ambient is negligible. At the same time, the tank wall absorbs energy the least, while the combustion chamber wall absorbs energy the most among the hardware elements. However, Fig. 5 shows that the present system is significantly sensitive to the heat transfer to the tank wall. Figures 5 and 6 demonstrate the importance of heat transfer to the hardware in modeling airbag systems.

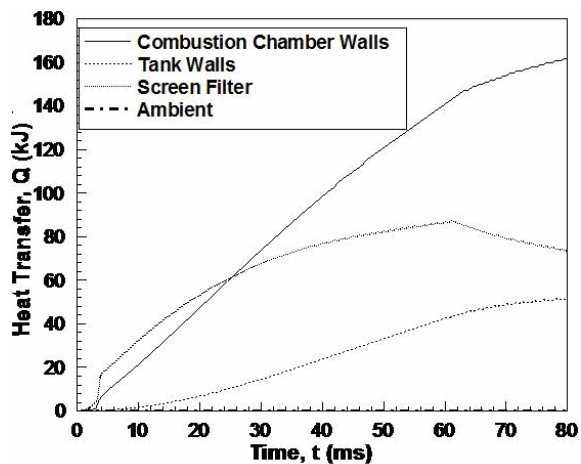


Figure 6. History of the heat absorbed by the combustion chamber walls, the tank walls, the screen filter, and the ambient.

An important issue in the design of airbags systems is the sensitivity of the airbag performance to ambient conditions. Airbags operate under a wide range of ambient temperatures that might span from 230 to 320 K. It is essential to investigate the performance of the present sample case under a broad extent of ambient temperatures. The effect of ambient temperature on the tank pressure

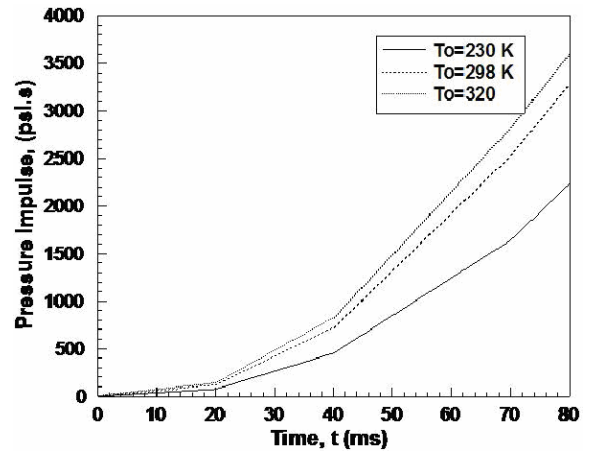


Figure 7. Effect of ambient temperature on the history of the pressure impulse.

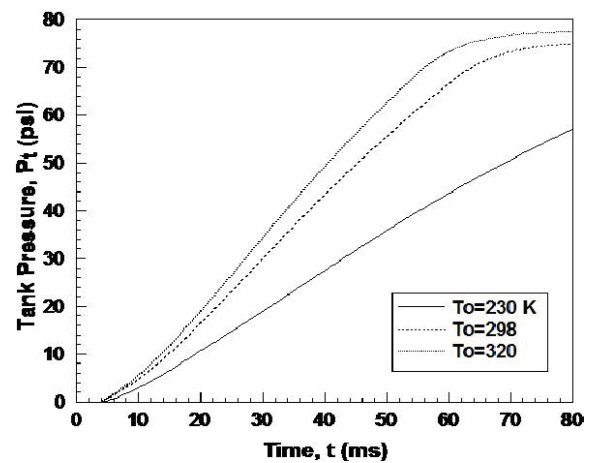


Figure 8. Effect of ambient temperature on tank pressure history.

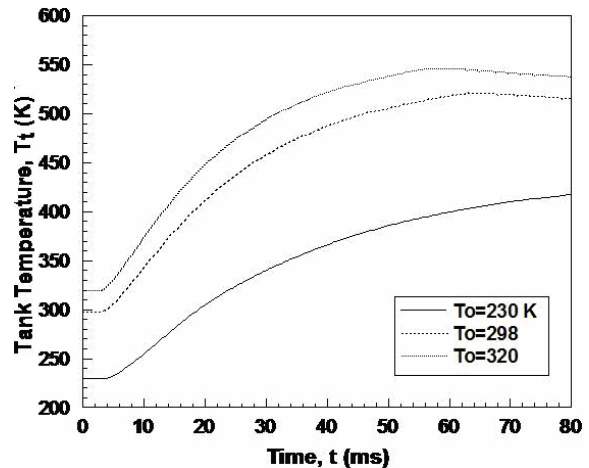


Figure 9. Effect of ambient temperature on tank temperature .

impulse is shown in Fig. 7. The figure shows that the tank pressure impulse at an ambient temperature of 320 K is around 50 % larger than that at an ambient temperature of 230 K. Further explanation of the effect of ambient temperature of the thermal characteristics of the present system is presented in Figs. 8, 9, and 10. Figure 8 shows that as the ambient temperature increases the maximum pressure inside the tank as well as the maximum pressure rise-rate increases considerably. The increase in ambient temperature increases the temperature level of the inflating

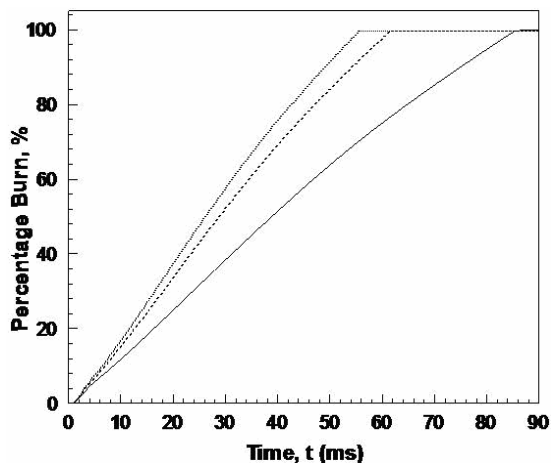


Figure 10. Effect of ambient temperature on history of fuel percentage burn.

process, and eventually increases the maximum temperature inside the tank as shown in Fig. 9. This explains the increase in the maximum tank pressure due to higher ambient temperature. The marked effect of the ambient temperature on the burn rate that is shown in Fig. 10 explains the effect of ambient temperature on the maximum pressure rise-rate. The figure shows that the present solid propellant burns faster at higher ambient conditions. Consequently, the mass flow rate of the product-gases into the tank increases and results in a faster rise in the tank pressure.

5. Conclusions

In the present work, a pyrotechnic solid propellant gas generator has been analyzed. The current results presented are intended to show the thermal characteristics of a generic design of an airbag inflator in a tank test. For the current operating and design conditions, the following conclusion are drawn:

1. The heat loss to the ambient is negligible.
2. The tank pressure history is sensitive to heat transfer to the tank wall. This makes it necessary to incorporate accurate heat transfer modeling for heat transfer to the hardware elements of airbag system.
3. The tank test results should not be applied directly to auto-airbags because the significant difference in heat transfer between the hot gases and the tank wall on the one hand, and the hot gases and the airbag, on the other, affect the tank pressure history.
4. It has been concluded that the thermal performance of the system under consideration can be significantly affected by the ambient temperature. If the ambient temperature rises from 230 to 320 K, the tank pressure

impulse increases by 50 %, the combustion time decreases by 35 %, the maximum tank pressure increases by 20 %, and the maximum tank temperature increases by 27 %.

References

- [1] Sutton G P. Rocket propulsion elements. 6th Edition. John Wiley and Sons; 1992.
- [2] P.B. Butler, J. Kang, H. Krier, "Modeling and numerical simulation of the internal thermochemistry of an automotive airbag inflator". *Progress in Energy and Combustion Science*, Vol. 19, 1993, 365-382.
- [3] T.H. Vos, G.W. Goetz, "Inflatable restraint systems: Helping save lives on the road". *TRW Space and Defense Quest*, Winter Issue, 1989.
- [4] J.M. Berger, P.B. Butler, "Equilibrium analysis of three classes of automotive airbag inflator propellants". *Combustion Science and Technology*, Vol. 104, No. 1-3, 1995, 93-114.
- [5] A. Ulas, G.A. Risha, K.K. Kuo, "Ballistic properties and burning behavior of an ammonium Perchlorate/Guanidine Nitrate/Sodium Nitrate airbag solid propellant". *Fuel*, Vol. 85, 2006, 1979-1986.
- [6] J.J. Freesmeier, P.B. Butler, P. Barry, "Analysis of a hybrid dual-combustion-chamber solid-propellant gas generator". *Journal of Propulsion and Power*, Vol. 15, No. 2, March-April, 1999.
- [7] W. Sinz, S. Hermann, "The development of a 3D-navier-stokes code for the simulation of an airbag inflation". *Simulation Modeling Practice and Theory*, Vol. 16, 2008, 885-899.
- [8] Butler P B, Krier H. *Airbag Inflator Model User's Guide*. Champaign: Combustion Sciences Inc.; 1997.
- [9] R.G. Schmitt, P.B. Butler, J.J. Freesmeier, "Performance and CO Production of a Non-Azide airbag propellant in a pre-pressurized gas generator". *Combustion Science and Technology*, Vol. 122, 1997, p. 306.
- [10] Chase M W, Davies C A, Downey J R, Frurip D J, McDonald R A, Syverud A N. *JANAF thermochemical tables*. 3rd Edition. American Chemical Society; 1985.
- [11] Cruise D R. *Theoretical computations of equilibrium compositions, thermodynamic properties, and performance characteristics of propellant systems, PEP equilibrium code*. NWC Technical Report, NWC TP 6037; 1973.
- [12] K.K. Kuo, M. Summerfield, "Fundamentals of solid-propellant combustion (*Progress in Astronautics and Aeronautics*)". AIAA, Vol. 90, 1984, 622-623.
- [13] Zucrow M J, Hoffman J D. *Gas Dynamics*. Vol. 1. John Wiley and Sons; 1976.
- [14] Kee R J, Miller J A, Jefferson T H. *CHEMKIN: A general-purpose, problem-independent, transportable, FORTRAN chemical kinetics code package*. Sandia National Laboratories, SAND 80-8003, Livermore, CA; 1980.
- [15] Hindmarsh A C. *LSODE Software*. Lawrence Livermore National Laboratories, Livermore, CA; 1980.

The Effect of Fatigue on Crack Propagation in Flat Plates under Buckling Bending and Shear

Fathi A. Al-Shamma*

Mechanical Engineering Department, College of Engineering, University of Baghdad, Baghdad, Iraq

Abstract

Many works have been carried out to determine expressions for critical loads of crack propagation in flat plates under elementary load cases of shear, compression, bending and combination of theme. In this new solution, the analytical work must take into consideration the effect of fluctuating the buckling load for panels under various types of bending and shear loading. The effect of combined buckling shear and bending stresses on the crack propagation has been considered in this research. The analytical solution is based on a combination of maximum strain under mixed mode, Paris and Sih equation with Forman et al. equation. Different boundary conditions must be included in the flat plates, and new stress intensity factors for combined modes I and II have been developed for the crack growth. Also the results show the effect of crack length on the stress distribution and the direction of crack propagation.

© 2009 Jordan Journal of Mechanical and Industrial Engineering. All rights reserved

Keywords: Buckling Bending; Shear; Crack Propagation Fatigue; Stress Intensity Factors (KI, KII).

1. Introduction

In structures formed from thin sheets of material, there is an additional possible mode of instability known as local buckling. When a thin rectangular sheet is subjected to loads which can potentially cause failure by buckling, these loads comprise combinations of compression, shear and bending forces. Generic to all of these cases is the existence of stress gradients across the shells.

Previous researchers have carried out work mainly based on the use of energy methods such as the Raleigh – Ritz method [1], to determine theoretical buckling loads for panels under pure shear, compression, and combinations of these. These cases are summarized in design guides such as those by young [2], Timoshenko and Gere [3] and Bruhn [4]. However, this work is fairly limited in that it assumes a constant stress distribution and only very simple boundary conditions such as four edges simply supported, or four edges clamped have been considered.

Featherstone [5] outlines a programmed work that has been under taken to compare collapse loads predicted by theoretical, experimental, and finite element. Analysis predicted collapse loads for the case of a flat rectangular plate under combined shear and bending.

A great deal of research has been devoted to a study of the mechanism of fatigue, and yet there is still not a complete understanding of the phenomenon and the effect of fatigue loading on the crack propagation under complex stress of boundary conditions. Knowledge of the initiation

site and subsequent growth path of a fatigue crack greatly assists in determining the mode of failure and severity of its consequences. In addition, knowledge of the stress intensity factors at the various stages of growth is used to ascertain the service life of such components. (Nurse and patten son) [6]. D.R.Tadjiev et al. [7] studied the fatigue crack growth prediction under random loading in specimens of high strength aluminum alloy using modified root mean square (RMS) model for each specimen to determine the max. And min stresses under constant amplitude loading, R.Doglione and M. Bartolone [8] studied the fatigue crack propagation in a 2195-T8 alloy plate. They showed that fatigue resistance of this alloy is comparable to that of the classical competitor alloys and high lights stress ratio effects on the behavior at the threshold which causes the stress intensity range (ΔK_{th}) decrease as R increases . Yongming Liu et al. [9] developed a new mixed mode threshold stress intensity factor using a critical plane based multiaxial fatigue theory and the Kitagawa diagram. The proposed method is a nominal approach since the fatigue damage is evaluated using remote stresses acting on the cracked component rather than stresses near the crack tip.

An alternative method for determining the fluctuating of buckling load and its effect on the crack propagation in thin shells under complex load cases by using combined methods of max strain and max stress was done in this research. This has the advantage of allowing more difficult boundary conditions to be modeled, and loads to be applied as they exist in situ, thereby recreating varying stresses fields within the panel. This paper calculates the buckling loads for plates of four aspect ratios with different crack of lengths.

* Corresponding author. Fathi_alshamma@yahoo.com.

2. Theory

2.1. Fracture Mechanics for Fatigue

Fracture mechanics can only be applicable to fatigue after the crack initiation phase to enable crack growth to be predicted. As stated earlier fatigue failure is generally considered to be a three – stage process:

2.1.1. Stage I The Initiation of a Crack

There is some doubt as to where this occurs, and the processes of nucleation and stage 1 growth are not fully understood.

Using electron microscopically techniques for observing extrusions and intrusions from well defined slip bands [10] and have been proposed a theory of cross slip or slip on alternate slip planes and initially the cracks will be formed [11]. These cracks are likely to be aligned with the direction of maximum shear within the component i.e. at 45 to the maximum principle stress. Hence nominally, the position of maximum tangential stress has been used; and assumes that surface flaws are homogeneously distributed and will form from the site of a crack initiation. This method has been used taking into consideration the effect of friction on the crack propagation [21].

2.1.2. Stage II Crack Propagation

After initiation, crack propagation occurs as stage II growth according to [10]. Description of fatigue crack growth which attempts to include stage 1 and 2 growth in the determination of crack path would necessitate knowledge of the transition between stage 1 and 2 growth. Stage 1 growth occurs immediately which often grow with a strong shear component. Most cracks move to stage 2 growths with increasing crack length, which is characterized by macroscopic effects with crack is characterized by macroscopic effects with crack growth dominated by mode I displacements.

2.1.3. Stage III Crack Acceleration

When the crack has grown so that the critical stress intensity factor K_{Ic} is approached, the crack accelerates more rapidly with non linear relation until K_{Ic} is exceeded, and a final catastrophic failure occurs. This is related to the amplitude of the stress intensity factor Δk during the cycle which increases in this stage.

3. Crack Growth Laws

For many materials stage II, growth is described by the Paris-Erdogan law which is:-

$$\frac{da}{dN} = c(\Delta k)^m$$

Where c and m material coefficients (m lies between 2 and 7)

This simple relationship can be used to predict life time of component if the stress amplitude is constant. However, when stress amplitude varies, then the growth rate may depart markedly from the simple relation, and then Forman equation could be used, which also describe stage III.

The propagation of the crack in stage 2 has been predicted in this study assuming brittle failure. It has been shown that stress and strain methods are more reliable than those based on strain energy criteria. This is especially true when there is a mixed mode crack [12].

Added to this, the stress and strain based methods, found in ASTM standard E647 – 939 [20] have more readily understood physical basis, which essentially states that failure will occur in the direction perpendicular to the largest stress or strain.

In this study, the method used for determining the direction of crack growth by using maximum principle strain which comes from mixing two modes, I and II, by applying fluctuating buckling stress. The method adopted was based also on the maximum circumferential stress and its direction with the crack propagation. The values of the ratio K_{II} to K_I was predicted and was improved by satisfying these values, mathematical approach in [13]. From these ratios of K_{II} / K_I , we can find ΔK , and then using them to find the crack growth rate in the expression of formans under mixed bending and torsion stresses.

4. Theoretical Analysis

For a plate with simply supported edges and the crack propagate by two modes I and II because the buckling of rectangular plates with mixed boundary conditions under combination of bending and shear as shown in fig 1(a-b) could be Equivalent to state two conditions:

4.1. Shear

The problem of shear buckling for long strips and plates has been studied by many works. Some workers [14] used Donnell's equations to investigate the buckling of long plates under shear with both simply supported and clamped edges for the whole curvature range. This work has shown that the critical stress of a panel in shear buckling can be written as:

$$\tau_{cr} = \frac{K_s \cdot \pi^2 \cdot E}{12 (1 - \mu^2)} \left(\frac{t}{b}\right)^2$$

Where

a = length of longer side of plate

E =young's modulus

b =length of shorter side of plate

K_s =shear buckling stress parameter

t = thickness of plate

μ =Poisson's ratio.

K_s varies according to the boundary condition and aspect ratio. It has been looked at the case of a rectangular plate with one edge clamped using a Fourier series to represent the deflection of the plate in the energy equations [15]. Values of K_s are shown in table (1).

4.2. Bending

To solve the problem of a rectangular plate with simply supported edges, it has been used the principle of conservation of energy and a deflection in the form of a double trigonometric function [3]. For pure bending, the critical load can be calculated by the formula:

$$\sigma_{cr} = \frac{K_b \cdot \pi^2 \cdot E}{12 (1 - \mu^2)} \left(\frac{t}{b}\right)^2$$

Where

Kb= bending buckling stress parameter.

Kb varies according to the boundary condition and aspect ratio values of Kb are shown in table (2)

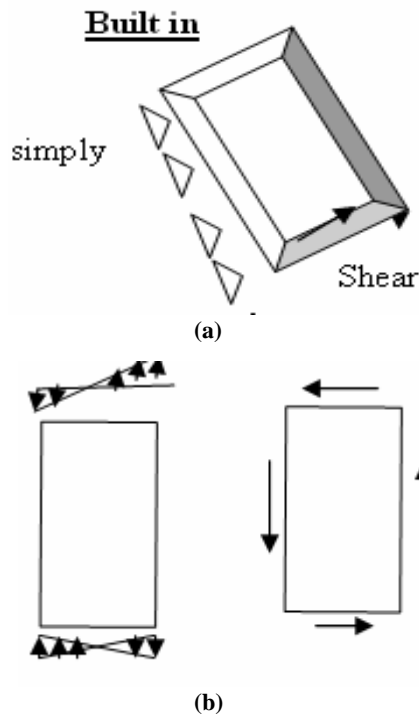


Figure 1(a),(b). Applied stress distribution on the edges of the plate.

Table 1. values of Ks for rectangular plate with one edge clamped

a/b	2.5	2	1.5	1.25	1.11	1.0
Ks	7.96	6.72	7.59	8.57	9.66	10.98

Table 2. values of Kb for rectangular plate with simply supported

a/b	0.6	0.75	0.8	0.9	1	1.5	2.	2.5
Kb	2.41	2.42	2.44	2.56	2.56	2.41	2.39	2.38

5. Equations for the Relation of Fatigue Buckling and Crack Propagation:

The relation between fatigue buckling and crack propagation can be divided to three groups:

1) For the displacement of the crack Propagation in the x-direction:

$$u = u_{model} + U_{modell} = u_I + u_{II} \tag{1}$$

$$\therefore \frac{\partial u}{\partial x} = \frac{\partial u_I}{\partial x} + \frac{\partial u_{II}}{\partial x}$$

$$\therefore \epsilon_x = \epsilon_{xI} + \epsilon_{xII} \tag{2}$$

For plane stress, Hooke's law applied as:

$$E \epsilon_x = \sigma_x - \nu (\sigma_y) \tag{3}$$

for mode I :

$$\left. \begin{aligned} \sigma_x &= \frac{K_I}{\sqrt{2\pi r}} \cos \frac{\theta}{2} (1 - \sin \frac{\theta}{2} \sin \frac{3\theta}{2}) \\ \sigma_y &= \frac{K_I}{\sqrt{2\pi r}} \cos \frac{\theta}{2} (1 + \sin \frac{\theta}{2} \sin \frac{3\theta}{2}) \\ \tau_{xy} &= \frac{KI}{\sqrt{2\pi r}} \sin \frac{\theta}{2} \cos \frac{\theta}{2} \cos \frac{3\theta}{2} \end{aligned} \right\} \tag{4}$$

substituted(4)in(3):

$$E \epsilon_{xI} = \frac{K_I}{\sqrt{2\pi r}} \cos \frac{\theta}{2} (1 - \sin \frac{\theta}{2} \sin \frac{3\theta}{2}) - \nu (\frac{K_I}{\sqrt{2\pi r}} \cos \frac{\theta}{2} (1 + \sin \frac{\theta}{2} \sin \frac{3\theta}{2})) \tag{5}$$

For mode II :

$$\left. \begin{aligned} \sigma_x &= \frac{-K_{II}}{\sqrt{2\pi r}} \sin \frac{\theta}{2} (2 + \cos \frac{\theta}{2} \cos \frac{3\theta}{2}) \\ \sigma_y &= \frac{K_{II}}{\sqrt{2\pi r}} \sin \frac{\theta}{2} (\cos \frac{\theta}{2} \cos \frac{3\theta}{2}) \\ \tau_{xy} &= \frac{K_{II}}{\sqrt{2\pi r}} \cos \frac{\theta}{2} (1 - \sin \frac{\theta}{2} \sin \frac{3\theta}{2}) \end{aligned} \right\} \tag{6}$$

Substitute eq(6) in eq(4) :-

$$E \epsilon_{xII} = \frac{-K_{II}}{\sqrt{2\pi r}} \sin \frac{\theta}{2} (2 + \cos \frac{\theta}{2} \cos \frac{3\theta}{2}) - \nu (\frac{K_{II}}{\sqrt{2\pi r}} \sin \frac{\theta}{2} (\cos \frac{\theta}{2} \cos \frac{3\theta}{2})) \tag{7}$$

From eq 2 we could obtain:

$$\begin{aligned} \epsilon_x &= \frac{1}{E} (\frac{KI}{\sqrt{2\pi r}} \cos \frac{\theta}{2} (1 - \sin \frac{\theta}{2} \sin \frac{3\theta}{2}) - \nu (\frac{KI}{\sqrt{2\pi r}} \cos \frac{\theta}{2} (1 + \sin \frac{\theta}{2} \sin \frac{3\theta}{2}))) \\ &+ \frac{1}{E} (\frac{-K_{II}}{\sqrt{2\pi r}} \sin \frac{\theta}{2} (2 + \cos \frac{\theta}{2} \cos \frac{3\theta}{2}) - \nu (\frac{K_{II}}{\sqrt{2\pi r}} \sin \frac{\theta}{2} (\cos \frac{\theta}{2} \cos \frac{3\theta}{2}))) \end{aligned} \tag{8}$$

For Combined mode I and II of the

$$\epsilon_x = \frac{1}{E} (\frac{K_I}{\sqrt{2\pi r}} \cos \frac{\theta}{2} (1 - \sin \frac{\theta}{2} \sin \frac{3\theta}{2}) - \nu (\frac{K_{II}}{\sqrt{2\pi r}} \cos \frac{\theta}{2} (1 + \sin \frac{\theta}{2} \sin \frac{3\theta}{2}))) \tag{9}$$

$$\gamma_{xy} = \frac{2(1+\nu)}{E} \tau_{xy} = \frac{2(1+\nu)}{E} (\frac{KI}{\sqrt{2\pi r}} \sin \frac{\theta}{2} \cos \frac{\theta}{2} \cos \frac{3\theta}{2} + \frac{K_{II}}{\sqrt{2\pi r}} \cos \frac{\theta}{2} (1 - \sin \frac{\theta}{2} \sin \frac{3\theta}{2})) \tag{10}$$

propagation of the crack it can be seen that mode II change the crack displacement in the x direction only, that is mean:

V=V_I where V is the displacement in the y direction

So that we could find in polar coordinate:

$$\epsilon_{\theta} = \frac{1}{2} (\epsilon_x + \epsilon_y) + \frac{1}{2} (\epsilon_x - \epsilon_y) \cos 2\theta + \frac{1}{2} \gamma_{xy} \sin 2\theta \tag{11}$$

By substituting eq 8, 9 and 10 in equation 11

$$\begin{aligned} &\nu (\frac{K_{II}}{\sqrt{2\pi r}} \sin \frac{\theta}{2} (\cos \frac{\theta}{2} \cos \frac{3\theta}{2})) + \frac{1}{2E} (\frac{KI}{\sqrt{2\pi r}} \cos \frac{\theta}{2} [1 - \sin \frac{\theta}{2} \sin \frac{3\theta}{2} - 1 - \sin \frac{\theta}{2} \sin \frac{3\theta}{2}]) \\ &- \nu (\frac{K_I}{\sqrt{2\pi r}} \cos \frac{\theta}{2} [1 + \sin \frac{\theta}{2} \sin \frac{3\theta}{2} - 1 + \sin \frac{\theta}{2} \sin \frac{3\theta}{2}]) + \frac{1}{2E} (\frac{K_{II}}{\sqrt{2\pi r}} \sin \frac{\theta}{2} (2 + \\ &\cos \frac{\theta}{2} \cos \frac{3\theta}{2}) - \nu (\frac{K_{II}}{\sqrt{2\pi r}} \sin \frac{\theta}{2} (\cos \frac{\theta}{2} \cos \frac{3\theta}{2}))) \cos 2\theta + \frac{1+\nu}{E} \sin 2\theta \\ &\epsilon_{\theta} = \frac{1}{2E} (\frac{K_I}{\sqrt{2\pi r}} \cos \frac{\theta}{2} [1 - \sin \frac{\theta}{2} \sin \frac{3\theta}{2}] - \nu (\frac{K_I}{\sqrt{2\pi r}} (\cos \frac{\theta}{2} [1 + \\ &\sin \frac{\theta}{2} \sin \frac{3\theta}{2} + 1 - \sin \frac{\theta}{2} \sin \frac{3\theta}{2}])) + \frac{1}{2E} (\frac{K_{II}}{\sqrt{2\pi r}} \sin \frac{\theta}{2} (2 + \cos \frac{\theta}{2} \cos \frac{3\theta}{2}) - \end{aligned}$$

$$\frac{k_I}{\sqrt{2\pi r}} \sin \frac{\theta}{2} \cos \frac{\theta}{2} \cos \frac{3\theta}{2} + \frac{k_{II}}{\sqrt{2\pi r}} \cos \frac{\theta}{2} \left(1 - \sin \frac{\theta}{2} \sin \frac{3\theta}{2} \right)$$

$$\therefore \epsilon_{\theta} = \frac{1}{2E} \left(\frac{2k_I}{\sqrt{2\pi r}} \cos \frac{\theta}{2} - \frac{\nu 2k_I}{\sqrt{2\pi r}} \cos \frac{\theta}{2} \right) + \frac{1}{2E} \left(-\frac{k_{II}}{\sqrt{2\pi r}} \sin \frac{\theta}{2} (2 + \cos \frac{\theta}{2} \cos \frac{3\theta}{2}) \right)$$

$$- \nu \left(\frac{k_{II}}{\sqrt{2\pi r}} \sin \frac{\theta}{2} (\cos \frac{\theta}{2} \cos \frac{3\theta}{2}) \right) + \frac{1}{2E} \left(\frac{k_I}{\sqrt{2\pi r}} \cos \frac{\theta}{2} (-2 \sin \frac{\theta}{2} \sin \frac{3\theta}{2}) \right)$$

$$- \frac{\nu k_I}{\sqrt{2\pi r}} \cos \frac{\theta}{2} [2 \sin \frac{\theta}{2} \sin \frac{3\theta}{2}] + \frac{1}{2E} \left(-\frac{k_{II}}{\sqrt{2\pi r}} \sin \frac{\theta}{2} (2 \cos \frac{\theta}{2} \cos \frac{3\theta}{2}) - \right.$$

$$\left. \nu \left(\frac{k_{II}}{\sqrt{2\pi r}} \sin \frac{\theta}{2} (\cos \frac{\theta}{2} \cos \frac{3\theta}{2}) \right) \right) \cos 2\theta + \frac{1+\nu}{E} \sin 2\theta \left[\frac{k_I}{\sqrt{2\pi r}} \sin \frac{\theta}{2} \cos \frac{\theta}{2} \right.$$

$$\left. \cos \frac{3\theta}{2} + \frac{k_{II}}{\sqrt{2\pi r}} \cos \frac{\theta}{2} (1 - \sin \frac{\theta}{2} \sin \frac{3\theta}{2}) \right] \dots \dots \dots (12)$$

Also we could find γ_{θ} as:

$$\frac{1}{2} \gamma_{\theta} = - \left[\frac{1}{2} (\epsilon_x - \epsilon_y) \sin 2\theta - \frac{1}{2} \gamma_{xy} \cos 2\theta \right]$$

$$= - \frac{1}{2} \left[\frac{1}{2E} \left(\frac{K_I}{\sqrt{2\pi r}} \cos \frac{\theta}{2} (-2 \sin \frac{\theta}{2} \sin \frac{3\theta}{2}) - \nu \frac{k_I}{\sqrt{2\pi r}} \cos \frac{\theta}{2} [2 \sin \frac{\theta}{2} \sin \frac{3\theta}{2}] \right) \right.$$

$$\left. + \frac{1}{2E} \left(-\frac{k_{II}}{\sqrt{2\pi r}} \sin \frac{\theta}{2} (2 \cos \frac{\theta}{2} \cos \frac{3\theta}{2}) - \nu \left(\frac{k_{II}}{\sqrt{2\pi r}} \sin \frac{\theta}{2} (\cos \frac{\theta}{2} \cos \frac{3\theta}{2}) \right) \right) \right]$$

$$\sin 2\theta - \frac{1+\nu}{E} \cos 2\theta \left[\frac{k_I}{\sqrt{2\pi r}} \sin \frac{\theta}{2} \cos \frac{\theta}{2} \cos \frac{3\theta}{2} + \frac{k_{II}}{\sqrt{2\pi r}} \cos \frac{\theta}{2} (1 - \sin \frac{\theta}{2} \sin \frac{3\theta}{2}) \right] \dots \dots \dots (13)$$

To find the maximum value of ϵ_{θ} , equation (12) is differentiated with respect to θ using math-Lab 2002 program for differentiating, and the derivative is equated to zero. The roots of this equation give values of θ at which max or min of the strain, which are the principal strains in the polar coordinates. The first root is found to be the maximum. The same roots substituted in equation (13) must be given a zero value of shear strain γ_{θ} .

These gives two set of equation which relates the ratio $\frac{k_{II}}{k_I}$ and θ for combined effect of mode II and I for crack propagation.

2- It could be related between mixed mode I – II loading involves axial loading in the y direction of a crack inclined as result of rotation about the z axis as shown in fig 2-a. Even in this instance, analytical method done by [16] shows that: -

$$KI = (\sigma \sin^2 \beta + n \sigma \cos^2 \beta) \sqrt{\pi a}$$

$$KII = (\sigma \cos^2 \beta + n \sigma \sin^2 \beta) \sqrt{\pi a} \quad (14)$$

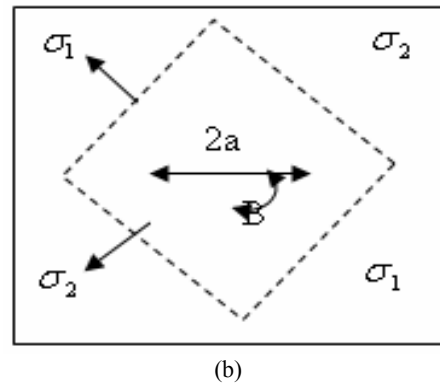
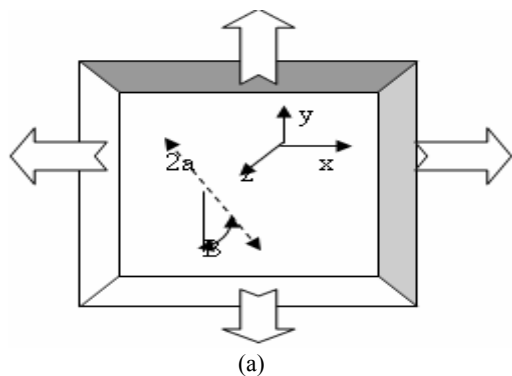


Figure 2. (a),(b).

Which could be done for very sharp and small crack?

Now by calculating the principle stresses from the condition shown in fig (2-a) and using Mohr's circle construction

$$\sigma_{1,2} = \frac{\sigma_x + \sigma_y}{2} \pm \sqrt{\left(\frac{\sigma_y - \sigma_x}{2} \right)^2 + \tau_{xy}^2} \quad (15)$$

Where $\sigma_y = 0$ and $\sigma_x =$ bending buckling stress

And $\tau_{xy} =$ shear buckling stress

By using the values of σ_1, σ_2 , the ratio of the stress intensity factories of mode I and II can be calculated from eq (14) as shown in fig (2-b):-

$$KI = (\sigma_1 \sin^2 \beta \pm \sigma_2 \cos^2 \beta) \sqrt{\pi a}$$

$$KII = (\sigma_1 \cos \beta \sin \beta \pm \sigma_2 \cos \beta \sin \beta) \sqrt{\pi a} \quad (16)$$

From group (1) and group (2) of the solution, relation between K_{II}/K_I can be obtained for crack propagation and the condition of external loading in which the stress intensity Factor depend on them. The plus minus in eq (16) depend on the value of σ_2 as compression or tension.

3):- In this group of solution, we used the fatigue equations of cycling loading by taking the fluctuating of buckling from tension to compression, so that the buckling bending stress will be change its direction, and from Mohers circle the principle stresses may be determined for the maximum and minimum limits of cyclic stresses, by taking the max principal stress in determining the max stress intensity factor as shown by [17].

$$K_{max} = y(\sigma_{1max} \sin^2 \beta + \sigma_{2max} \cos^2 \beta) \sqrt{\pi a} \dots (17 - a)$$

And for min. stress intensity factor

$$K_{min} = y(\sigma_{1min} \sin^2 \beta + \sigma_{2min} \cos^2 \beta) \sqrt{\pi a} \dots (17 - b)$$

Where y is a correction factor for finite plate and there values depend on the aspect ratio of the plate given in (16). Knowing that σ_{2min} have mines sign because it is compression, the relation expressing crack growth rates in terms of $\Delta K + K_c$ and a measure of K mean was proposed by [18] in the form:

$$\frac{da}{dN} = \frac{c \Delta k^n}{(1-R)K_c - \Delta K} \quad (18)$$

Where c, n=material constants

K_c = fracture toughness

$$R = \text{load ratio} \left(\frac{k_{min}}{k_{max}} \right)$$

$$\Delta k = k_{max} - k_{min}$$

6. Determination of Stress Intensity Factors

The determination of the mode I and II stress intensity factors was performed by solving eq (12) and eq (16) and is fitted to the mathematical approach of [13] in the form:

$$\frac{K_I}{K_{IC}} + \left(\frac{K_{II}}{k_{IIc}} \right)^2 = 1$$

The determination of the mode I and II stress intensity factors was performed by solving eq (12) and eq (16) and is fitted to the mathematical approach of [13] in the form:

Where

$$K_{IIc} = \sqrt{\frac{2}{3}} k_{Ic}$$

Using a Newton-Raphson iteration scheme, and then it is calculated approximately from the model dimensions and the loads applied.

This work is done for very small crack propagated in the direction of applying buckling load.

7. Results

For the case studies in this research, they taken are from aircraft standard specification duralumin _Bs3L100 Grade 2014 T₄ of rectangular plate with width b=100 mm and thickness t=0.55m for aspect ratio 1, 100 mm wide x 100 mm long. And aspect ratios 1.5, 2, 2.5 with crack length 2a=2, 4, 6,8,10 mm under fluctuation of compression and tension buckling stress, where the result gives the effect of this fluctuation on the stress intensity factor (Δk).

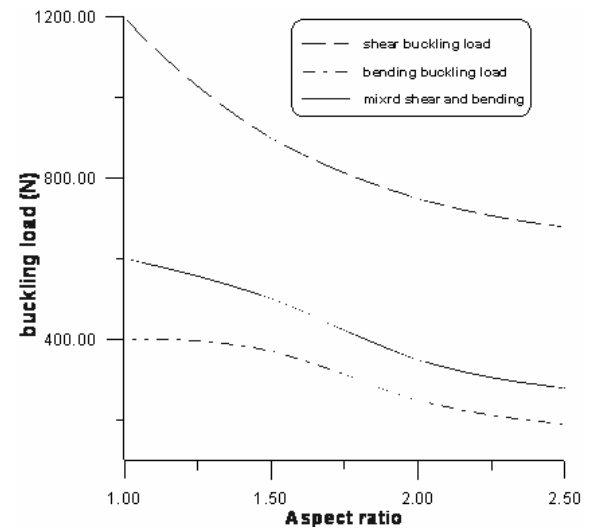


Figure 3. a comparison of theoretical buckling loads for varying boundary conditions.

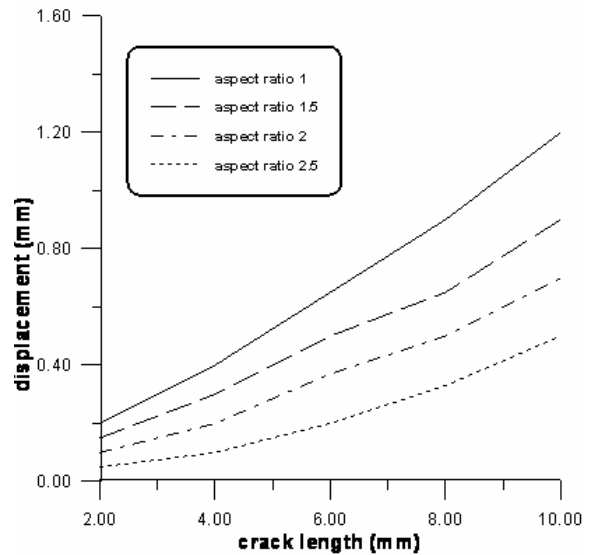


Figure 4. crack length versus u displacement for combined mode I and II from the crack tip.

In fig (3) the theoretical buckling load, for the case of pure shear only and pure bending only, mixed shear and bending stress with different aspect ratios.

It can be shown that shear stress have pronounced effect on the mixed shear and bending, but this effect will be decreased with increasing aspect ratio, so that it become nearer to the bending condition only. The value of bending stress is more pronounced on the crack propagation since in equations (14, 15, and 16). This stress is more effective on the value of K_I since they multiplied by $\cos^2 \theta$ rather

than KII which multiplied by $(\sin\theta \cos\theta)$ for very small values of θ .

From the strain method used in this study, the behavior of the displacement (u) in front of the crack tip with different crack length could be shown in fig(4). The behavior of the displacement will be decreased with increasing aspect ratio, and the rate of decreasing also increased with increasing the crack length. It can be shown also that with increasing the crack length for the same aspect ratio, the displacement will be increased, but the rate of increasing in the displacement are decreased with increasing aspect ratio.

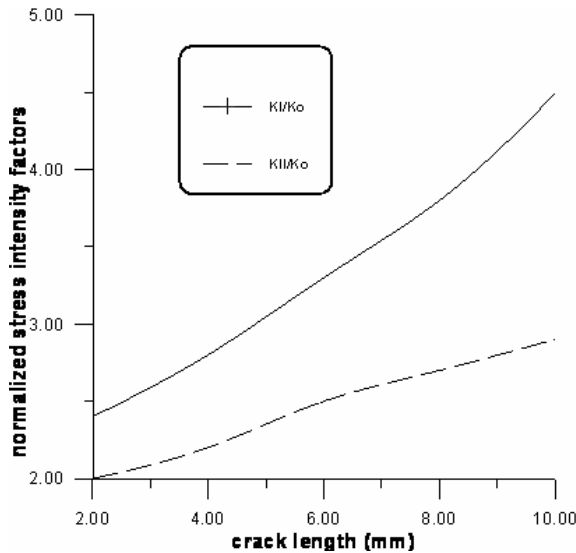


figure 5. Normalized Stress intensity factors as a function of crack length for aspect ratio 1.

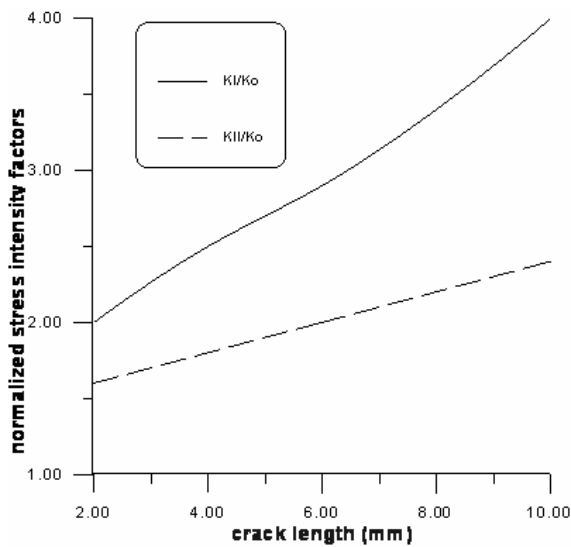


figure 6. normalized stress intensity factors as a function of crack length for aspect ratio 1.5.

In figures (5),(6),(7) , and (8), the data obtained from this process were the normalized stress intensity factors KI/K_0 and KII/K_0 , where $K_0 = \sigma_0 \sqrt{\pi a}$ and σ_0 is the applied or normal stress. For different crack length, the values of KI/K_0 and KII/K_0 will be increased with increasing crack length, but these values decreased with increasing aspect ratio. It is worthntoing that the values of KII have small values for aspect ratio of 2.5 which means

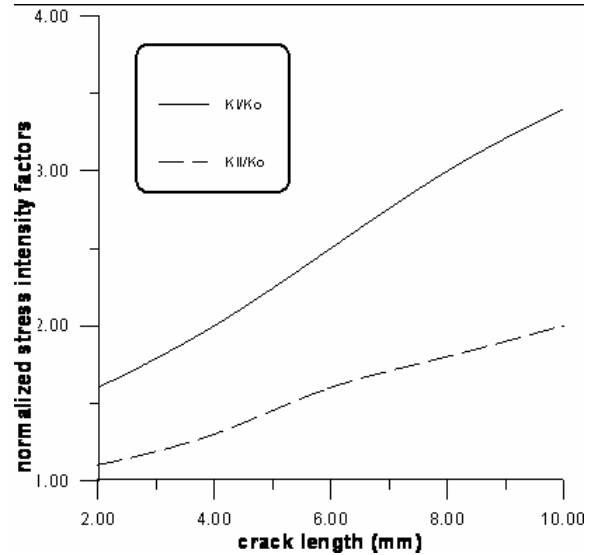


figure 7. normalized stress intensity factors as a function of crack length for aspect ratio 2.

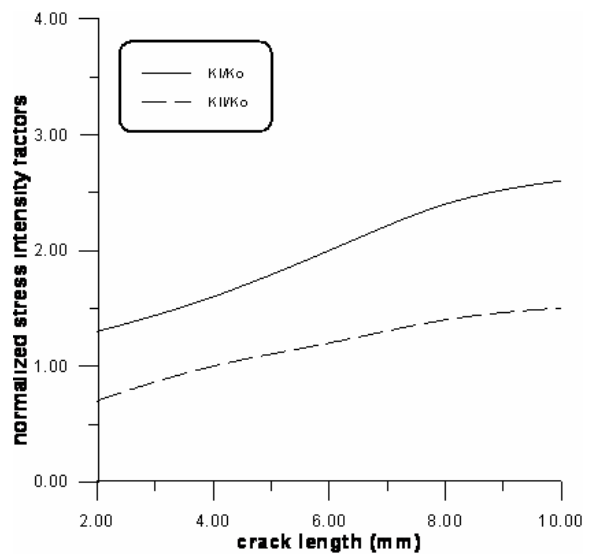


figure 8. normalized stress intensity factors as a function of crack length for aspect ratio 2.

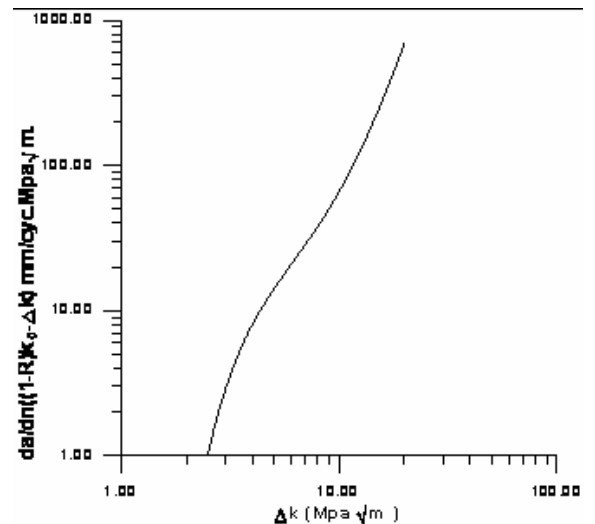


figure 9. fatigue crack propagation in aluminum plate with $(2a=2mm)$ showing the effect of Δk vs. da/dn .

that the mode I fracture is more effective than mode II fracture with increasing aspect ratio of the thin plate. The

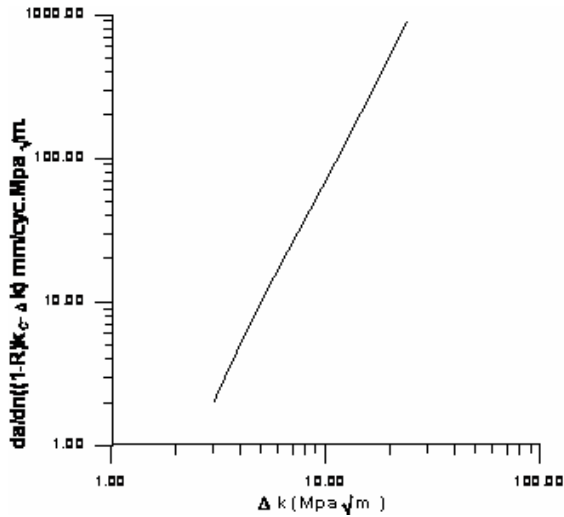


figure 10. fatigue crack propagation in aliminum plate with (2a=4mm) showing the effect of Δk vs. da/dn.

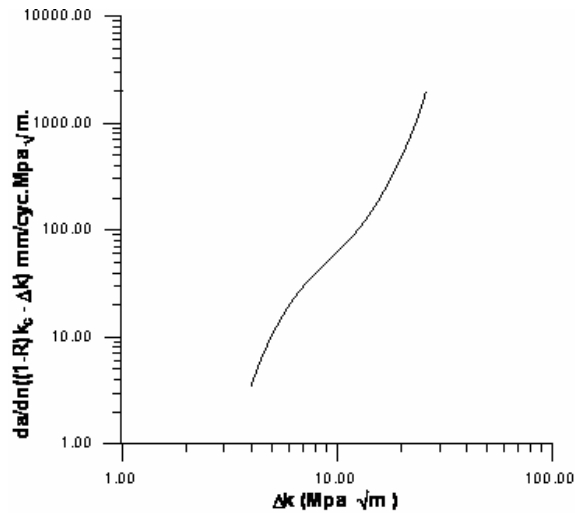


figure 11. fatigue crack propagation in aliminum plate with (2a=8mm) showing the effect of Δk vs. da/dn.

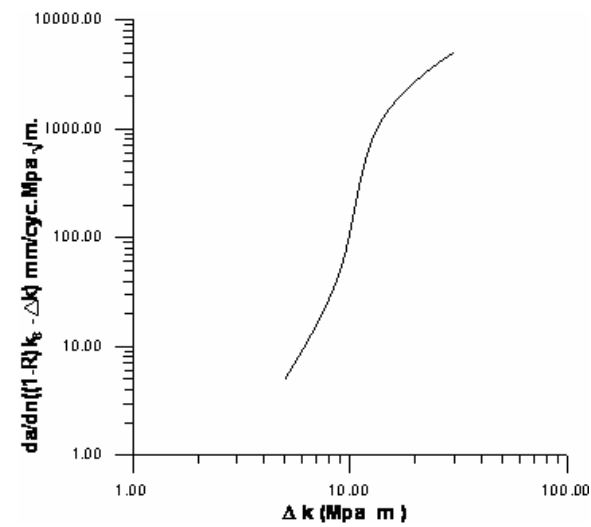


figure 12. fatigue crack propagation in aliminum plate with (2a=8mm) showing the effect of Δk vs. da/dn.

results show that the variation in the values of KI and KII depends not only on the values of the normal and shear stresses, but also on other factors like aspect ratio, and the

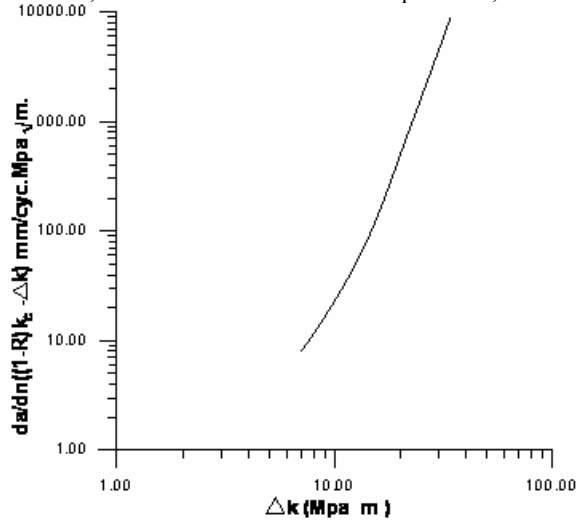
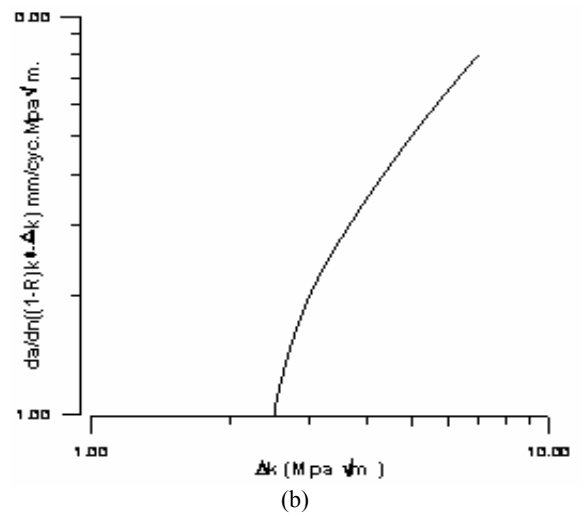
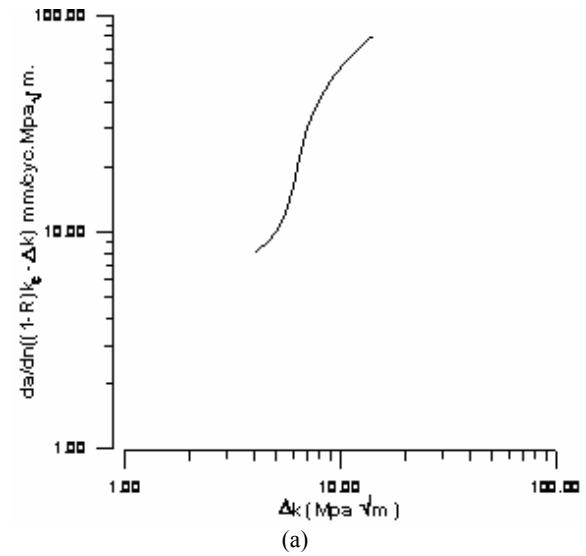


figure 13. fatigue crack propagation in aliminum plate with (2a=10mm) showing the effect of Δk vs. da/dn.



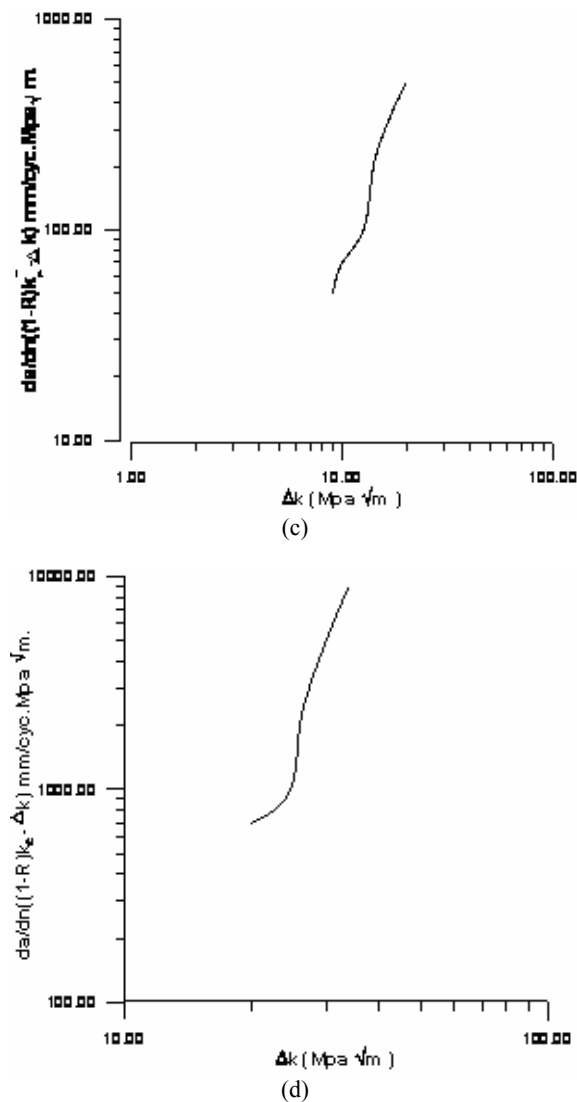


Figure 14. (a) fatigue crack in aluminum plate with aspect ratio = 1 showing the effect of Δk vs. da/dN , (b) fatigue crack in aluminum plate with aspect ratio = 1.5 showing the effect of Δk vs. da/dN , (c) fatigue crack in aluminum plate with aspect ratio = 2 showing the effect of Δk vs. da/dN , (d) fatigue crack in aluminum plate with aspect ratio = 2.5 showing the effect of Δk vs. da/dN .

ratio of crack length to the aspect ratio which is shown in these figures.

Calculating the fatigue crack propagation, by using Forman equation in four cases of aspect ratios (1, 1.5, 2, 2.5) which results in four points connected by spline fitting, gives good observation about the relation between Δk versus da/dN for cycling buckling loads for thin plates, figures (9, 10 and 11).

It can be seen the effect of increasing the crack length causes increasing in the value of Δk and increasing in the Forman cycling load

$$\left(\frac{da}{dN}\right) [(1-R)K_c - \Delta K] \text{ mm/cyc.Mpa } \sqrt{\text{m}}.$$

It can be seen that increasing the aspect ratio causes an increase in the $\frac{da}{dN}$ but the rate of increasing will be decreased when we transfer from aspect ratio 2 to 2.5, and this is because the effect of stress ratio will be more effective than the change in Δk on the value of da/dN . Also from figures (12) and (13) increase the crack length

and increasing the aspect ratio to values 2 and 2.5 cause very high values of da/dN which are corresponding to the effect of increasing of mode I (KI) and decreasing in the mode II (KII) in these boundary condition.

It could be shown from figures (14-a, b, c, d) that the variation of aspect ratio for crack lengths ($2a=2,4,6,8,10$ mm) causes nonlinearity in the behavior of Δk versus $(da/dN) [(1-R)K_c - \Delta k] \text{ mm/cyc.Mpa } \sqrt{\text{m}}$, and the rate of increasing will not be changed uniformly because the effect of combined mode I and II and the complexity of the fluctuating of buckling loads and its effect on the fatigue crack growth for high aspect ratio.

8. Conclusions

It has been shown that the method developed for restricting crack paths using combined maximum principle strain and maximum principle stress give good results when compared with experimental results that have been obtained previously by some researchers for thin plate with small crack initiation [19]. Then this method has been used for predicting the crack growth for many aspect ratio and its effect on the values of cycling loading da/dN . The results show that increasing aspect ratio and crack length causes very high values of da/dN and assist that the crack propagate under mode I rather than mode II. Also in this research it takes into consideration the variation of Δk with different aspect ratios for the same applied fluctuating stresses.

References

- [1] W. Ritz, "Journal für reine und angewandte Mathematik". Vol. 135(1), 1909, 1-61.
- [2] Young W C. Roarks formulas for stress and strain. London: McGraw-Hill; 1989.
- [3] Timoshenko S P, Gere J M. Theory of elastic instability. London: McGraw- Hill; 1961.
- [4] Bruhm E F. Analysis and design of flight vehicle structures. Indianapolis: Jacobs publishing Inc.; 1973.
- [5] C.A. Featherston, C. Ruiz, "Buckling of flat plates under bending and shear". Journal of Mechanical Engineering science, Vol. 212, 1998, 249-261.
- [6] A.D.Nurse, E.A.Patterson "Determination of predominantly mode I stress intensity factors from isochromatic data". Fatigue and fracture of Engng Mater. Structure, 16(12), 1993, 1339-1354
- [7] D.R.Tadjive, S.T.Ki, "fatigue crack growth prediction in 7475-T7351 Aluminum Alloy under Random loading using modified root mean square model", Yeungnam university, South Korea, 2003, 712-749.
- [8] R. Doglione, M. Bartolone, "Fatigue crack propagation in 2195-T8 Aluminum alloy plate". 9th International conference on Aluminium Alloys (ICAA9), Institute of materials Engineering Australasia, 2004, 616-621.
- [9] Y. Liu, S. Mahadevan, "Threshold stress intensity factor and crack growth rate prediction under mixed - mode loading". Engineering Fracture Mechanics, Vol. 74, 2006, 332-345.
- [10] P.J. Forsyth, "A two stage process of fatigue crack growth". In proceedings of the crack propagation symposium, canfield, Bedfordshire, 1961, 76-94.
- [11] A.H. Cottrell, "Theoretical aspects of radiation damage and brittle fracture in steel pressure vessels". Iron Steel Institute, Special Report No.69, 1961, 281-296.

- [12] S.K. Maiti, R.A.Smith, "Criteria of brittle fracture in biaxial tension". Engineering Fracture Mechanics , Vol. 19, No.5, 1984,739-804 .
- [13] Hellan K. Introduction to fracture mechanics. London: Mc Graw –Hill; 1985.
- [14] Batdorf S B. A simplified method of elastic stability analysis for thin cylindrical shells I- Donnell's equation. NACA TN 1341; 1947.
- [15] I.T. Cook, K.C. Rokey, "Shear buckling of rectangular plates with mixed boundary conditions". Aeronaut , 14 ,1963 .
- [16] P.C.Paris., G.C.sih ., ASTM STP 381, 1965, 30.
- [17] Hertzberg W R. Deformation and fracture mechanics of Engineering materials. John Wiley and Sons; 1996.
- [18] [18] R.G. Forman, V.E. Kearrey,R.M.Engle, J.Basic Engineering Trans .ASME89459 , 1967.
- [19] Ewalds H L, Wanhill R J. Fracture mechanics. Edward Arnold publication; 1989.
- [20] ASTM standard E647-93. 1993 Annual Book of ASTM Standards. Philadelphia, PA; 1993.
- [21] R.I. Burguete, E.A.Patterson,"The effect of friction on crack propagation in the dovetail fixings of compressed discs". J. Mechanical Eng. Science, Vol. 212, Part c, 1998, 171 .

Water Pumping System with PLC and Frequency Control

Akayleh Ali^{a,*}, Mohammed Al_Soud^b, Essam Abdallah^b, Salah Addallah^c

^aDepartment of Electrical Engineering, Tafila Technical University, Tafila, Jordan

^bDepartment of Mechanical Engineering, Al-Balqa Applied University, Amman, Jordan

^cDepartment of Mechanical and Industrial Engineering, Applied Science University, Amman, Jordan

Abstract

In this study controlled water pumping system is designed, constructed, and modeled. The programming method of control of pumping flow rate is achieved by means of integrated programmable logic controller (PLC) and frequency inverter (FI). PLC main function is to determine the required flow rate levels and the related time intervals of the flow rate hold time. (FI) is used to control the dynamic change of temperature between various operating points. The designed system shows the capability for full control of pumping flow rate from zero to maximum for any required range of time in case of increasing or decreasing the pumping flow rate. All variables of the system will be changed gradually until reaching their needed working points. The mathematical model of water pumping system with PLC and frequency control is built based on MATLAB-SIMULINK. A test rig built and an experimental study was performed. From the analysis of the experimental starting dynamic characteristics of water pumping system and modeled characteristics, it was noticed that they are very similar.

© 2009 Jordan Journal of Mechanical and Industrial Engineering. All rights reserved

Keywords: PLC; Frequency Control; Water Pumping System; Dynamic Characteristics.

1. Introduction

Pumping equipments in the modern manufacturing systems may be used as main parts in many industrial activities, like chemical industries, food industries, etc. The automation of the pumping processes in those industries will certainly lead to improve their performance [1]. In Jordan about 18% of generated electrical power is consumed by three-phase-induction motors driven centrifugal pump in water pumping stations. From the analysis of the working conditions of water pumping systems, it is noticed that there are many problems, which face the work of such systems, as hydraulic hammers, dynamic stresses in mechanical parts, high starting currents in the three-phase-motor driven centrifugal pump, and energy saving problems [2].

A new single-switch parallel resonant converter for induction heating was introduced in [3]. The circuit consists of an input LC-filter, a bridge rectifier, and only one controlled power switch. The switch operates in a soft communication mode and serves as a high frequency generator. A voltage-fed resonant LCL inverter with phase shift control was presented in [4]. It was observed that the control strategy offered advantages in the megahertz operating region, where a constant switching frequency is required. The inverter steady state operation is analyzed using fundamental frequency analyses. A cost-effective high efficiency inverter with phase-shifted pulse

modulation scheme was proposed for medium power (5-30) kW induction heating applications is discussed in [5]. The proposed inverter accomplishes soft switching operation over a wide power regulation range. The actual power conversion efficiency reached was 96.7%.

A control method of reducing the size of the dc-link capacitors of a converter-inverter system was presented in [6]. The main idea is to utilize the inverter operation status in the current control of the converter. This control strategy is effective in regulating the dc-voltage level. Even the dc-link capacitor is arbitrarily small and the load varies abruptly. In [7], a method was proposed to accurately predict the minimum required temperature recovery, considering repeatability and accuracy of the leak detector by investigating the relation between temperature recovery time and applied pressures using PLC system. A methodology was demonstrated to design a PLC program that organizes the relation between the physical inputs and outputs of the pumping tools in manufacturing systems.

In [8], an experimental study was performed to investigate the effect of using two axes tracking with PLC control on the solar energy collected. The two axes tracking surface showed better performance with an increase in the collected energy up to 41% compared to the fixed surface. This study seeks to design, model, and experiment of fully automated water pumping system with PLC and frequency control, where the main PLC function is to control the required flow rate levels and the related time intervals of the pumping flow rate hold time. FI is

* Corresponding author. akayleh_em@yahoo.com.

used to control the dynamic change of pumping flow rate between various operating points.

2. Water Pumping System Design and Control

For the purpose of experimentation, the electromechanical system PLC-FI-Three phase induction motor-centrifugal pump pipeline was designed and constructed as shown in figure 1.

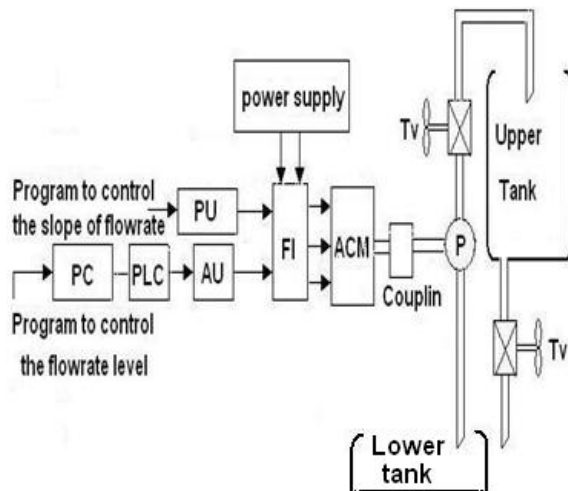


Figure 1. Water pumping system with PLC and frequency control.

Both the design of PLC and frequency controlled pumping system were performed, using an open loop and programming method of control in which stored instructions in memory of PLC was used to control the pumping flow rate. PC is a personal computer which is used to write the control program; then download it to the PLC through communication cable. The PLC is S7-200 type, which has 12 inputs, 8 outputs and 220 VAC supply voltage [9]. The PLC main function is to instruct the analog unit to go on or off and to state the required percentage output and the related hold time intervals. The analog unit function is to transfer the digital output value at the output of PLC into analog value, which ranges from zero to 10 VDC at the output of the analog unit. In the control program, different percentages of output voltage are supplied to the AC motor driven centrifugal pump by the frequency inverter, which is originally stated by the analog unit output, where 0 VDC equals 0% at the output of the frequency inverter and 10 VDC equals 100% at the output of frequency inverter.

FI is a one-phase input, three-phase output with a rated power of 0.95 KVA and a rated output current of 2.5A. ACM is a three -phase induction motor with a rated power of 0.37Kw at 50 Hz, and with a voltage of 240V and current of 1.8A for Δ connection [10]. P is a centrifugal pump which has the following data: flow rate 10-30 L/min, head 14-22m and nominal impeller speed 2900 rpm. P connects the upper and lower tanks with 0.5 inch steel pipes to provide an unlimited water supply for the system. TV is a throttling value which could be used for varying the flow rate manually. A venture meter was used to measure water flow rate, and a stop watch was used to measure the time. The rotational speed of the pump impeller was calculated using the following proportionality equation:

$$Q_a/Q_r = n_a/nr \quad (1)$$

Where:

Q_a : The actual flow rate of water.

Q_r : The rated flow rate of water.

n_a : The actual speed of motor.

nr : The rated speed of motor.

To investigate the system performance during starting towards different input signals, the frequency control laws which represent the frequency function of time, shown in Figure 2, were used. The control laws were started from the base frequency of 10 Hz through the starting time to reach reference frequency of 50 Hz. In case of direct connection to the supply network, the starting time equals zero as shown in curve 1 of figure 2, which represents step signal [11].

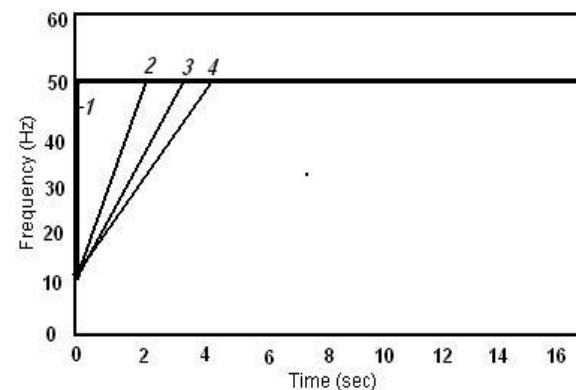


Figure 2. The programmed input frequency of time in case of starting

The curves 2, 3 and 4 in Figure 2, where obtained by using different ramp signals with starting time equal to 2 seconds, 3 seconds, and 4 seconds respectively. According to the different inserted control laws, the output flow rate of the water pumping system in starting condition change as a time function as shown in figure 3.

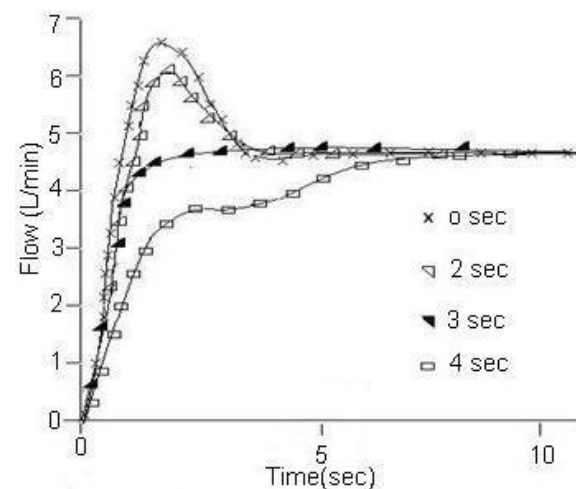


Figure 3. Flow rate vs. time according to the different inserted control laws

According to the different inserted control laws, the output pump speed of the water pumping system in starting condition changes as a function of time as shown in Figure 4.

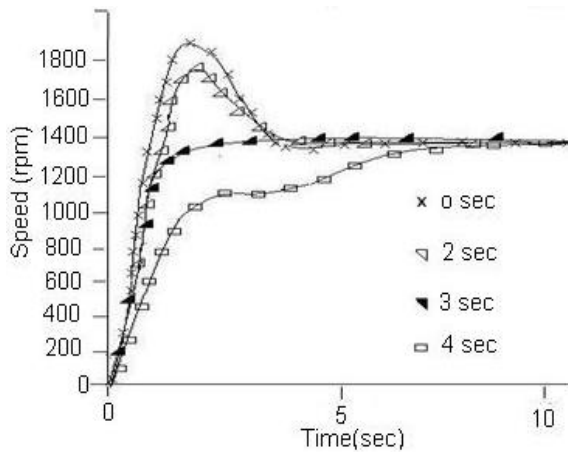


Figure 4. Speed vs. time according to the different inserted control laws.

From the analysis of starting curves in Figures 3 and 4, it can be noticed that in case of starting with step input signal, all output parameters of the water pumping system including speed and flow rate exhibited a high peak value with fluctuation until reaching the rated values. Considering other control laws, the range of vibrations decreased as time increased. Setting the starting time to 3 seconds exhibited very small oscillations that can be neglected. While setting the starting time to more than 3 seconds exhibit no oscillations [12, 13].

Figure 5 shows the variation of programmed frequency function of time. The control law was started from the base frequency of 0 Hz to reach 12.5 Hz with in 10 seconds, after that, the frequency will be stable for 15 seconds, then the frequency will be changed softly from 12.5 Hz to the 25 Hz through 10 seconds, later the frequency will be stable for 15 seconds, then the frequency will be changed softly from 25 Hz to 37.5 Hz through 10 seconds, after that the frequency will be stable for 15 seconds, later the frequency will be changed softly from 37.5 Hz to 50 Hz through 10 seconds, after that the frequency will be stable for 15 seconds, next the frequency will slow down softly to 25 Hz through 10 seconds, after that the frequency will be stable for 20 seconds, then the frequency will slow down softly from 25 Hz to 0 Hz through 10 seconds.

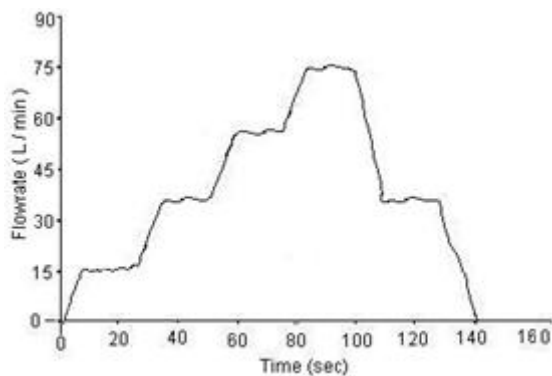


Figure 5. Input frequency vs. time

According to the control law, shown in Figure 5, the experimental output flow rate and experimental pump

speed of the water pumping system are shown in Figure 6 and figure 7.

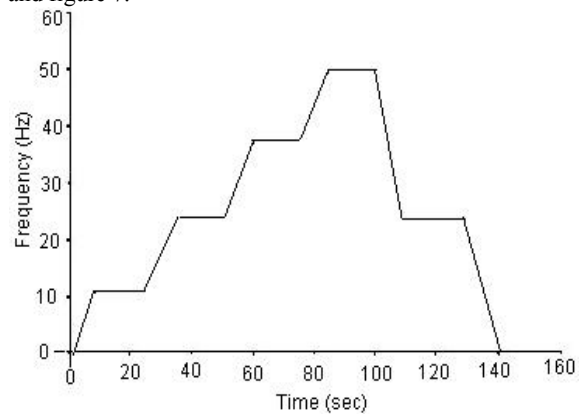


Figure 6. Flow rate vs. time.

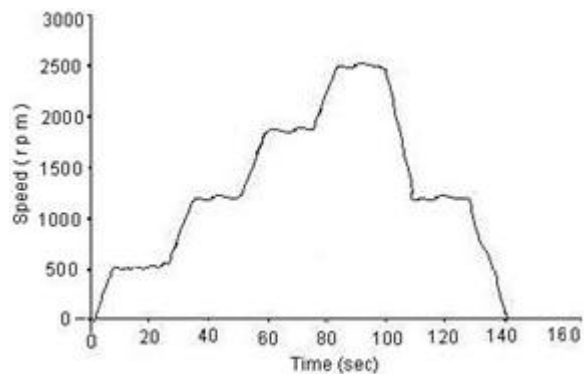


Figure 7. Pump speed vs. time.

Frequency inverter, according to the different incoming instructions of PLC through analog unit, operates the three-phase motor with the required percentage of voltage and frequency. Parameter unit is a type of programmer which is used to program the ramp up and ramp down time between each two controlled levels. So, frequency inverter has two types of commands:

1. Type of commands supplied by the PLC to the analog unit then to the frequency inverter to state the required level of flow rate and the hold time interval.
2. Type of commands supplied by parameter unit to control the ramp up and ramp down time to make a soft transition conditions between various operating levels.

It can be noticed from the curves in Figure 6 and Figure 7 that the experimented system shows the capability for full control of flow rate and pump speed from zero to maximum for any required range of time in case of increasing or decreasing the flow rate and pump speed. All variables of the system will be changed gradually until reaching their needed working points [14, 15].

3. Mathematical Model of the System

The mathematical model of water pumping system with PLC and frequency control will be done by using MATLAB-SIMULINK graphical interface Figure 8.

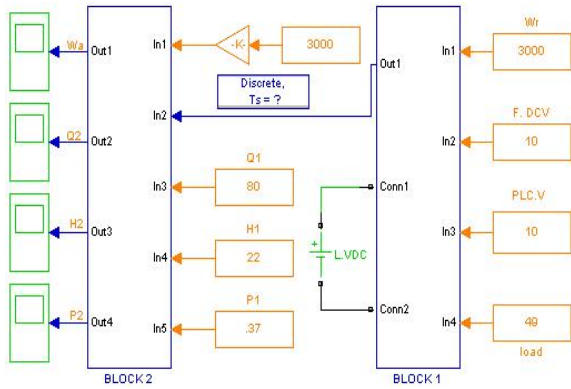


Figure 8. Mathematical model of water pumping system with PLC and frequency control.

The mathematical model consists of two blocks each of them has a specific function.

Block 1- The main function of this block is represent the vector control of a variable –frequency induction motor drive, which is available as a built using MATLAB library (see figure.9)[16]. In this block the main input signals are:

- Rated angular speed signal In 1
- Full value of dc controlled voltage signal In 2 ,this value is related of rated frequency of the system.
- PC or PLC voltage signal In 3
- Rated load torque signal In 4

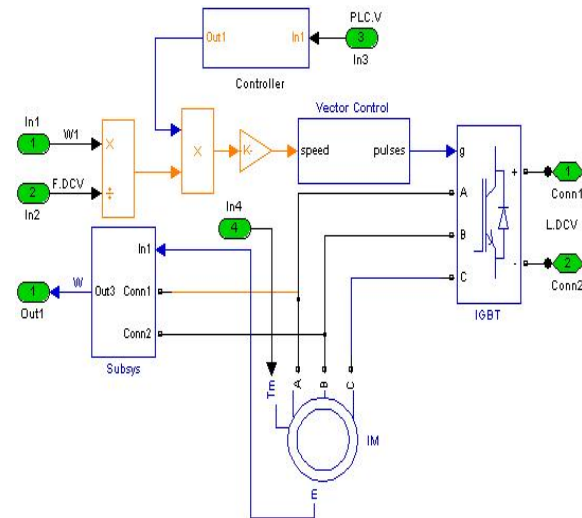


Figure 9. Vector control of a variable –frequency induction motor drive.

Block 2- This block contains the mathematical equations that are responsible for the main equations and relationships of pumping system calculation. The main inputs of this block are the rated of pump system parameters (Q_r, H_r, P_r) and the rated and actual speed values of the induction motor (n_r, n_a) (see figure.10).

Output values of this block diagram are presented as the main system response as follows:

$$Q_a / Q_r = n_a / n_r \tag{2}$$

$$H_a / H_r = (n_a / n_r)^2 \tag{3}$$

$$P_a / P_r = (n_a / n_r)^3 \tag{4}$$

Where:

H_a : The actual head of pump

H_r : The rated head of pump

P_a : The actual power consumption

P_r : The rated power consumption

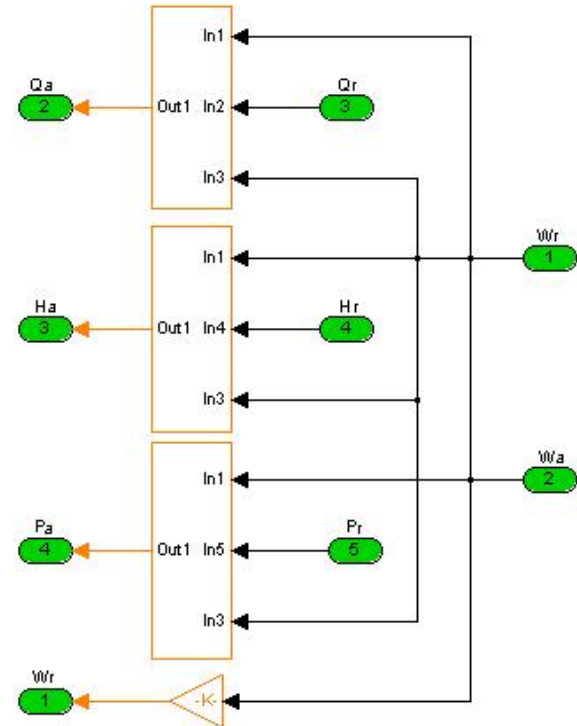


Figure 10. System main equations block.

Output values of this block diagram are presented as the main system response as follows:

$$Q_a / Q_r = n_a / n_r \tag{2}$$

$$H_a / H_r = (n_a / n_r)^2 \tag{3}$$

$$P_a / P_r = (n_a / n_r)^3 \tag{4}$$

Where:

H_a : The actual head of pump

H_r : The rated head of pump

P_a : The actual power consumption

P_r : The rated power consumption

4. System Operation and Test

According to the programmed control law shown in Figure 5 as a relationship between frequency and time, the modeled output flow rate and pump speed of water pumping system are shown in figure 11 and figure 12.

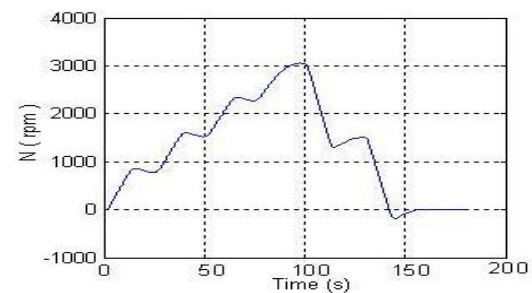


Figure 11. The modeled flow rate.

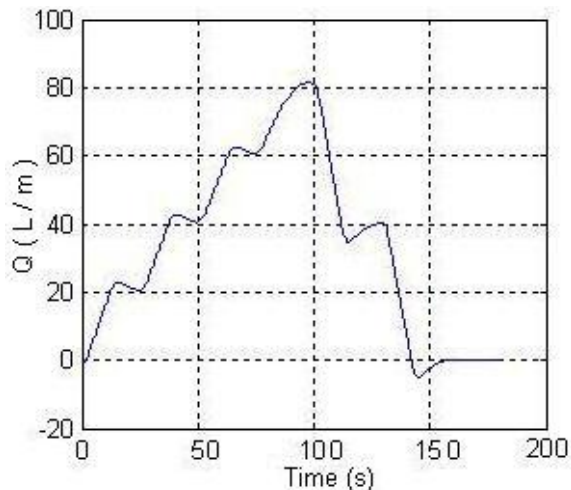


Figure 12. The modeled pump speed

It can be noticed from Figure 11 and Figure 12 that the flow rate and pump speed in modeled system showed the capability for full control from zero to maximum for any required range of time in case of increasing or decreasing.

5. Discussion and Results

PLC and frequency control of water pumping can be used in cases of dynamic conditions, for example starting, breaking, and changing from one operating condition to another. The using of PLC and frequency control of water pumping system will change all variables of the system gradually until reaching the desired operating condition. Consequently, it is possible to prevent hydraulic hummers and dynamic stresses in mechanical elements in water pumping system. Also it is possible to avoid dynamic currents in the three-phase AC machine. From the comparison of the experimental curves in Figure 6 and Figure 7, and the theoretical curves in Figure 10 and Figure 11, it is obvious that they are very similar. This means theoretical model can successfully represents the real behavior of water pumping system with PLC and frequency control.

6. Conclusions

In this work, small capacity water pumping system is designed, constructed and experimented by using PLC and frequency control. The designed system shows the capability for full control of flow rate from zero to maximum for any required range of time in case of increasing or decreasing the flow rate. It can be concluded from the experimentation of the water pumping system that all variables of the system would be changed

gradually until reaching their required operating points. The proposed mathematical model of the system successfully represents the real behavior of water pumping system with PLC and frequency control.

References

- [1] S. Abdallah, A. Abdulkarim, "Methodology to design an automated pump plants with PLC control system". Proceedings of the International engineering conference. Mutah-Jordan, 2004, 26-28 April, 373-398.
- [2] Abdallah S. "The regulation of starting and breaking dynamic characteristics in water pumping systems with open-loop control". In proceedings of the 8th Cairo University conference on mechanical design and production. Cairo, Egypt; January 2004,4-6.
- [3] Shenkman A. "Axelrod B. Berkovich Y. Improved modification of the single-switch AC-AC converter for induction heating applications". IEE, Proc-Electr Power Appl 2004, 151(1),1-4.
- [4] Mollov, S.V., Theodoridis, M. "Forsyth AJ. High frequency voltage-fed inverter with phase-shift control for induction heating". IEEE, 2003,12-8
- [5] Kifune, H., Hatanaka, Y., Nakaoka, M. "Cost effective phase shifted pulse modulation soft switching high frequency inverter for induction heating applications". IEE, Proc-Electr Power Appl ,2004, 151(1),19-25.
- [6] Jung, J., Lim, S., Nam, K. "A feedback linearizing control scheme for a PWM converter-inverter having a very small DC-Link capacitor". IEEE, Trans Ind Appl 1999, 35(5).
- [7] Harus, L.G., Cai, M., Kawahima, K., Kagawa, T. "Determination of temperature recovery time in differential-pressure-based air leak detector". Measurement Science and Technology 17(2006) 411-418.
- [8] Abdallah, S., Nijmeh, S. "Two axis sun tracking system with PLC control". Issued Energy conversion manage ,2004 ,45,193-199
- [9] Siemens PLC, s7-200, "operating instruction manual". Issued, 06/02.
- [10] [10] Siemens Sinamics, G110, "operating instruction manual". User documentation issued ,04/02.
- [11] M.Arkan, D. Kostic-Perovic and Unsworth P.J.2005, "Modelling and Simulation of Induction Motors with Inter-Turn Faults for Diagnostics," Electric Power Systems Research, vol. 75, N. 1, pp.57-66.
- [12] T.Kamalov , S. Abdallah, "The choose of economical law for frequency control of centrifugal pumps". Problems of power and automation, Russia, Vol 4, 1994.
- [13] R.William, E. Robert, "Retrofit of 22 pipe line pumping stations with 3000-HP motors and variable-frequency drives". IEEE, (34)/ 1,1998,178-186
- [14] L.Manz, "Applying adjustable-speed drives to three phase induction NEMA frame motors". IEEE, 1997,Vol. 33, No. 2.
- [15] H.Jung-IK, S. Seung-ki, "Sensor less field orientation control of an induction machine by high-frequency signal injection". 1999,Vol. 35, 1.
- [16] Palm, III. W. (2005). "Introduction to MATLAB 7 for Engineers".1999, McGRAW-HILL.

Plane Deformation of a Textile Material with Boundary Forces Using Finite Element Method

M. A. Nawafleh^{a,*}, N. Al-Kloub^b

^aDepartment of Civil Engineering, Al-Hussen Bin Talal University, Ma'an, Jordan

^bDepartment of Mechanical Engineering, Al-Balqa' Applied University, Amman, Jordan

Abstract

An approach is proposed to determine the stress-strain state of soft shells having rectangular shape. The finite element method is applied to investigate the plane problem of strains and stresses calculation. The model is based on assuming that the density of strain potential energy of the textile shell material is a function of the macroscopic strain measures of the soft shell. The results obtained from the calculations display that the internal boundary layers begin at the vertices of the aperture. The calculations show that progressive cracks are developed due to the destruction of filaments forming the fabric along the boundary layers. The calculations are characterised by zero approximation and exact estimates of the maximum values of stresses are determined.

© 2009 Jordan Journal of Mechanical and Industrial Engineering. All rights reserved

Keywords: Soft Shells; Stress; Strain; Finite Element; Zero Approximation; Boundary Layers.

1. Introduction

For the design and operation of textile industries [1, 2], studies are requested to investigate the stresses and strains resulted from the application of forces at the boundaries of a fabric having a rectangular form.

In order to calculate the actual strains of a fabric, a minimization of the energy functional are implemented which can be fulfilled by finite elements methods with a various choices of these elements [3, 4]. For each choice, this approach is based on the calculation of the nodal values of unknown functions as a solution of a system of non-linear algebraic equations [5, 6]. In this study, a reduction to a solution of Cauchy problem corresponding to some parameters which characterize the rigidity of the baric is used of the calculation of the actual strains. A zero value parameter relates to forces with negligible small elongations in the filaments of the fabric. By assuming a zero value of this parameter, the deformation of the fabric can be only resulting from the changing of angles between filaments. In the Cauchy problem approach, the initial conditions are taken as the deformations of the fabric at the zero value of the parameter. Different deformations of the fabric having a net structure with square meshes are obtained when such initial conditions are applied [7, 8]. By applying various boundary conditions, the fabric can be divided into zones with bi-axial or one-axial deflected mode, and these zones can be separated by concentration lines and disruption lines of the stresses. The elastic properties of the fabric are considered in the calculations

which is the most essential condition to the zero order solution, which are observed in the surrounding of the concentration lines and disruption lines. To determine the geometric characteristics of the finite elements, the knowledge of the properties of these lines is of great importance.

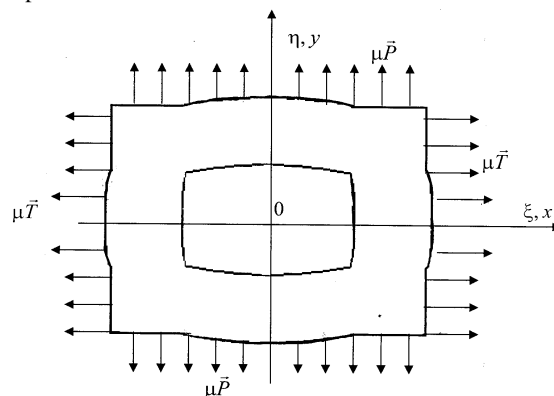


Figure 1. Deformed fabric with aperture.

In this study, a method is developed to investigate fabrics which have or haven't some inner cuts. Also, the conditions of the fabrics disruption at the cuts ends are studied. Further studies are essential to understand the local mechanical damages which produced from the manufacturing and the following processes, as these damages concentrate in areas of so small measure.

2. The Problem of Energy Functional Minimization

Let us consider the plane rectangular section of orthotropic shell including may be a rectangular aperture

* Corresponding author. m_nawafleh@hotmail.com.

[9, 10]. The deflected mode of this section is supposed (see Fig.1) to be axially symmetric with respect to Ox -axis and Oy -axis, tensile loads $\mu \bar{T}$ and $\mu \bar{P}$ applied to the section edges are respectively parallel to the axes mentioned above, where μ is a parameter, which is introduced in such way that all investigation may be easily and exactly fulfilled if $\mu = 0$.

For indication of plane location of any shell's particle two coordinate systems are used: Cartesian coordinate system Oxy and material (Lagrangian) system $O\xi\eta$ identifying shell's particles. We assume that material coordinates ξ, η of any shell's particle coincide with its Cartesian coordinates x, y when the shell is in non-deformed state.

In view of mentioned assumption it is possible to indicate the location of any shell's particle by equalities

$$x = \xi + u(\xi, \eta), \quad y = \eta + v(\xi, \eta), \quad (1)$$

where $u(\xi, \eta)$ and $v(\xi, \eta)$ are displacements of the shell's particle with Lagrangian coordinates ξ, η along Ox -axis and Oy -axis respectively.

Extensional strains of coordinate curves $\eta = const$ and $\xi = const$ are defined by expressions

$$\begin{aligned} \varepsilon_1 &= \sqrt{\left(1 + \frac{\partial u(\xi, \eta)}{\partial \xi}\right)^2 + \left(\frac{\partial v(\xi, \eta)}{\partial \xi}\right)^2} - 1, \\ \varepsilon_2 &= \sqrt{\left(\frac{\partial u(\xi, \eta)}{\partial \eta}\right)^2 + \left(1 + \frac{\partial v(\xi, \eta)}{\partial \eta}\right)^2} - 1. \end{aligned} \quad (2)$$

On the assumption of the absence of external forces distributed over the shell surface the following vector equilibrium equation takes place [1, 2]:

$$\frac{\partial}{\partial \xi} \left(\sigma_1(\xi, \eta) \left| \frac{\partial r(\xi, \eta)}{\partial \eta} \right| \right) + \frac{\partial}{\partial \eta} \left(\sigma_2(\xi, \eta) \left| \frac{\partial r(\xi, \eta)}{\partial \xi} \right| \right) = 0 \quad (3)$$

Here

$$\sigma_1(\xi, \eta) = e_1 \sigma_{11} + e_2 \sigma_{12}, \quad \sigma_2(\xi, \eta) = e_1 \sigma_{21} + e_2 \sigma_{22}, \quad (4)$$

Where

$$e_1 = \frac{\partial r(\xi, \eta)}{\partial \xi} \left/ \left| \frac{\partial r(\xi, \eta)}{\partial \xi} \right| \right., \quad e_2 = \frac{\partial r(\xi, \eta)}{\partial \eta} \left/ \left| \frac{\partial r(\xi, \eta)}{\partial \eta} \right| \right.,$$

$r(\xi, \eta) = x(\xi, \eta)\mathbf{i} + y(\xi, \eta)\mathbf{j}$ - is radius-vector (with respect to point O) of the shell's particle corresponding to Lagrangian coordinates ξ, η .

Let us consider the fabric section restricted by the lines $\xi = \bar{\tau}L$ and the lines $\eta = \bar{\tau}H$. Suppose that the rectangular aperture is enclosed between the lines $\xi = \bar{\tau}l$ and the lines $\eta = \bar{\tau}h$. It is quite reasonable to content ourselves with consideration of the quarter of the section located in the first quadrant of the plane Oxy and to set up the following zones. The first one is restricted by the lines $\xi = 0, \xi = l, \eta = h, \eta = H$; the second one - by the lines $\xi = l, \xi = L, \eta = h, \eta = H$; the third one - by the lines $\xi = l, \xi = L, \eta = 0, \eta = h$.

The analysis of the deflected mode of the soft shell is based on variational methods under the supposition of

elasticity of the shell material; therefore the equilibrium state of the shell reduces its energy functional to a minimum. This functional can be represented in the form (equation 5):

$$U = \iint_S F \left(\mu, \frac{\partial u}{\partial \xi}, \frac{\partial u}{\partial \eta}, \frac{\partial v}{\partial \xi}, \frac{\partial v}{\partial \eta} \right) d\xi d\eta - \mu T \int_0^H u(L, \eta) d\eta - \mu P \int_0^L v(\xi, H) d\xi$$

where the double integral is taken over the whole fabric, function F under the integral sign is the density of strain energy which is supposed to be known.

For greater definiteness of our considerations we shall assume, that the shell is linearly elastic network with rectangular cells. In this case it is possible to copy (5) in the form of (equation 6):

$$U = \iint_S (k_1 \varepsilon_1^2 + k_2 \varepsilon_2^2) d\xi d\eta - \mu T \int_0^H u(L, \eta) d\eta - \mu P \int_0^L v(\xi, H) d\xi,$$

where k_1 and k_2 are the coefficients describing elastic properties of the fabric.

3. Finite Elements Method

Definitional domain of functions $u(\xi, \eta)$ and $v(\xi, \eta)$ is subjected to triangulation according to the scheme shown in Fig. 2.

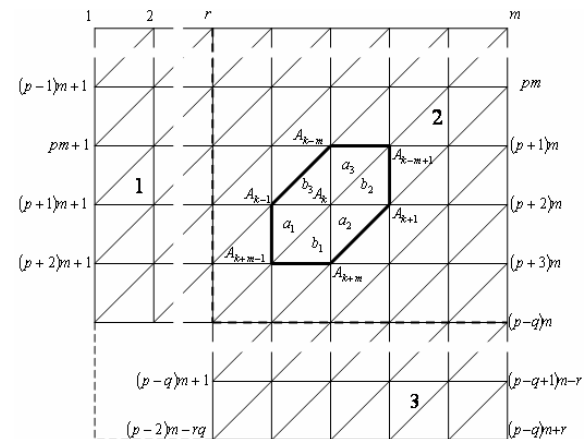


Figure 2. Triangulation of functions domain.

Without essential loss of generality one could suppose legs of all triangles to be equal, so that the following identities hold on [11, 12]:

$$s = \frac{L}{m} = \frac{l}{r} = \frac{H}{n} = \frac{h}{q} \quad (7)$$

These equalities in particular define the sense of integers m, r, q and n .

As it can be seen in Fig.3, we deal with two types of elements. Let us introduce functions (equation 8):

$$\begin{aligned} f_1(\xi, \eta; \xi_k, \eta_k) &= 1 + \frac{1}{s}(\xi_k - \eta_k - \xi + \eta), \\ f_2(\xi, \eta; \xi_k, \eta_k) &= \frac{1}{s}(\eta_k - \eta), \quad f_3(\xi, \eta; \xi_k, \eta_k) = \frac{1}{s}(\xi - \xi_k), \end{aligned}$$

which distinctive feature is that f_i equals 1 in apex i and equals zero in other apexes, corresponding to the elements of type 1; everywhere outside of the element these functions are zero.

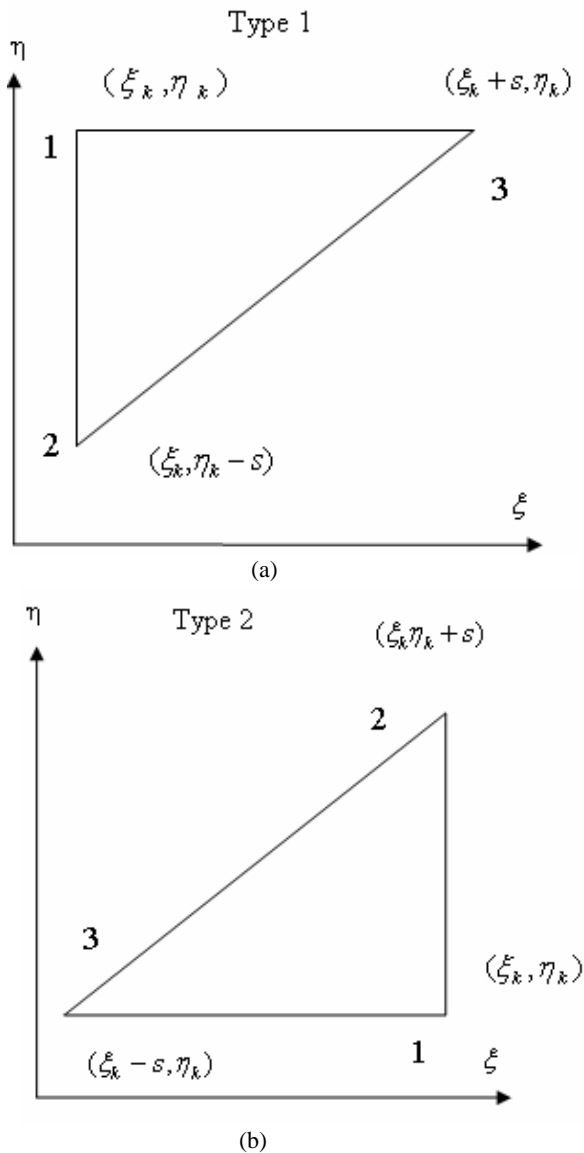


Figure 3. (a), (b). Two types of finite elements.

Similar functions correspond to the elements of type 2:

$$\begin{aligned}
 p_1(\xi, \eta, \xi_k, \eta_k) &= 1 + \frac{1}{s}(\xi - \xi_k - \eta + \eta_k), \\
 p_2(\xi, \eta, \xi_k, \eta_k) &= \frac{1}{s}(\eta - \eta_k), \quad p_3(\xi, \eta, \xi_k, \eta_k) = \frac{1}{s}(\xi_k - \xi).
 \end{aligned} \tag{9}$$

Now it is easy to obtain following approximation of displacements u and v :

$$u(\mu, \xi, \eta) = \sum_{k=1}^{MN-mn} u_k \tilde{U}_k(\xi, \eta), \quad v(\mu, \xi, \eta) = \sum_{k=1}^{MN-mn} v_k \tilde{V}_k(\xi, \eta), \tag{10}$$

where \tilde{U}_k and \tilde{V}_k are easily construed of functions given by (8) and (9).

Substitution of expressions (10) into energy functional (5) transmutes it into the function of required coefficients

$$u_k = u_k(\mu) = u(\mu, \xi_k, \eta_k)$$

$$\text{and } v_k = v_k(\mu) = v(\mu, \xi_k, \eta_k).$$

By dint of equating the partial derivatives of this function with respect to mentioned coefficients u_k and v_k with zero, a system of algebraic equations could be obtained as the solution of which the coefficients could be found.

This system can be written as follows (equation 11):

$$\begin{aligned}
 \frac{\partial U}{\partial u_k} &= 2 \iint_S \left[\frac{k_1 \varepsilon_1}{1 + \varepsilon_1} \left(1 + \frac{\partial u}{\partial \xi} \right) \frac{\partial \tilde{U}_k}{\partial \xi} + \frac{k_2 \varepsilon_2}{1 + \varepsilon_2} \frac{\partial u}{\partial \eta} \frac{\partial \tilde{U}_k}{\partial \eta} \right] d\xi d\eta - \mu \int_0^H \tilde{U}_k(L, \eta) d\eta = 0, \\
 \frac{\partial U}{\partial v_k} &= 2 \iint_S \left[\frac{k_1 \varepsilon_1}{1 + \varepsilon_1} \frac{\partial v}{\partial \xi} \frac{\partial \tilde{V}_k}{\partial \xi} + \frac{k_2 \varepsilon_2}{1 + \varepsilon_2} \left(1 + \frac{\partial v}{\partial \eta} \right) \frac{\partial \tilde{V}_k}{\partial \eta} \right] d\xi d\eta - \mu \int_0^H \tilde{V}_k(\xi, H) d\xi = 0.
 \end{aligned}$$

4. Zero-Approximation Solution

In order to analyze this nonlinear system let us differentiate all equations with respect to parameter μ . As the result a system of linear equations in regard to derivatives $du_k / d\mu$ and $dv_k / d\mu$ is obtained.

This system is following:

$$C(\mu, X(\mu)) \frac{dX}{d\mu} = B(\mu, X(\mu)), \tag{12}$$

where C is a matrix of a format $t \times t$, B is a vector of length t , X is a required vector of the same length $t = 2((n - q)(m - 1) + (m - r)(q - 2))$.

Here the next designations are used

$$u_k = X_{2k-2}, \quad v_k = X_{2k-1}, \tag{13}$$

while $k < 2(m - 1)(n - q)$. Otherwise

$$u_{m(n-q)+r} = X_{2[m(n-q)+r-1]}, \quad v_{m(n-q)+r} = X_{2[m(n-q)+r]-1}. \tag{14}$$

Thus, the system (13) represents system of the ordinary differential equations from which should be found $u_k(\mu)$ and $v_k(\mu)$.

Solution of this system leads to Cauchy problem if $u_k(0)$ and $v_k(0)$, or more definitely $X_k(0)$, are known values.

Having written down (13) in the form of

$$\frac{dX}{d\mu} = C^{-1}(\mu, X(\mu)) B(\mu, X(\mu)), \tag{15}$$

we can construct the decision under the recurrent formula (16):

$$X(\Delta\mu) = X(0) + \frac{dX}{d\mu} \Big|_{\mu=0} \Delta\mu = X(0) + C^{-1}(0, X(0)) B(0, X(0)) \Delta\mu,$$

$$X(\mu_k + \Delta\mu) = X(\mu_k) + \frac{dX}{d\mu} \Big|_{\mu=\mu_k} \Delta\mu = X(\mu_k) + C^{-1}(\mu_k, X(\mu_k)) B(\mu_k, X(\mu_k)) \Delta\mu.$$

Thus, calculation of the shell's deformation at any value μ can be carried out, if the decision of this problem is known at $\mu = 0$, or in other words, at the first approximation.

Zero-approximation $X(0)$ required to begin calculations by formulas (16) is construed under supposition that to $\mu = 0$ corresponds net-like fabric with

square meshes made of non-extensible threads [13, 14]. In this case it is readily seen that for the first of above mentioned zones the following equations are valid:

$$u(\xi, \eta) = U_1(\xi), \quad v(\xi, \eta) = V_1(\xi) \tag{17}$$

For the third zone the equations

$$u(\xi, \eta) = U_2(\eta), \quad v(\xi, \eta) = V_2(\eta) \tag{18}$$

are satisfied.

For the second zone we have

$$u(\xi, \eta) = C_1, \quad v(\xi, \eta) = C_2 \tag{19}$$

where C_1 and C_2 are arbitrary constants subjected to search.

Let us write out the equilibrium equations for indicated zones. For the first zone one obtains that

$$\frac{\partial}{\partial \xi} (\sigma_{11}^1(\xi, \eta) (1 + U_1'(\xi))) = 0 \tag{20}$$

$$\frac{\partial}{\partial \xi} (\sigma_{11}^1(\xi, \eta) V_1'(\xi)) + \frac{\partial}{\partial \eta} (\sigma_{22}^1(\xi, \eta)) = 0 \tag{21}$$

The equilibrium equations for the third zone are given by

$$\frac{\partial}{\partial \xi} (\sigma_{11}^3(\xi, \eta)) + \frac{\partial}{\partial \eta} (\sigma_{22}^3(\xi, \eta) U_2'(\eta)) = 0 \tag{22}$$

$$\frac{\partial}{\partial \eta} (\sigma_{22}^3(\xi, \eta) (1 + V_2'(\eta))) = 0 \tag{23}$$

For the second zone the following equations are carried out

$$\frac{\partial}{\partial \xi} (\sigma_{11}^2(\xi, \eta)) = 0, \quad \frac{\partial}{\partial \eta} (\sigma_{22}^2(\xi, \eta)) = 0 \tag{24}$$

In equations (20) – (24) the upper index $i, i = 1, 2, 3$, in designations σ_{11}^i and σ_{22}^i is used to identification of stresses in corresponding zone of the fabric section.

Equations (20)-(24) are easily integrated

$$\left. \begin{aligned} \sigma_{11}^1(\xi, \eta) &= \frac{s(\eta)}{1+U_1'(\xi)}, \sigma_{22}^1(\xi, \eta) = -s(\eta) \frac{\partial}{\partial \xi} \left(\frac{V_1'(\xi)}{1+U_1'(\xi)} \right) + f(\xi), \\ S'(\eta) &= s(\eta), \end{aligned} \right\} \tag{25}$$

$$\left. \begin{aligned} \sigma_{22}^3(\xi, \eta) &= \frac{q(\xi)}{1+V_2'(\eta)}, \sigma_{11}^3(\xi, \eta) = -Q(\xi) \frac{\partial}{\partial \eta} \left(\frac{U_2'(\eta)}{1+V_2'(\eta)} \right) + g(\eta), \\ Q'(\xi) &= q(\xi), \end{aligned} \right\} \tag{26}$$

$$\sigma_{11}^2(\xi, \eta) = G(\eta), \quad \sigma_{22}^2(\xi, \eta) = F(\xi) \tag{27}$$

where $f(\xi)$, $s(\eta)$, $q(\xi)$, $g(\eta)$, $F(\xi)$ and

$G(\eta)$ are the desired functions.

According to the problem statement the following boundary conditions should be satisfied:

$$\sigma_{22}^1(\xi, h) = -S(h) \frac{\partial}{\partial \xi} \left(\frac{V_1'(\xi)}{1+U_1'(\xi)} \right) + f(\xi) \equiv 0 \tag{28}$$

$$\sigma_{22}^1(\xi, H) = -S(H) \frac{\partial}{\partial \xi} \left(\frac{V_1'(\xi)}{1+U_1'(\xi)} \right) + f(\xi) \equiv P \tag{29}$$

$$\sigma_{11}^3(l, \eta) = -Q(l) \frac{\partial}{\partial \eta} \left(\frac{U_2'(\eta)}{1+V_2'(\eta)} \right) + g(\eta) \equiv 0 \tag{30}$$

$$\sigma_{11}^3(L, \eta) = -Q(L) \frac{\partial}{\partial \eta} \left(\frac{U_2'(\eta)}{1+V_2'(\eta)} \right) + g(\eta) \equiv T \tag{31}$$

$$\sigma_{11}^2(L, \eta) = G(\eta) \equiv T, \quad \sigma_{22}^2(\xi, H) = F(\xi) \equiv P \tag{32}$$

Furthermore, on the border of the first and the second zone as well as on the border of the second and the third zone the conditions of normal stresses conjunction should be satisfied. Satisfying these and also geometrical conditions of zones conjunction, as well as the symmetry conditions one can easily obtain that

$$\left. \begin{aligned} U_1(\xi) &= -\xi + \frac{T(H-h)}{P} \ln \left(\frac{P}{T(H-h)} \xi + \sqrt{1 + \left(\frac{P}{T(H-h)} \xi \right)^2} \right), \\ C_1 &= U_1(l) \end{aligned} \right\} \tag{33}$$

$$\left. \begin{aligned} V_2(\eta) &= -\eta + \frac{P(L-l)}{T} \ln \left(\frac{T}{P(L-l)} \eta + \sqrt{1 + \left(\frac{T}{P(L-l)} \eta \right)^2} \right), \\ C_2 &= V_2(h) \end{aligned} \right\} \tag{34}$$

$$\sigma_{11}^1(\xi, \eta) = T \sqrt{1 + \left(\frac{P}{T(H-h)} \xi \right)^2}, \tag{35}$$

$$\sigma_{22}^3(\xi, \eta) = P \sqrt{1 + \left(\frac{T}{P(L-l)} \eta \right)^2}$$

The displacements of the shell's particles $V_1(\xi)$, $U_2(\eta)$ should be obtained by dint of equations (25), (26) which accomplishes exact investigation of zero-approximation. This approximation is used as initial condition when the desired solution is numerically construed by continuation by parameter μ .

Obtained results allow us to calculate in zero-approximation coefficients $u_k(0)$ and $v_k(0)$.

For considered textile structure of fabric the stresses are defined by formulas:

$$\sigma_1 = e_1 \sigma_{11} = 2k_1 \varepsilon_1 e_1, \quad \sigma_2 = e_2 \sigma_{22} = 2k_2 \varepsilon_2 e_2, \quad \sigma_{12} = \sigma_{21} = 0 \tag{36}$$

The calculations performed in this paper have shown, that the internal boundary layers beginning at vertices of the aperture and dividing specified above zones arose.

Along these lines destruction of filaments forming the fabric leads to development of progressive cracks. In zero approximation exact estimations of the maximal values of stresses are received.

5. Conclusions

The strains of the fabric were calculated using finite element methods. In the calculations the elastic properties of the fabric are considered. The model developed takes into account the types of fabrics which possess some inner cuts also the model applies for fabrics haven't such inner cuts. Referring to the different boundary conditions, the fabric is divided into stress deformed states which are bi-axial or uni-axial. Lines of concentrations as well as lines of disruption are used to describe the boundaries of the stress deformed zones. The conditions expected from the calculations based on the zero ordered solution are found to be applicable in the vicinity of the lines of concentration and lines of disruption. The calculations showed also that the conditions of fabric disruption appear at the end of the cuts.

References

- [1] I.V. Dneprov, A.T. Ponomarev, A.V. Radchenko, "The stress-strain state of soft shells of arbitrary shape". *Journal of Mathematical Sciences*, Vol.72, No. 5, 1994, 3293-3298.
- [2] N. Pan, "Development of a constitutive theory for short-fiber yarns: The Mechanics of Blended Fibrous Structures". *J. Textile Inst.*, Vol. 87, No. 3, 1996, 467-483.
- [3] Zienkiewicz O. *Finite element method in engineering science*. New York: McGraw-Hill; 1971.
- [4] G.A. Carnaby, N. Pan, N, "Theory of the compression hysteresis of fibrous assemblies". *Textile Res. J.*, Vol. 59, No. 5, 1989, 275-284.
- [5] R.M.J. Sidhu, R.C. Averill, M. Riaz, F. Pourboghart, "Finite element analysis of textile composite preform stamping". *J. Compos. Struct.*, Vol. 52, 2001, 483- 497.
- [6] P.H. Dastoor, T.K. Ghosh, S.K. Batra, S.P. Hersh, "Computer-assisted structural design of industrial woven fabrics". Part III: modelling of fabric uniaxial/biaxial load-deformation, *J. Text. Inst.*, Vol. 85, 1994, 135-57.
- [7] N. Pan, G.A. Carnaby, "Theory of the shear deformation of fibrous assemblies". *Textile Res. J.*, Vol. 59, No. 5, 1989, 285-292.
- [8] H.M. Irvin, "Analytical solution for pretensioned cable nets". *Journal Eng. Mech. Div. ASCE*, Vol. 102, 1976, 43-57.
- [9] J.W.S. Hearle, W.J. Shanahan, "An energy method for calculations in fabric mechanics. Part I: principles of the method. Part II: examples of the application of the method to woven fabrics", *J. Text. Inst.*, Vol. 69, 1978, 81-100.
- [10] T.V. Sagar, P. Potluri, J.W.S. Hearle, "Meso-scale modeling of interlaced fibre assemblies using energy method". *Comput. Mater. Sci.* Vol. 28, 2003, 49-62.
- [11] M. King, S. Socrate, "A shell formulation to model the three-dimensional deformation response of woven fabrics". *ASME International Mechanical Engineering Congress and Exposition*, Anaheim, CA, USA, 2004
- [12] S. Kawabata, M. Niwa, H. Kawai, "The finite-deformation theory of plain-weave fabrics. Part II: the uniaxial-deformation theory". *J. Text. Inst.*, Vol. 64, 1973, 47-61.
- [13] U. Ramamurty, T. Seshacharyulu, "Effect of spatial inhomogeneity in fiber packing on the strength variability of almatrix composites". *Mater. Sci. Engng A – Struct. Mater. Properties Microstruct. Processing*, Vol. 268, NO. 1-2, 1999, 97-103.
- [14] Hearle J W S, Grosberg P, Backer S. *Structural mechanics of yarns and fabrics*. New York: Wiley-Interscience; 1969.

Modeling and Verification of Double Slope Single Basin Solar Still Using Laboratory and Actual Solar Conditions

K. Kalidasa Murugavel^a, Kn. K. S. K. Chockalingam^a, K. Srithar^{b,*}.

^aDepartment of Mechanical Engineering, National Engineering College, Tamil Nadu, India.

^bDepartment of Mechanical Engineering, Thiagarajar College of Engineering, Madurai, Tamil Nadu, India.

Abstract

A double slope single basin, passive type, still with basin area of 1.75 m² is fabricated and tested under laboratory conditions. The solar radiation heat is simulated by using 2 kW electrical resistance heater placed below the inner basin. The heat supply is varied using control circuit. The still is tested for varying input condition to simulate the actual solar radiation condition with different minimum depths of water in the basin ranging from 2 cm to 0.2 cm. The experiment is also carried out at different constant input conditions with a constant depth of water. The variation of different parameters with production rate has been studied. It is found that the production rate increases with the increases of water and glass temperature. But at higher operating temperature, the production rate increases with the decrease in temperature difference between water and glass. A new model is recommended for the still with shallow basin. The experiment is also conducted with the same still at actual sunshine conditions and compared with the model. The experimental values are in close agreement with model values.

© 2009 Jordan Journal of Mechanical and Industrial Engineering. All rights reserved

Keywords: Solar Still; Laboratory Simulation; Minimum Depth; Modeling; Productivity Enhancement.

Symbols

A	Area (m ²)
C	Specific heat (J/kg K)
Gr	Groshof number
h_c	Heat transfer coefficient (W/m ² K)
h_e	Evaporative heat transfer coefficient based on temperature difference (W/m ² K)
h_{ew}	Evaporative heat transfer coefficient based on pressure difference (W/m ² K)
h_{fg} (J/kg)	Latent heat of evaporation of the water
h_{ga}	Heat transfer coefficient of the glass upper surface to air (W/m ² K)
k	Thermal conductivity (W/m K)
L_c	Length (m)
M	Molecular weight
m	Mass production rate (gr/min or kg/m ² /h)
Nu_L	Nusselt number
P	Perimeter (m)
p	Pressure (N/m ²)
Pr	Prandtl number
Q	Heat transfer rate (W)
Q_c	Convection heat transfer rate from water surface to glass (W)
Q_e	Evaporation heat transfer rate from water surface to glass (W)
Ra_L	Rayleigh number
T	Temperature, °C

Greek symbols

ω	Specific humidity of air, kg of vapour/kg of dry air.
ϵ	Emissivity of the glass,

Subscripts

a	Atmosphere, air
b	Basin
g	Glass
g_a	Glass to atmosphere
s	Saturation condition
w	Water
ws	Water vapour at saturation condition

1. Introduction

A lot of works have been done on improving the effectiveness of the simple solar still, which converts the brackish water into fresh water, using solar energy. Recently, the authors reviewed the progress in improving the effectiveness of simple single basin solar still [1]. Studies show that basin water temperature is the significant parameter that affects the effectiveness of the still. The basin water temperature is at maximum when the heat capacity of the basin is less. The heat capacity of the basin depends on the depth of the water in the basin. For

* Corresponding author. ponsathya@hotmail.com

given solar intensity variation, the still production rate is higher, when depth is at minimum [2-6].

A Number of studies in the literature is available to examine heat transfer process of the still. The most widely acceptable study was made by Dunkle [7]. Since then, most of researchers used the proposed Dunkle's [7] model for their analysis. But, the above model is suitable for mean basin water temperature of 50°C. Clark [8] conducted steady state experiment on solar still; and examined the validity of the various correlations, proposed earlier for evaluating the heat transfer coefficients. Shawaqfeh and Farid [9] investigated heat and mass transfer processes and recommended new correlations for internal convective heat transfer coefficient. Kumar and Tiwari [10] recommended to test and model the fabricated still for various atmospheric conditions for predicting the performance at a particular place. An experimental still has been tested, and analysis have been made to study the water to cover heat transfers by Porta et al. [11] and a correlation to calculate the production rate of the still is also recommended [12]. Recently Tripathi and Tiwari [3, 13] studied the effect of basin water depth on the internal heat transfer coefficients.

The authors already conducted experiment with a laboratory solar still, for layer of water with different basin materials; and studied the performance and noted the peculiar behavior of the still at higher basin water and glass temperatures [14]. At lower depths, the basin water temperature is high, and the production rate of the still is not in proportion with basin water temperature and the difference between the basin and glass temperatures. The objective of this work is to conduct three experimental works to analyze the performance of the double slope single basin solar still. Two works are carried out in laboratory conditions; one with varying heat input condition. Here, the experiments are carried out with varying depths ranging from 2 cm to 0.2 cm. This will help in studying the effect of solar insulation on productivity. The second experiment is conducted with constant heat input condition to study the variation of production rate with various temperatures. Hence, constant depth of 1 cm is also maintained. A new model for the still is proposed from the above analysis. The model is verified by testing the still at actual solar radiation condition for minimum depths of water in the basin. For the still at actual sunshine condition, the heater is taken out, and the bottom is leveled with cement concrete. This concrete layer stores excess heat during noon and releases heat during evening and night. This increases the nocturnal production.

2. Internal and External Heat Transfer Processes

The modes of heat transfer inside the still between the water surface and the glass cover are convection accompanied with evaporative mass transfer in the form of water vapour and radiation. The radiation heat transfer is very small if compared with other two heat transfers, and the production of the still is not affected significantly by this heat transfer. The evaporative heat transfer is responsible for the transportation of water mass from water

surface to cover. This evaporative heat transfer increases with the vapour pressure difference between the water and glass; and is responsible for bulk motion of air inside the still. This bulk motion increases the convection heat transfer. Hence the convection and evaporation heat transfer inside the still are interrelated.

Dunkle [6] used the following correlation developed by Jakob [15] to estimate the convection heat transfer coefficient inside the still, (Relation.1)

$$h_c = 0.884 \left[(T_w - T_g) + \frac{(p_w - p_g)(T_w + 273.15)}{268900 - p_w} \right]^{2/3}$$

The convective heat transfer is given by [7],

$$Q_c = A_b h_c (T_w - T_g) \quad (2)$$

The evaporative heat transfer coefficient as per the detailed derivation given by Malik et al. [16] is given by,

$$h_{ew} = \frac{M_w h_{fg} p}{M_a C_p (p - p_w)(p - p_g)} h_c \quad (3)$$

Dunkle [6] assumed that the p_w and p_g are considerably smaller than the total pressure p , and the mean operating temperature is 50°C and estimated the value of h_c as,

$$h_{ew} / h_c = 0.016273 \quad (4)$$

In equation (3), the values p_w and p_g are considerably smaller than p for lower range of basin water and glass temperatures. When the still is with shallow basin, the mean water and glass temperatures are higher than 50°C; and the equation (4) can not be used. At higher temperatures, the partial pressure values are considerably higher, and the equation (4) will not yield a constant value. The evaporative heat transfer is given by [16],

$$Q_e = A_b h_{ew} (p_w - p_g) \quad (5)$$

The mass transfer rate of water vapour is given by [16],

$$m_w = \frac{Q_e}{h_{fg}} \quad (6)$$

At higher basin water temperature, the water is more susceptible to evaporation and the water mass proportion in the still air is high. The percentage of mass of water vapour present in the air inside the still is given as by assuming the air as saturated,

$$\text{percentage of vapour} = \frac{\omega_s}{1 + \omega_s} \times 100 \quad (7)$$

where ω_s is the kg of vapor present in the one kg of dry air at saturated condition and it is given as [17],

$$\omega_s = 0.662 \frac{p_{ws}}{p - p_{ws}} \quad (8)$$

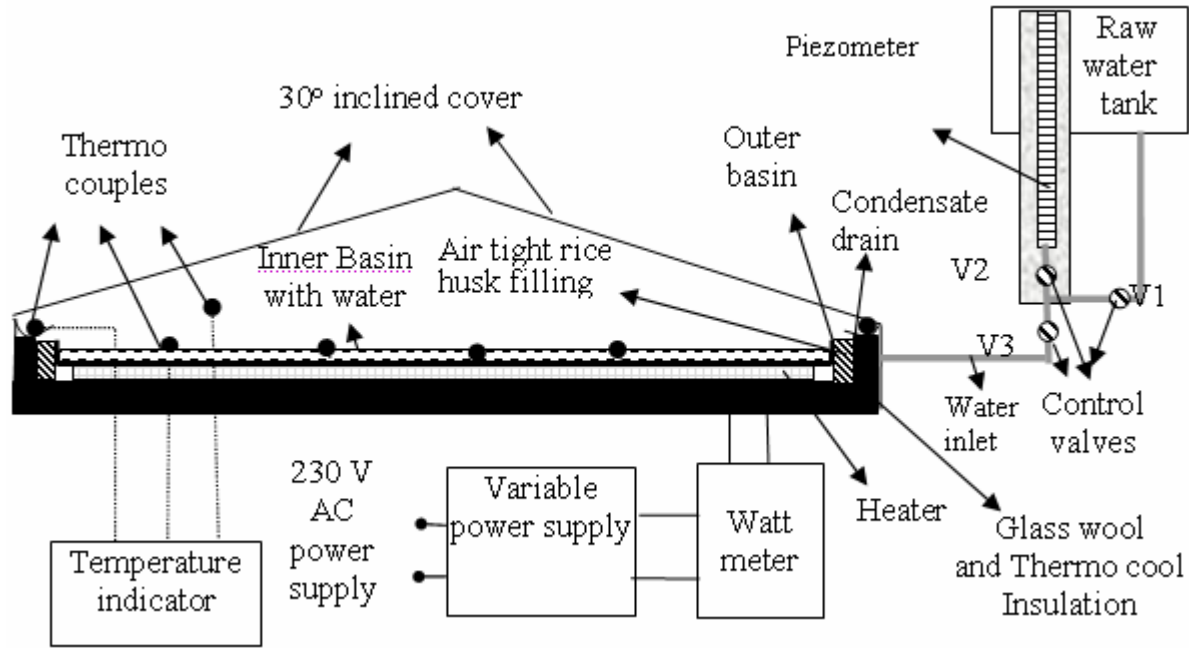


Figure 1. Single basin double slope laboratory still.

The increase in p_{ws} with temperature is exponential. Hence, at higher basin and water temperature, the productivity depends on rate of heat transfer from the glass cover to the atmosphere. The effect of the temperature difference between the water and glass, which is the driving force for the bulk motion of air inside the still on condensation and transportation of water mass from basin to glass, is less significant.

The evaporative heat transfer coefficient, h_e based on the temperature difference between the water and glass can be calculated using following relation,

$$Q_e = m_w h_{fg} = A_b h_e (T_w - T_g) \tag{9}$$

The amount of heat transfer from the glass upper surface to the atmosphere is given by:

$$Q_{ga} = A_g \{ h_{ga} (T_g - T_a) + \epsilon_g [(T_g + 273)^4 - (T_a + 273)^4] \} \tag{10}$$

In most of the studies this values is taken as constant of $4.5 \text{ W/m}^2 \text{ K}$ as recommended by Duffie [18] including the radiation effect for no freeze condition. In this work, the actual convection heat transfer coefficient of the inclined surface was calculated using the procedure given by Incropera and Dewitt. [19].

The relation for average Nusselt number for the glass cover for entire range of Rayleigh number has been recommended by Churchill and Chu [20] and is of the form: (Relation.11)

$$Nu_L = \left\{ 0.825 + \frac{0.387 Ra_L^{1/4}}{\left[1 + (0.492/Pr)^{1/4} \right]^{1/4}} \right\} \frac{h_g L_c}{k} \tag{11}$$

$$\text{where } L_c = \frac{A_g}{P} = 1.18 \text{ m.}$$

The overall heat transfer coefficient of the glass surface, including the radiation heat transfer to atmosphere and without considering sky radiation, can be calculated as:

$$Q_{ga} = A_g h_{ga} (T_g - T_a) \tag{12}$$

3. Laboratory and Solar Still

A single basin double slope solar still has been fabricated with mild steel plate, as shown in Figure 1. The overall size of the inner basin is $2.08 \text{ m} \times 0.84 \text{ m} \times 0.075 \text{ m}$, and that of the outer basin is $2.3 \text{ m} \times 1 \text{ m} \times 0.25 \text{ m}$. The gap between the inner and outer basin is packed with rice husk as insulation material. The top is covered with two glasses of thickness 4mm, inclined at 30° on both sides, using wooden frame. The outer surfaces of the still are covered with glass wool and thermo cool insulation. The condensed water is collected in the V-shaped drainage provided below the glass lower edge of the still. The condensate collected is continuously drained through flexible hose and stored in a jar placed on the electronic weighing machine on both side of the still. A hole in the basin side wall allows inserting the thermocouples for the measurement of the basin water, still, and condensate temperature. To measure the basin temperature, four thermocouples were placed at the basin at different locations. Two thermocouples were dipped into the water in the collecting drainage on either side. The hole is closed with insulating material to avoid the heat and vapour loss. One thermocouple is exposed to atmosphere to measure the atmospheric temperature. This thermocouple is placed in a shadow area to prevent the variation in temperature due to incidence of sun radiation on the thermocouple.

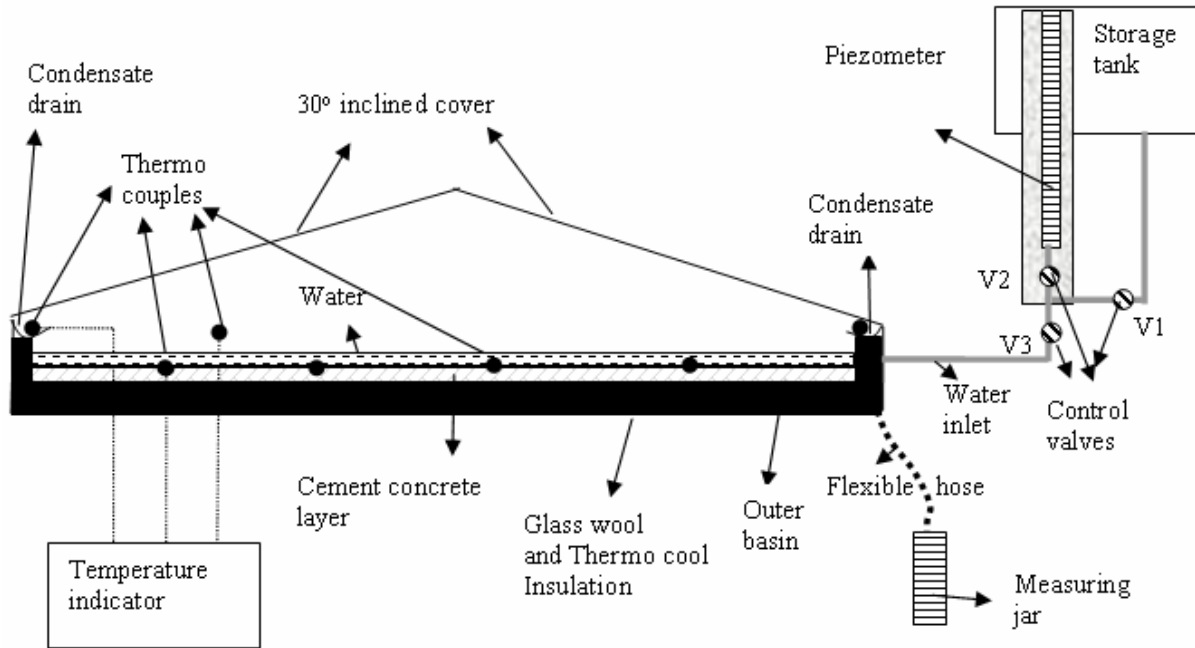


Figure 2. Single basin double slope solar still.

Another hole is provided for water inlet. Through this hole, a small tube is inserted to supply raw water continuously to the basin from storage tank through a flow regulator to keep the mass of water in the basin always constant. The heating coil of 2000 W is placed below the inner basin to supply necessary heat energy to the basin. The input to the heater is given through a control circuit, which controls the input electrical energy. An energy meter is fitted with the circuit to measure the input energy.

To convert the laboratory still into an actual solar still, the heater and power supply and measurement systems were removed. The inner basin is also removed. The bottom of the still is leveled with 5 cm thick cement concrete to minimize heat loss through the basin and to spread the minimum depth of water uniformly, shown in Figure 2. The concrete surface is black painted to improve the radiation absorption capacity. The distillate output was recorded with the help of a measuring jar. The solar intensity was measured with the calibrated PV type sun meter.

4. Experimental Procedure

The experiment was carried out in the fabricated laboratory still at Steam Laboratory, National Engineering College, Kovilpatti (9°11'N, 77°52'E), a city in southern India during December 2005 to February 2006. In the laboratory still, the heat input is given to the solar still using heating coil through control circuit. For a given constant depth of basin water condition, the input to the heater is varied for every 15 minutes from 0 - 775 W/m² between 6 AM and 12 noon and from 775 - 0 W/m² between 12 noon and 6 PM to match with the local average solar radiation condition [8]. During night, the heater supplies no heat. For given depth, all the observations are taken for 24 hours duration, starting from 6 AM. The temperature of the atmosphere, basin water, and the condensate are noted for every 15 minutes. The

energy meter readings and condensate collected on both side of the still are also noted. The experiments were conducted for 2 cm, 1.5 cm, 1 cm, 0.5 cm and 0.2 cm depth of water in the still basin for same solar condition without freeze. For experimentation with depth of water 0.5 cm and 0.2 cm, a light black cotton cloth is used to spread the water through the entire area of the basin. The condensate temperature is taken as the temperature of the glass cover. Figure 3 shows energy input given to the laboratory still at various times and corresponding variation in atmospheric temperature.

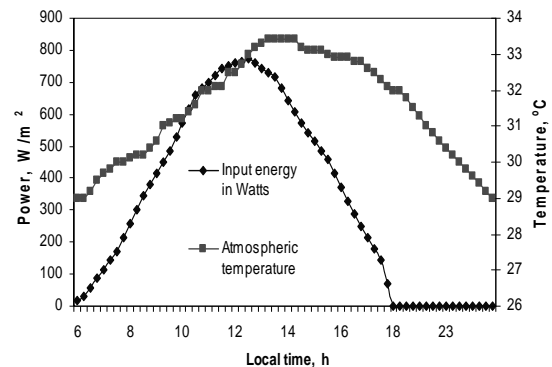


Figure 3. Input energy and atmosphere temperature variation in the simulated solar still.

The still is also tested under various constant input conditions with different depths of water in the basin. Heat is supplied by the heater until the still reaches steady state condition. Then power is cut off and the still is allowed to cool down naturally to reach equilibrium state with atmosphere. The readings are taken for every 15 minutes from the time the still starts to deliver water production until it delivers significant amount of output. The experiments are carried out for the constant input powers from 300 W to 1500 W.

The experiments with solar still at actual sunshine conditions were conducted during February to April 2007

for various depths ranging from 10 cm to 0.5 cm. The observations are taken for 24 hours duration, starting from 6 AM. The total radiation on horizontal plane, the temperatures of the atmosphere, basin water and condensate and the mass of condensate collected are noted for every 30 minutes.

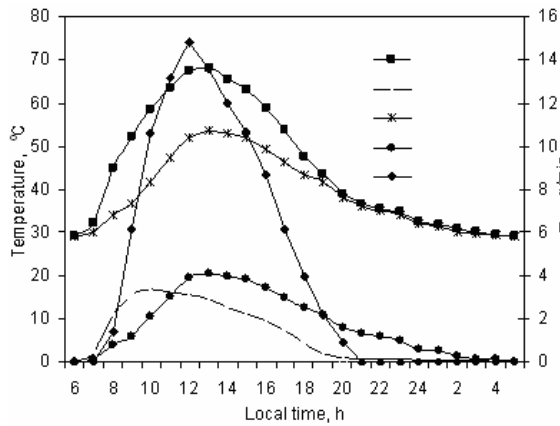


Figure 4. Variation in temperatures and production rate for laboratory still with varying input – set I.

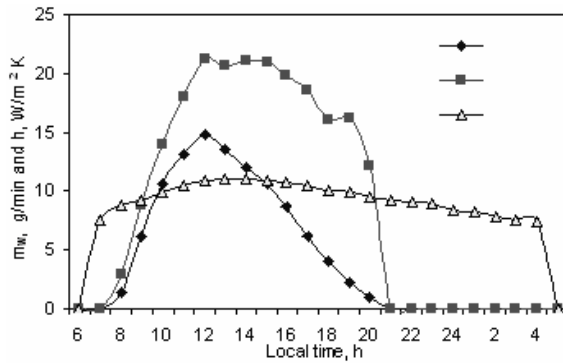


Figure 5. Variation in heat transfer coefficients and production rate for laboratory still with varying input

5. Results and Discussion

5.1. Analysis of Laboratory Still at Variable Input Condition

The evaporative heat transfer coefficients are calculated using equation (9), and the overall heat transfer coefficient of the glass surface to the atmosphere is calculated using equations (10) to (14). Figure 4 shows the variation of water and basin temperatures, water-glass temperatures difference, and glass-atmospheric temperatures difference, and water production rate with time for laboratory still with a depth of 0.5 cm and under varying input condition. The variation of all parameters with production rate is normal and as expected. The variation of difference in temperature between water and glass is also different here. Initially, during morning hours when the input power is less, the production rate increases with this temperature difference.

When water temperature exceeds 50°C, this temperature difference reaches a maximum value and starts to decrease there after. The still production rate continues to increase until the difference in temperature between glass and atmosphere increases. The difference

between the glass and atmospheric temperatures is at maximum when the production rate is at maximum. Then all water and glass temperatures and difference in temperatures start to decrease with production rate.

The variation of the internal evaporative heat transfer coefficient and overall heat transfer coefficient for glass with local hours are in relation with production rate, shown in Figure 5. This variation is similar for different depths of water in the basin.

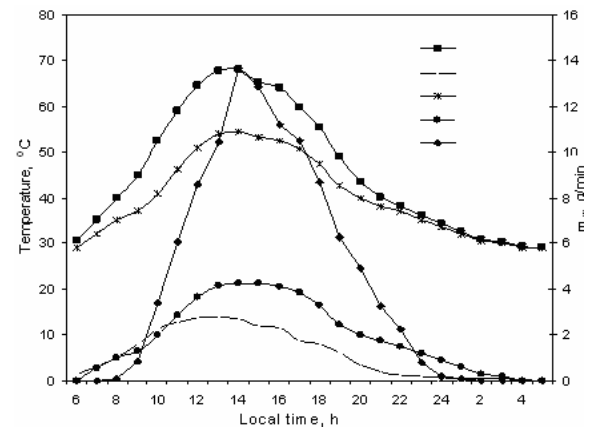


Figure 6. Variation in temperatures and production rate for laboratory still with varying input – set II.

The variation of the water and glass temperature and difference in water-glass and glass-atmospheric temperatures, are similar for the still with different lower depths ranging from 2 cm to 0.2 cm. The starting time and the duration in which the production rate increase with the decrease of the temperature difference between water-glass. Figure 6 shows the variation of these parameters for a still with 1 cm depth. For this still the peculiar behavior starts around 12 Noon and lasts up to around 2 PM. For the still with 0.5 cm depth, the peculiar behavior occurs during 10 PM and 1 PM [Figure 4].

For a given solar intensity variation in lower depth still, this peculiar behavior starts early and lasts longer duration and for higher depth, and starts early and lasts for shorter duration. For deep basin still, during lower solar intensity variations in a day, the still may not experience this peculiar operation. If a still experience this peculiar behavior for longer duration, the production per day will be high.

5.2. Analysis of Laboratory Still at Constant Input Condition

The variation of the different parameters of the laboratory still at constant input of 1500 W is shown in the Figure 7. The production rate of the still increases with the increase of water and glass temperatures during heat supply period. Also the production rate increases with the increase in water-glass temperature difference during this period. The production rate decreases with these parameters during cooling. This is the normal operation of the still.

During heating period, the production rate increases with the decrease in water-glass temperatures difference. It is the peculiar behavior of the still. During heating, the rate of decrease of water-glass temperature difference is minimal, and the corresponding rate of increase in production rate is higher. This peculiar behavior is

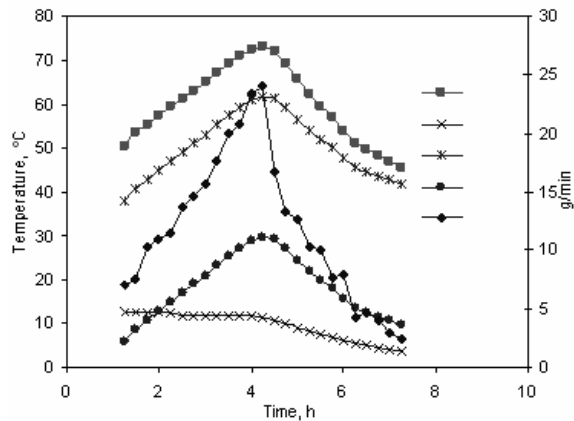


Figure 7. Variation in temperatures and production rate for laboratory still with 1500 W constant input.

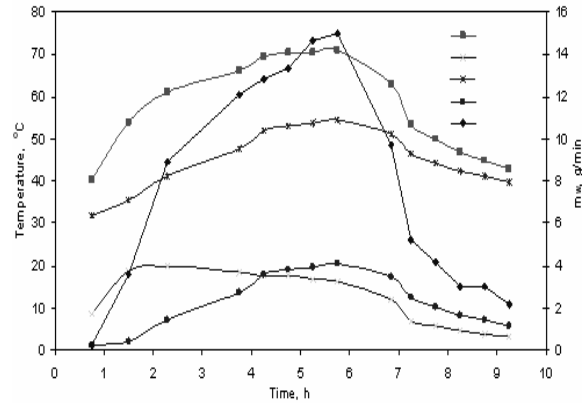


Figure 9. Variation in temperatures and production rate for laboratory still with 1200 W constant input.

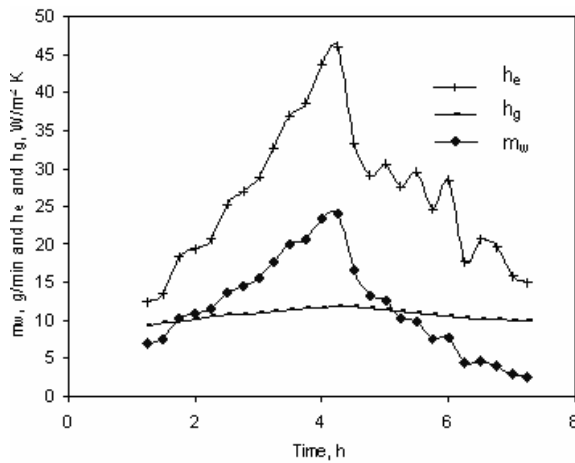


Figure 8. The variation in heat transfer coefficient and production rate for laboratory still with 1500 W constant input.

observed only during heating. During cooling, normal behavior is observed.

Figure 8 shows the variation production rate, internal evaporative heat transfer, and the external overall heat transfer coefficient of the glass cover with for the still. The variations of these parameters are in relation with the variation of production rate.

For the laboratory still with constant input, the variations of different parameters are similar for different constant input powers. For higher input power, rate of temperature rise for water and basin is higher, and production starts early. The water-glass temperatures initially increase with production rate for lower water and glass temperatures as shown in Figure 7. When the water temperature is around 55°C, this difference temperature attains a maximum value then starts to decrease. Similar variations are observed for the still with 1200 W input also as shown in Figure 9.

5.3. Modeling of Still

To study the production rate variation with water and glass temperatures, water-glass and glass-atmosphere temperature differences, a correlation plot is drawn by using the observations of the still under varying operating conditions as shown in the Figure 10. Both water and glass temperatures and difference between glass and atmospheric temperature are increasing with production rate. The overall variation of the difference between water

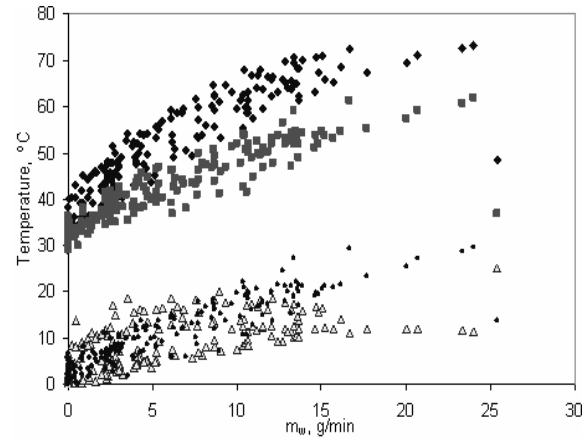


Figure 10. Variation of production rate with different temperatures for laboratory still.

glass temperatures is different. Initially this value increases with production rate, attains a maximum value and starts to decrease. The maximum value of this different corresponds to a water temperature around 55°C. The production rate is 5 g/min when the temperature difference between water and glass is in the range 5°C to 20°C. Similarly other parameters also have a range of values for a particular production rate.

At lower temperatures of water and glass, the water vapour present in the air inside still is in minimum proportion. The water mass proportion increases exponentially with the still air temperature, (equations (7) and (8)). Hence, production rate of the still depends on basin water and glass temperatures. At higher water temperature, water is more susceptible for evaporation, and the water vapour proportion in the still air is high. When the glass temperature is high, both heat transfer from glass to atmosphere and the production rate are also high. When the water and glass temperatures are higher, their difference is less, and the production rate is high. This is the reason for the peculiar operation of the still.

The amount of condensation at the glass lower surface mainly depends on the mass of air circulated, and in contact with the glass lower surface. This circulation depends on the temperature difference between water and glass. If the glass temperature is higher or water temperature is lower, this difference will be low and the production rate is also low. Hence the production rate is a complex function of water and glass temperatures and the

$$\begin{aligned}
 m_w = & -1.48 \times 10^{-3} T_w (T_g - T_a) - 3.901 \times 10^{-3} T_g (T_g - T_a) + 1.124 \times 10^{-3} (T_g - T_a) (T_w - T_g)^{(11)} \\
 & + 4.809 \times 10^{-3} (T_g - T_a)^2 + 0.146 \times (T_g - T_a) + 7.185 \times 10^{-4} T_w (T_w - T_g) - 1.196 \times 10^{-3} (T_w - T_g) \\
 & - 1.732 \times 10^{-3} (T_w - T_g)^2 + 0.039 \times (T_w - T_g) + 9.918 \times 10^{-5} T_w T_g + 7.349 \times 10^{-5} T_g^2 + 0.035 T_g \\
 & + 0.42 - 0.08 T_w + 8.932 \times 10^{-4} T_w^2
 \end{aligned}
 \tag{15}$$

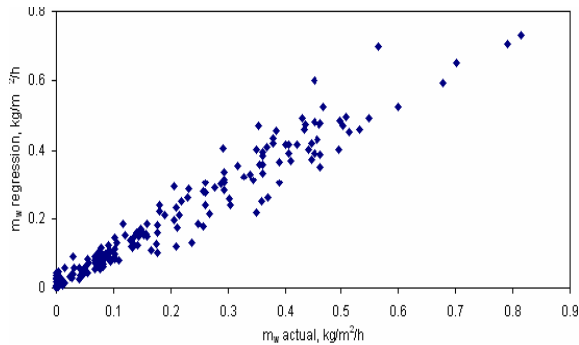


Figure 11. Comparison between actual and calculated values of production rate for laboratory still

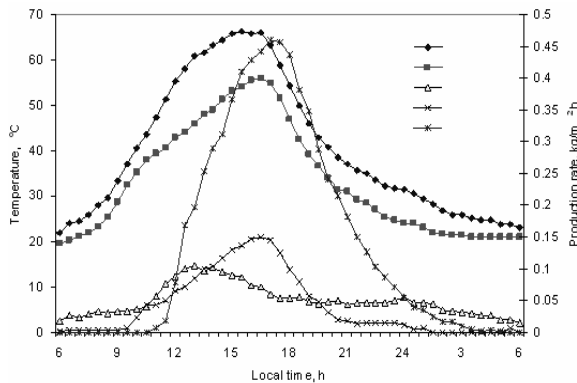


Figure 12. Performance of the solar still with medium depth

difference between the water-glass and glass-atmospheric temperatures.

The observation from laboratory still experiments at constant depth with varying constant input and with varying depth with constant varying input are used to establish a regression equation using Mathcad-12 software. Two-degree fitting function is used. The following equation is obtained for the production rate of the still in kg/m²/h.

The above equation (equation 15) is taken as a new model. Using this model, the production rate is calculated using the observations of laboratory still experiments, and the calculated values are compared with actual values. The Figure 11 shows the comparison between the actual and calculated production rate values by using the model. It is found that most calculated values are closer to actual values with a correlation coefficient of 0.974.

5.4. Analysis of the Still Under Solar Radiation Condition

The same laboratory still is tested under actual solar radiation condition for different depths of water in the basin. Both Figures No. 12 and and No. 13 show the performance of the stills when the depths of water are 3 cm and 1cm. The production rate of the still varies proportionally with different water, glass temperatures,

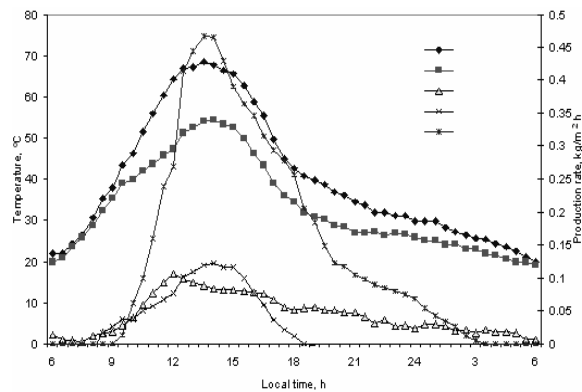


Figure 13. Performance of the solar still with lower depth .

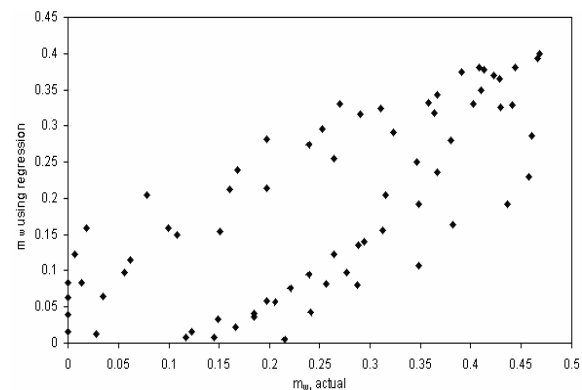


Figure 14. Comparison between actual and calculated values of production rate for actual solar still

and difference between glass and atmospheric temperatures. Similar with laboratory still, for actual still also, the production rate increases initially with the increase of the temperature difference between water and glass, but at higher temperature when the basin water reaches around 55°C, this difference is at maximum. But the production rate increases until the difference between the glass and atmospheric temperatures starts to decrease.

Hence the still, and under actual sunshine conditions, behaves similarly to laboratory still with varying input. Using the observed values of different temperatures, the new model is used to calculate the production rate for the actual solar still with different depths of 4 cm, 3 cm and 1 cm. The actual values and calculated values are compared by using the new model. The Figure 14 shows the comparison between the actual and values calculated, using the new model. The most of the calculated values are close to actual values with a correlation coefficient of 0.8646. The deviation in values due to sky radiation effect and wind velocity effect even though, during experiment time, no appreciable wind is observed.

6. Conclusion

A double slope single basin, passive type, still with basin fabricated; and tested under laboratory conditions. The heat is supplied to the basin using electrical resistance heater placed below the inner basin. The heat supply is varied using control circuit. The still is tested for varying input condition to simulate the actual solar radiation condition with different minimum depths of water in the basin ranging from 2 cm to 0.2 cm. The experiment is also carried out at different constant input conditions with a constant depth of 1 cm water. The variation of different parameters with production rate variation has been studied.

It is found that the production rate increases with the increases of water and glass temperature. At lower water and glass temperatures, the production rate is proportional with the temperature difference with water and glass. At higher operating temperatures, the production rate increases with the decrease in temperature difference between water and glass until the difference between the glass and atmospheric temperature increases. This is the peculiar behavior of the still. The reason for this behavior is the higher proportion of water vapour at higher still temperature. The still overall production rate per day will be high when the still operation in this peculiar behavior for longer duration.

A new model is proposed for the still with shallow basin. The experiment is also conducted with the same still at actual sunshine conditions. The still under solar radiation condition with lower depth behaves similarly to laboratory still. The experimental production rate values are in close agreement with model values. The proposed model can be used to predict the production rate of the still with minimum depth of water in basin in the range of 2 cm to 2 mm and for the basin water temperature up to 80°C.

References

- [1] K.K. Murugavel, S.K. Chockalingam, K. Srithar, "Progresses in improving the effectiveness of the single basin passive solar still". *Desalination*, Vol. 220, No. 1-2, 2008, 677-686.
- [2] P.I. Cooper, "Digital simulation of transient solar still processes". *Solar Energy*, Vol. 12, No. 3, 1969, 313-331.
- [3] R. Tripathi, G.N. Tiwari, "Thermal modeling of passive and active solar stills for different depths of water by using the concept of solar fraction". *Solar Energy*, Vol. 80, No. 8, 2006, 956-967.
- [4] R. Tripathi, G.N. Tiwari, "Effect of water depth on internal heat and mass transfer for active solar distillation". *Desalination*, Vol 173, No. 2, 2005, 187-200.
- [5] S. Aboul-Encin, A.A. El-Sebaei, El-Bialy, "Investigation of a single-basin solar still with deep basins". *Renewable Energy*, Vol. 14, No. 1-4, 1998, 299-305.
- [6] N. Hussain, A. Rahim, "Utilisation of new technique to improve the efficiency of horizontal solar desalination still". *Desalination*, Vol. 138, No. 1-3, 2001, 121-128.
- [7] R.V. Dunkle, "Solar water distillation; the roof type still and a multiple effect diffusion still". *International Developments in Heat Transfer, ASME, Proceedings of International Heat Transfer Part V, University of Colorado, 1961*.
- [8] J. A. Clark, "The steady state performance of a solar still". *Solar Energy*, Vol. 44, No. 1, 1990, 43-49.
- [9] A.T. Shawaqfeh, M.M. Farid, "New development in the theory of heat and mass transfer in solar stills". *Solar energy*, Vol. 55 No. 6, 1995, 527-535.
- [10] S. Kumar, G.N. Tiwari, "Estimation of convective mass transfer in solar distillation systems". *Solar energy*, Vol. 57, No. 6, 1996, 459-464.
- [11] M.A. Porta, E. Rubio, J.L. Fernandez, "Experimental measurement of the water-to-cover heat transfer coefficient inside shallow solar still". *Applied Thermal Engineering*, Vol. 18, No. 1-2, 1998, 69-72
- [12] E. Rubio, M.A. Porta, J.L. Fernade, "Cavity geometry influence on mass flow rate for single and double slope solar stills". *Applied Thermal Engineering*, Vol. 20, No. 12, 2000, 1105-1111.
- [13] R. Tripathi, G.N. Tiwari, "Effect of water depth on internal heat and mass transfer for active solar distillation". *Desalination*, Vol. 173, No. 2, 2005, 187-200.
- [14] K.K. Murugavel, K.K. Chockalingam, K. Srithar, "An experimental study on single basin double slope simulation solar still with thin layer of water in the basin". *Desalination*, Vol. 220, No. 1-3, 2008, 687-693.
- [15] Jacob M. *Heat Transfer*. New York: Wiley; 1957.
- [16] Malik M, Tiwar GN, Kumar A, Sodha MS. *Solar Distillation*. 1st ed., Oxford: Pergamon press; 1982.
- [17] Cengel Y. *Thermodynamics – An Engineering Approach*. 3rd edition. India: Tata Mc Graw Hill; 2003.
- [18] Duffie JA., Beckman WA. *Solar Energy Thermal Processes*. John Wiley and sons; 1974
- [19] Frank P. Incropera D, Dewitt P. *Heat and Mass Transfer*. Singapore: John Wiley & Sons (Asia) Pte. Ltd.; 2006.
- [20] S.W. Churchill, H.S. Humbert, "Correlating equations for laminar and turbulent free convection from a vertical plate". *International Journal of Heat and Mass Transfer*. Vol. 18, No. 11, 1975, 1323-1329.



الجامعة الهاشمية



المملكة الأردنية الهاشمية

المجلة الأردنية
للمهندسة الميكانيكية والصناعية

JJMIE

مجلة علمية عالمية محكمة

<http://jjmie.hu.edu.jo/>

ISSN 1995-6665

المجلة الأردنية للهندسة الميكانيكية والصناعية

مجلة علمية عالمية محكمة

المجلة الأردنية للهندسة الميكانيكية والصناعية: مجلة علمية عالمية محكمة أسستها اللجنة العليا للبحث العلمي في وزارة التعليم العالي والبحث العلمي، الأردن، وتصدر عن عمادة البحث العلمي والدراسات العليا، الجامعة الهاشمية، الزرقاء، الأردن .
هيئة التحرير

رئيس التحرير:

الأستاذ الدكتور موسى محسن
قسم الهندسة الميكانيكية، الجامعة الهاشمية، الزرقاء، الأردن .

الأعضاء:

الأستاذ الدكتور عدنان الكيلاني الجامعة الأردنية	الأستاذ الدكتور بلال العكش الجامعة الهاشمية
الأستاذ الدكتور أيمن المعاينة جامعة مؤتة	الأستاذ الدكتور علي بدران الجامعة الأردنية
الأستاذ الدكتور محمد النمر جامعة العلوم والتكنولوجيا الأردنية	الأستاذ الدكتور نسيم سواقد جامعة مؤتة

مساعد رئيس هيئة التحرير:

الدكتور أحمد الغندور
الجامعة الهاشمية

فريق الدعم:

تنفيذ وإخراج
م. أسامة الشريط

المحرر اللغوي
الدكتور وائل زريق

ترسل البحوث إلى العنوان التالي :

رئيس تحرير المجلة الأردنية للهندسة الميكانيكية والصناعية
عمادة البحث العلمي والدراسات العليا
الجامعة الهاشمية
الزرقاء - الأردن

هاتف : 3903333 00962 5 فرعي 4147

Email: jjmie@hu.edu.jo

Website: www.jjmie.hu.edu.jo